# Abstract

HAIJIANG PENG. Classical E&M Model for Nonlinear Optics — Applications to the Generation of Harmonic and Terahertz Radiation (Under the direction of Professor David E Aspnes).

Nonlinear optical techniques have become very useful diagnostic methods for surface and interface properties of materials and for developing new materials. However, it is still very difficulty to interpret nonlinear optical data. Here, I continued to develop the simplified bond hyperpolarizability model (SBHM). I extended the theory to describe the bulk-forbidden second harmonic generation (SHG), bulk third harmonic generation (THG), and fourth harmonic generation (FHG). I clarified the relative importance of bulk-forbidden contribution and surface dipole contribution to SHG. I showed the transverse-bond-direction motion was necessary to correctly describe THG data. And I presented a way to evaluate the surface roughness effects on FHG.

In addition, from the principle of SBHM, I developed a simple model to interpret the origin of terahertz radiation from semiconductor surfaces trigged by ultrashort laser pulse. I unified the mechanisms of terahertz generation — difference frequency mixing and current surge mechanism at the field level.

Finally, I showed spectroscopic SHG could give us more information than single frequency azimuthal dependent data.

# Classical E&M Model for Nonlinear Optics — Applications to the Generation of Harmonic and Terahertz Radiation

By

**Haijiang Peng**

A dissertation submitted to the Graduate Faculty of
North Carolina State University
in partial fulfillment of the requirements for
the Degree of Doctor of Philosophy

**PHYSICS**

Raleigh

2005

**APPROVED BY:**

| | |
|---|---|
| Dr. Christopher Roland | Dr. Hans Hallen |
| Dr. Robert M. Kolbas | Dr. David E. Aspnes<br>Chair of Advisory Committee |

# Dedication

To my grandmother Juyun Liu, grandfather Dongsheng Peng, my parents Funan Peng and Meixiu Chen, my stepmother Shengchun Liu, and my girl friend Shuwei Wu for their love.

# Biography

Haijiang Peng was born in a small village in XiangTan County, XiangTan, Hunan, P. R. China to Funan Peng and Meixiu Chen. His mother, Meixiu Chen, died a few hours after his birth. He grew up with his grandparents until he was 10 years old. He then stayed with his father and stepmother, continuing in elementary school in Changsha. After completing the $9^{th}$ grade, he passed the entrance examination for a special class, in which the students are trained specifically for attending the competition of Olympic-Physics competition for middle-school students. Unfortunately, his first try in physics was unsuccessful. He did not do as well as expected in the contest. However, he did not lose confidence. He continued his goal of physics in the Department of Physics, Jilin University, after his graduation from high school. In Jilin Unversity he was really attracted by the world of physics and felt the power of physics. He started his research under Prof. Chengxiang Zhang in solid state physics. After he obtained his bachelor degree, he went to the Department of Physics, National University of Singapore. There he worked on the growth of cobalt silicide for 0.18μm CMOS technology, which is supported by the largest chip manufacturing company, Chartered Semiconductor Manufacture Ltd. In this project, he published his first scientific referred-journal paper on solid-state electronics, "Effects of First Rapid Thermal Annealing Temperature on Co Silicide Formation". Two years later, he went to Department of Physics, North Carolina State University, to pursue his PhD degree under the direction of Prof. David E. Aspnes. He and Dr. Aspnes worked together very well, publishing 5 referred journal papers. Upon graduation he intends to continue his dream of becoming a scientist.

# Acknowledgements

Here, I would like to thank many people for their help and encouragement. Without them, it would have been impossible to finish this project. First of all, I appreciate very much my advisor, David E. Aspnes. His attitude toward science, his keen insight into problems, his solid background on all aspects of physics, and his kindness are always my good example and my motivation to be a professor. I also thank Committee members Prof. Hans Hallen, Prof. Christopher Roland, and Prof. Robert M. Kolbas for their time and consideration.

I must say that our group is very nice. Jon–K. Hansen, a visiting scientist from Norway, helped me significantly at the beginning. I have very happy memories of our discussions during lunch time. I would also like to acknowledge other group members, Ji-Fu Wang, Muharrem Asar, Klaus Flock, Sungjin Kim, Nicholas Stoute, Eric Adles, Inkyo Kim, and Xiang Liu. I will remember them always.

# TABLE OF CONTENTS

List of Tables…….. …..…….……..……vii

List of Figures……...……...…….……..…..viii

Chapter I. Introduction ..... 1

References: ..... 7

Chapter II Theory of Simplified Bond Hyperpolarizability Model ..... 9

2.1 Basic equations. ..... 9
2.2 Anharmonic restoring forces: elementary considerations ..... 12
2.3 Higher-order terms ..... 18
2.3.1 Phenomenological treatment ..... 18
2.3.2 First-principles treatment. ..... 20
2.4 Conclusions ..... 22
References: ..... 23

Chapter III: Dipole-Forbidden Bulk SHG in Crystals with Inversion Symmetry ..... 24

3.1 Introduction ..... 24
3.2 SHG including dipole-forbidden bulk contributions ..... 25
3.2.1 Bond-sum evaluation: quadrupole contributions ..... 26
3.2.2 Bond-sum evaluation: spatial dispersion contributions ..... 29
3.2.3 Signals as a function of depth: field-penetration effects, phase considerations, and relative bulk and surface contributions ..... 31
3.2.4 Determination of relative bulk/surface contributions from anisotropy data. ..... 35
3.3 Conclusions ..... 38
References: ..... 40

Chapter IV Bulk Third Harmonic Generation from Crystalline Si ..... 49

4.1 Introduction ..... 49
4.2 Derivation of expressions for THG ..... 51
4.3 General properties for tetrahedrally bonded semiconductors; connection to fourth-rank susceptibility tensor components ..... 52
4.4 THG responses for specific geometries ..... 55
4.4.1 General considerations ..... 55
4.4.2 Si (111) ..... 58
4.4.3 Si(001) ..... 62
4.4.4 Si (110) ..... 63
4.5 Estimation of relative bulk and surface contributions ..... 65
4.6 Conclusions ..... 66
References ..... 68

Chapter V. Surface Fourth-Harmonic Generation ..... 74

5.1. Introduction ..... 74
5.2. Formulation ..... 74
5.3. (001)Si-$SiO_2$ interface ..... 75
5.4. Comparison with experiment ..... 78
5.5 Conclusions ..... 83
References ..... 85

Chapter VI Dipole-Radiation Model for Terahertz Radiation from Semiconductors ..... 89

6.1 Introduction ..... 89
6.2 Formulation ..... 89
6.3 Comparison to data for THz generation from InP ..... 97
6.4 Conclusions ..... 99
References ..... 100

Chapter VII Spectroscopic Second Harmonic Generation ..... 103

7.1 The spectroscopic properties of the SBHM ..... 103
7.2 Spectroscopic SHG ..... 104

Chapter VIII Conclusions and Proposals ..... 110

8.1 Conclusions ..... 110
8.2 Proposed work ..... 111

Publication and Presentation List: ..... 113

# List of Tables

Table 3.1 cos7ϕ coefficients of *pp* signals of Si interfaces……...42

# List of Figures

Figure 3.1 Experimental configuration for harmonic-generation measurements……..43

Figure 3.2 Bond-vector diagram……...44

Figure 3.3 Anisotropy of SHG for vicinal Si 5° off (111) toward [11-2]……..45

Figure 3.4 Different contributions to the *pp* data of Fig. 3.2……46

Figure 3.5 Anisotropy of SHG for vicinal Si 9° off (001) toward [111]……...…47

Figure 3.6 Different contributions to the data of Fig. 3.4…….48

Figure 4.1 Azimuthal dependences of THG signals for vicinal Si (111) offcut 5° toward $[11\bar{2}]$. Points: data from Ref. 14. Lines: SHBM with longitudinal and transverse components both included (solid) and longitudinal component alone (dashed)…69

Figure 4.2 Best-fit residual as a function of angle of incidence $\theta_1$…….....70

Figure 4.3 As Fig. 4.1, but for on-axis Si(111). The data are from Ref. 20…….....71

Figure 4.4 As Fig. 4.1, but for Si (001). The data are from Ref. 20……..……72

Figure 4.5 As Fig. 4.1, but for Si (001). The data are from Ref. 14……..……73

Figure 5.1 Normalized FHG anisotropies for the (001)Si-$SiO_2$ interface for the polarization combinations *pp*, *ps*, *sp*, and *ss*, as reported in Ref. 2. The solid curves are the results of the SBHM calculations……...86

Figure 5.2 Normalized FHG anisotropies of (001)Si immediately following exposure of the sample to a buffered oxide etch for durations of 0 (top), 10, 20, 30, and 60 min (bottom). The solid curves are the result of SBHM calculations taking into account interface roughening……..……..87

Figure 5.3 Normalized FHG anisotropies for the (001) Si-$SiO_2$ interface for the polarization combinations *pp* and *sp*. The solid curves are the result of SBHM including interface roughness……88

Figure 6.1 *pp*- and *ps*- polarized FIR intensity for (001)InP. Data are from Ref.1…....101

Figure 6.2 Frequency dependence of the bond-charge contribution to the THz intensity.

…….102

Figure 7.1 SHG experimental configuration...…….106

Figure 7.2 Azimuthal-dependent data at difference wavelengths for samples with oxide-nitrided and oxide-oxidized layers with and without RTA on Si (111) surfaces tilted 5º towards (-1 -1 2)……..……...……....107

Figure 7.3 Comparison of hyperpolarizabilities for samples with and without RTA: a, up bond; b, step bond; and c, back bonds…….……..108

Figure 7.4 Comparison of hyperpolarizabilities of the oxide-oxidized and oxide-nitrided samples: a, up bond; b, step bond; and c, back bonds…….……109

# Chapter I. Introduction

Optical probes have unique advantages that become more desirable when higher spatial and temporal resolutions are required. Material damage and the buildup of contamination layers associated with charged-particle exposure do not occur; no special ambient conditions such as ultrahigh vacuum are needed; charging effects in insulators are avoided; long penetration depths allow access to solid-solid and other buried interfaces; and real-time, in-situ monitoring of film growth is possible [1-4]. These advantages are important when exploring new materials, especially in the nanotechnology era, and in applications to biology, where vacuum environments are not relevant. However, optical techniques also have disadvantages when used for surface and interface analysis. Signals are generally weak because of the weak interaction between photons and matter [5], and data are often difficult to interpret [5]. For example, in linear-optical measurements more than 90% of the reflection is due to the bulk, so the signals from the interface/surface are relatively small and hence difficult to analyze.

We can classify optical techniques into two groups: linear and nonlinear. Linear optical techniques involve the linear susceptibility, $\chi^1$, which is a second-rank tensor, and include laser light scattering (LLS), spectroscopic ellipsometry (SE), spectroscopic polarimetry (SP), reflection-difference (-anisotropy) spectroscopy (RDS/RAS), surface photoabsorption (SPA), photoluminescence (PL), etc. Nonlinear optical (NLO) techniques such as second- (SHG), third- (THG), and fourth- (FHG) harmonic generation, involve higher-order susceptibilities such as $\chi_2$, $\chi_3$, and $\chi_4$, which are third-, fourth-, and fifth-rank tensors, respectively. Other NLO possibilities include optical sum-frequency generation (SFG), and stimulated Raman scattering (SRS). Since higher-order tensors are

involved, NLO probes exhibit richer selection rules than linear-optic probes [6], so NLO methods are potentially more powerful than linear-optic approaches as diagnostic tools. Furthermore, because the symmetries of surfaces and interfaces are generally lower than those of the bulk, some NLO approaches can be considered as only surface/interface diagnostic techniques. For example, both SHG and FHG are dipole-forbidden in the bulk of centrosymmetric crystals such as silicon [7-10], so if we ignore higher-order contributions, either of these probes will return information only about Si surfaces and interfaces.

Following the golden days of theoretical research in the 1960s and 1970s, interest in NLO declined as a result of small signal strengths and the difficulties of interpreting data. However, the development of the femtosecond (fs) laser changed the experimental situation. By reducing pulse durations to the fs range, peak fields could be increased substantially without violating the usual limit to signal strength, the average power applied to a sample. The result for SHG was an increase in signal strength by 3 to 4 orders of magnitude. As a consequence, NLO has re-emerged as a viable experimental approach for studying bulk material, thin films, interfaces, and surfaces.

However, until recently, the difficulties in interpreting NLO data remained. As we noted, optical data are already difficult to interpret, and the situation for NLO is even worse. One standard approach is the macroscopic tensor-coefficient representation. Its basis is the relation between polarization and external field [11]. The approach takes advantage of the known symmetry of a crystal. One first uses rotation to project the applied field into the crystal frame, where the polarization is calculated. The polarization is then transformed back into the laboratory frame, from which far-field radiation

expressions are used to obtain the observed harmonic fields. Another method is the Green-function approach, where the NLO problem is solved using the classical E&M Green-function formalism in terms of s- and p- polarized vector waves. This leads to generated fields written as functions of the Fresnel coefficients of the interfaces [12]. The polarizable bond model calculates SHG in terms of the energy resonances associated with the linear response [13], and in fact picks up only part of the total response, the quadrupole contribution. Other methods such as quantum-mechanical evaluation of polarizabilities from band structure, and simple listings of Fourier coefficients of intensity anisotropies observed as the sample is rotated during exposure to a fixed wavelength, are also used in some applications.

Unfortunately, none of the previous formalisms were simple enough to lead to closed-form expressions or to provide useful or complete physical insight about the origins of NLO signals on the atomic scale. These shortcomings were eliminated with the development of the simplified bond-hyperpolarizability model (SBHM) of Powell *et al* [14]. These workers introduced what they termed the SBHM to assist the analysis of their SHG data obtained on Si-insulator interfaces [14, 15]. They showed that observed SHG anisotropies could be described in terms of a hyperpolarizability associated with each of 3 types of interface bonds as opposed to the 11 Fourier or 14 tensor characteristic coefficients of previous work. Moreover, they showed that the 3 hyperpolarizabilities determined from the observed intensity anisotropy of the *pp* polarization combination could be used to predict the observed anisotropies for the *ps*, *sp*, and *ss* combinations. Finally, they obtained analytic descriptions of these anisotropies in terms of these hyperpolarizabilities. The result not only enormously simplified the description of these

SHG data, but also allowed them to be understood in terms of parameters that had direct physical meaning on the atomic scale.

However, the question remains as to how general the SBHM really is. Powell *et al.* did not address a number of NLO phenomena also of interest: FHG from Si-dielectric interfaces, higher-order bulk contributions to SHG in centrosymmetric crystals, THG from bulk Si, or the generation of terahertz (THz) radiation from semiconductor surfaces and interfaces. Owing to the wide wavelength range involved and the relatively weak signals associated with a high-order nonlinearity, FHG is not necessarily a universal probe, but data exist so the model can be critically tested. Bulk contributions from higher-order effects such as spatial-dispersion, magnetic-dipole, and electric-quadrupole interactions have been postulated to be important for SHG from Si, so this needs to be investigated as well. The first nonvanishing NLO contribution to the (001)Si interfaces universally used in integrated-circuits technology is THG. However, THG is not dipole-forbidden in the bulk of centrosymmetric semiconductors, so bulk THG needs to be calculated also. Finally, the generation of THz radiation is important for a number of emerging areas.

In this work we extend and modify the SBHM to fill these gaps by using it to calculate FHG, bulk THG in centrosymmetric crystals, all dipole-forbidden contributions relevant to bulk SHG in centrosymmetric materials, and the generation of THz radiation from semiconductor surfaces and interfaces. With the exception of the THz application, which falls in the sum-frequency category, we concentrate here on harmonic generation, since sum-frequency calculations are a minor extension of the basic approach. We show that the roughness contribution is important for FHG at silicon interfaces, and that this

can be modeled in terms of randomly directed surface bonds. We find that the azimuth dependence of THG on Si (111) can be described accurately in the SBHM provided that the transverse contribution is taken into account, and establish the relationship between the macroscopic susceptibility and the hyperpolarizabilties. To ensure that all contributions are considered we formulate the electric-dipole-forbidden SHG contribution in centrosymmetric crystals from first principles, obtaining results that are clear and unambiguous from the perspective of both physics and mathematics. The capability of obtaining analytic expressions allows us to assess the relative bulk and surface contributions to SHG, and despite previous speculations to the contrary, we find that the bulk contribution here is minor. Extending the SBHM to THz generation, we obtain a very simple dipole-radiation expression to describe the two mechanisms giving rise to THz generation in one analytical expression.

The outline of this work is as follows. In Ch. II, we review the basic theory of the model. We start from Maxwell's Equations, and with a few assumptions formulate the SBHM. We also review the previous work of Powell *et al.* and Wang *et al.* In Ch. III, we evaluate the bulk contribution to SHG, including not only electric-dipole-allowed terms in both the bulk and at the interface, but also the electric-dipole-forbidden contributions: spatial dispersion, magnetic-dipole, and electric-quadrupole effects. We evaluate these for bulk Si, and show that their contribution is small compared to that of the interface. In Ch. IV, we discuss bulk THG generation, showing that the transverse contribution is important and describing how to we add it to the theory. In Ch. V, we treat FHG of silicon, showing how interface-roughness contributions can be identified and described. In Ch. VI, we extend the SBHM to calculate THz generation from semiconductor

surfaces and interfaces. In Ch. VII, we provide a brief discussion of the possibilities fro NLO spectroscopy. Finally, in Ch. VIII we draw some conclusions from our work and propose possible future directions.

## *References:*


[1] G. Lüpke, Characterization of semiconductor interfaces by second-harmonic generation, Surface Science Reports **35**, 75 (1999).

[2] J. F. McGilp, A review of optical second-harmonic and sum-frequency generation at surfaces and interfaces, Journal of Physics **D29**, 1812 (1996).

[3] J. F. McGilp, Optical characterization of semiconductor surfaces and interfaces, Progress in Surface Science, **49**, 1 (1995).

[4] D. E. Aspnes, Linear and nonlinear spectroscopy of surfaces and interfaces, Physica Status Solid, **a188**, 1353 (2001).

[5] D. E. Aspnes, Real-time optical analysis and control of semiconductor epitaxy: progress and opportunity, Solid State Communications, **101**, 85 (1997).

[6] Y. R. Shen, The Principles of nonlinear optics (wiley, New York, 1984).

[7] T. F. Heinz, C. K. Chen, D. Ricard, and Y. R. Shen, Phys. Rev. Lett. **48**, 478 (1982).

[8] T. F. Heinz, M. M. T. Loy, and W. A. Thompson, Phys. Rev. Lett. **54**, 63 (1985).

[9] J. A. Litwin, J. E. Sipe, and H. M. van Driel, Phys. Rev. B **31**, 5543 (1983).

[10] H. W. K. Tom, T. F. Heinz, and Y. R. Shen, Phys. Rev. Lett. **51**, 1983 (1983).

[11] G. Lüpke, D. J. Bottomley, and H. M. van Driel, J. Opt. Soc. Am. B **11**, 33 (1994).

[12] J. E. Sipe, New Green –function formalism for surface optics, J. Opt. Soc. Am. **B4**, 481 (1987).

[13] J. E. Mejia and B. S. Mendoza, Polarizable-bond model for surface second-harmonic generation at Si(111): H (1 x 1), Physica Status Solid, **a188**, 1393 (2001).

[14] G. D. Powell, J.-F. T. Wang, and D. E. Aspnes, Phys. Rev. B **65**, 205320 (2002).

[15] J.-F. T. Wang, G. D. Powell, R. S. Johnson, G. Lucovsky, and D. E. Aspnes, J. Vac. Sci. Technol. B **20**, 1699 (2002).

# Chapter II Theory of Simplified Bond Hyperpolarizability Model

## *2.1 Basic equations.*

All electromagnetic phenomena can be derived from Maxwell's Equations. In SI units these are

$$\nabla \cdot \vec{D} = \rho\,, \tag{2.1.a}$$

$$\nabla \cdot \vec{B} = 0\,, \tag{2.1.b}$$

$$\nabla \times \vec{E} + \frac{\partial \vec{B}}{\partial t} = 0\,, \tag{2.1.c}$$

$$\nabla \times \vec{H} - \frac{\partial \vec{D}}{\partial t} = \vec{J}\,. \tag{2.1.d}$$

Here, ρ and **J** are the charge and current densities, respectively, and $\vec{D}$, $\vec{B}$, $\vec{E}$, and $\vec{H}$ are the displacement field, magnetic flux density, electric field, and magnetic field intensity, respectively. For NLO calculations ρ and **J** are normally set equal to zero.

Taking the time derivative of Eq. (2.1.d), using Eq. (2.1.c), setting the magnetic permeability μ = 1, where $\vec{B} = \mu\vec{H}$, and using

$$\vec{D} = \vec{E} + \vec{P} \tag{2.1.e}$$

where $\vec{P}$ is polarization (dipole density in the dipole approximation), we have

$$[\nabla \times (\nabla \times) + \frac{\partial^2}{\partial t^2}]\vec{E}(\vec{r},t) = -\frac{\partial^2}{\partial t^2}\vec{P}(\vec{r},t)\,. \tag{2.2.a}$$

We now separate $\vec{P}$ into linear and nonlinear parts:

$$\vec{P} = \vec{P}_L + \vec{P}_{NL}\,, \tag{2.2.b}$$

which leads to

$$[\nabla \times (\nabla \times) + \varepsilon \frac{\partial^2}{\partial t^2}]\vec{E}(\vec{r},t) = -\frac{\partial^2}{\partial t^2}\vec{P}_{NL}. \qquad (2.3.a)$$

Here, $\varepsilon$ is the dielectric function, which is defined as

$$\vec{D} = \varepsilon\vec{E} = \vec{E} + \vec{P}_L. \qquad (2.3.b)$$

If we ignore the nonlinear polarization, Eq. (2.2.a) reduces to the familiar form

$$[\nabla \times (\nabla \times) + \varepsilon \frac{\partial^2}{\partial t^2}]\vec{E}(\vec{r},t) = 0. \qquad (2.3.c)$$

From Eq. (2.3.a), we can obtain the far-field limit of the radiation field within the dipole approximation. This is

$$\vec{E}_{ff} = Z\frac{ck^2}{4\pi}(\hat{k} \times \vec{P}_{NL}) \times \hat{k} \cdot \frac{e^{ikr}}{r}, \qquad (2.4)$$

where Z is the impedance of the medium. We emphasize that $\vec{P}_{NL}$ is a total effective nonlinear dipole density, which is a nonlocal function of the field and can be divided into electric-dipole, quadupole, and magnetic-dipole (but not spatial-dispersion) contributions, and so on.

The problem now is to calculate $\vec{P}_{NL}$. In the linear case $\vec{P}$ is related to the external (driving) field by the linear susceptibility according to

$$\vec{P}(\vec{r},t) = \int_{-\infty}^{\infty} \chi^1(\vec{r} - \vec{r}', t - t') \cdot \vec{E}(\vec{r}', t')d\vec{r}'dt'. \qquad (2.5.a)$$

By Fourier-transforming the above expression we have

$$\vec{P}(\vec{r},t) = \vec{P}(\vec{k},\omega) = \chi^1(\vec{k},\omega) \cdot \vec{E}(\vec{k},\omega), \qquad (2.5.b)$$

where

$$\chi^{1}(\vec{k},\omega) = \int_{-\infty}^{\infty} \chi^{1}(\vec{r},t) e^{-i\vec{k}\cdot\vec{r}+i\omega t} d\vec{r}dt\,. \tag{2.5.c}$$

Using this expression in Maxwell's Equations in the linear-optics case leads to the familiar reflection and refraction laws.

In the nonlinear case, if the applied field $\vec{E}$ is sufficiently weak compared to internal fields but still a strong laser field, then $\vec{P}$ can be expanded as a power series of $\vec{E}$ to obtain

$$\begin{aligned}\vec{P}(\vec{r},t) = & \int_{-\infty}^{\infty} \chi^{(1)}(\vec{\mathrm{r}} - \vec{\mathrm{r}}', \mathrm{t} - \mathrm{t}') \cdot \vec{\mathrm{E}}(\vec{\mathrm{r}}', \mathrm{t}') \mathrm{d}\vec{\mathrm{r}}' dt' + \\ & \int_{-\infty}^{\infty} \chi^{(2)}(\vec{\mathrm{r}} - \vec{\mathrm{r}}_1, \mathrm{t} - \mathrm{t}_1; \vec{\mathrm{r}} - \vec{\mathrm{r}}_2, \mathrm{t} - \mathrm{t}_2) : \\ & \vec{E}(\vec{r}_1, \mathrm{t}_1) \vec{E}(\vec{r}_2, \mathrm{t}_2) \mathrm{d}\vec{\mathrm{r}}_1 dt_1 \mathrm{d}\vec{\mathrm{r}}_2 dt_2 + \\ & \int_{-\infty}^{\infty} \chi^{(3)}(\vec{\mathrm{r}} - \vec{\mathrm{r}}_1, \mathrm{t} - \mathrm{t}_1; \vec{\mathrm{r}} - \vec{\mathrm{r}}_2, \mathrm{t} - \mathrm{t}_2, \vec{\mathrm{r}} - \vec{\mathrm{r}}_3, \mathrm{t} - \mathrm{t}_3) \vdots \\ & \vec{E}(\vec{r}_1, \mathrm{t}_1) \vec{E}(\vec{r}_2, \mathrm{t}_2) \vec{E}(\vec{r}_3, \mathrm{t}_3) \mathrm{d}\vec{\mathrm{r}}_1 dt_1 \mathrm{d}\vec{\mathrm{r}}_2 dt_2 \mathrm{d}\vec{\mathrm{r}}_3 dt_3 + \cdots\end{aligned} \tag{2.6.a}$$

where $\chi^{(n)}$ is the n$^{\text{th}}$ order susceptibility. If we expand $\vec{E}$ as a sum of monochromatic plane waves

$$\vec{E}(\vec{r},t) = \sum_j \vec{E}(\vec{k}_j, \omega)\,, \tag{2.6.b}$$

we can Fourier-transform Eq. (2.6.a) to obtain

$$\vec{P}(\vec{\mathrm{k}},\omega) = \vec{P}^{(1)}(\vec{\mathrm{k}},\omega) + \vec{P}^{(2)}(\vec{\mathrm{k}},\omega) + \vec{P}^{(3)}(\vec{\mathrm{k}},\omega) + \cdots, \tag{2.6.c}$$

where

$$
\begin{aligned}
&\vec{P}^{(1)}(\vec{\mathrm{k}},\omega) = \chi^{(1)}(\vec{k},\omega)\cdot\vec{E}(\vec{k},\omega),\\
&\vec{P}^{(2)}(\vec{\mathrm{k}},\omega) = \chi^{(2)}(\vec{k}=\vec{k}_i+\vec{k}_j,\omega=\omega_i+\omega_j):\\
&\qquad\qquad \vec{E}(\vec{k}_i,\omega_i)\vec{E}(\vec{k}_j,\omega_j),\\
&\vec{P}^{(3)}(\vec{\mathrm{k}},\omega) = \chi^{(3)}(\vec{k}=\vec{k}_i+\vec{k}_j+\vec{k}_l,\omega=\omega_i+\omega_j+\omega_l):\\
&\qquad\qquad \vec{E}(\vec{k}_i,\omega_i)\vec{E}(\vec{k}_j,\omega_j)\vec{E}(\vec{k}_l,\omega_l),
\end{aligned}
\tag{2.6.d}
$$

and

$$
\begin{aligned}
&\chi^{(n)}(\vec{k}=\vec{k}_1+\vec{k}_2+\cdots+\vec{k}_n,\omega=\omega_1+\omega_2+\cdots+\omega_n)\\
&\quad=\int_{-\infty}^{\infty}\chi^{n}(\vec{r}-\vec{r}_1,t-t_1;\cdots;\vec{r}-\vec{r}_n,t-t_n)\\
&\quad\times e^{-i[\vec{k}_1\cdot(\vec{r}-\vec{r}_1)-\omega_1(t-t_1)+\cdots+\vec{k}_n\cdot(\vec{r}-\vec{r}_n)-\omega_n(t-t_n)]}d\vec{r}_1dt_1\cdots d\vec{r}_ndt_n
\end{aligned}
\tag{2.6.e}
$$

It follows that

$$
\vec{P}_{NL}(\vec{\mathrm{k}},\omega) = \vec{P}^{(2)}(\vec{\mathrm{k}},\omega)+\vec{P}^{(3)}(\vec{\mathrm{k}},\omega)+\cdots. \tag{2.7}
$$

Hence once we know the nonlinear susceptibilities, we can obtain the nonlinear polarizations and therefore calculate in general the generated nonlinear fields. However, only a very few nonlinear susceptibilities are known, and the method is still mathematically very difficult. Furthermore this macroscopic description has no explicit connection to the microscopic properties of materials on the atomic scale, such as bond angles, strengths, and hyperpolarizabilities

## *2.2 Anharmonic restoring forces: elementary considerations.*

To facilitate the interpretation of their SHG data Powell, Wang, and co-workers developed the simplified bond-hyperpolarizability (SBHM) model [1-2]. Like the tensor-coefficient description, the SBHM is phenomenological, but instead of simply listing coefficients consistent with crystal symmetry, it derives its parameters from a one-dimensional force model for the motions of bond or free charges that result from the

application of an external field. The second difference is that the far-field radiation $\vec{E}_{ff}$ is calculated using the expression for radiation from an accelerated charge in the dipole approximation. As a result the SBHM is essentially the NLO version of the Ewald-Oseen extinction theory of linear optics [3-4], with the exception of that the SBHM includes bond directionality and the need to solve the radiation problem self-consistently is eliminated, since the generated radiation is at a different frequency and also orders of magnitude weaker than the driving field. The bond charges are treated separately and the overall radiation obtained by summing the individual radiation fields over the unit cell, then integrated from surface to bulk. It is also a semiclassical model, which assumes that the charges are particles and the radiation field can be described as a wave.

The original assumptions of the SBHM are sufficient to treat the Powell-Wang application to interface SHG of centrosymmetric materials with bulk contributions ignored, and our application to interface FHG, which also involves centrosymmetric crystals. These assumptions are: (1) for a given bond the only charge motion that is relevant is that along the bond direction; (2) the bond directions themselves are those of the bulk material; and (3) the observed intensity is a result of the coherent superposition of radiation from the individual bonds calculated in dipole approximation. The first assumption follows from the idea that bonds are essentially rotationally symmetric, which eliminates transverse contributions for SHG and FHG. However, as in linear optics, the assumption of rotational symmetry does not eliminate the transverse contributions in THG, so for bulk THG we will need to extend the SBHM by considering the transverse motions as well. The second assumption follows from empirical observation.

The third assumption is an adaptation of one of the concepts used in the derivation of the Ewald-Oseen extinction theorem of linear optics [3-4]. As mentioned above, the SBHM differs from the Ewald-Oseen treatment in two important ways: the SBHM requires the added assumption of bond directionality at the microscopic level, and self-consistency is not necessary since the generated radiation does not interact with driving field. Calculation of higher-order NLO effects requires further elaboration: to evalute bulk SHG in the centrosymmetric materials we need to consider magnetic-dipole, electric-quadrupole, and spatial-dispersion contributions, and for THz generation, free-carrier contributions as well.

We now consider the evaluation of the dipole density. The dipole moment is defined as follows for the discrete and continuum cases:

$$\begin{aligned}\vec{P} &= \frac{1}{(vol)}\sum_i q(\vec{r}-\vec{r}_{0i}) \\ &= \int n(\vec{r}')\rho(\vec{r}')\Delta\vec{r}(\vec{r}')\, d^3\vec{r}'\end{aligned} \tag{2.8}$$

where in the upper line $\vec{r}_0$ is the equilibrium position of the charge before the external field is applied and in the lower line $n(\vec{r})$ is the number density and $\Delta\vec{r}(\vec{r}')$ is the local displacement of $\rho(\vec{r}')$ as a result of the laser field . We consider the discrete case of a point bond charge q moving in the response of an applied field $\vec{E}(\vec{r},t)=\vec{E}_0 e^{-i\omega t}$. After the field is applied the position of q is assumed to be described by

$$\begin{aligned}\vec{r} &= \vec{r}_0 + \Delta\vec{r}_1 e^{-i\omega t} + \Delta\vec{r}_2 e^{-2i\omega t} + \cdots \\ &= \vec{r}_0 + (\Delta r_1 e^{-i\omega t} + \Delta r_2 e^{-2i\omega t} + \Delta r_3 e^{-3i\omega t} + \Delta r_4 e^{-4i\omega t}\cdots)\hat{b}\end{aligned} \tag{2.9}$$

where $\Delta\vec{r} = \vec{r} - \vec{r}_0$ is the displacement of q. In the second line we have written $\Delta\vec{r}$ as a power series of $e^{-i\omega t}$ and have made the basic SBHM assumption that we need consider only the motion of q in the direction $\hat{b}$ of the current bond of interest. With these equations and assumptions, $\Delta\vec{r}$ can be calculated with a one-dimensional force equation, which for the $j^{th}$ bond takes the form

$$\begin{aligned}\vec{F} &= m\frac{d^2\vec{r}}{dt^2} \\ &= q_j\vec{E}\cdot\hat{b}_j e^{-i\omega t} - \kappa_1\Delta\vec{r} - \kappa_2\Delta\vec{r}^{\,2} - \\ &\quad \kappa_3\Delta\vec{r}^{\,3} - \kappa_4\Delta\vec{r}^{\,4} - \cdots - \gamma\frac{d\Delta\vec{r}}{dt},\end{aligned} \tag{2.10}$$

where $\vec{E}$ is the externally applied driving field; $\kappa_1$ is the harmonic (linear or Hooke's Law) polarizability; $\kappa_2$, $\kappa_3$, and $\kappa_4$ are the second-, third-, and fourth-order anharmonic longitudinal hyperpolarizabilities; and $\gamma$ represents frictional loss. The terms that we retain are determined by the order of harmonic generation that needs to be calculated. From Eqs. (2.9) and (2.10) we obtain for the linear response of the $j^{th}$ bond:

$$\Delta\vec{r}_{1j} = \frac{q_j}{-m\omega^2 + \kappa_1 - i\gamma\omega}(\vec{E}\cdot\hat{b}_j)\hat{b}_j, \tag{2.11.a}$$

which allows us to define the linear polarizability $\alpha_{1j}$ of the $j^{th}$ bond as

$$\alpha_{1j} = \frac{q_j}{-m\omega^2 + \kappa_1 - i\gamma\omega}, \tag{2.11.b}$$

in which case we can write

$$\Delta\vec{r}_{1j} = \alpha_{1j}(\vec{E}\cdot\hat{b}_j)\hat{b}_j. \tag{2.11.c}$$

Proceeding to second order we find

$$\begin{aligned}\Delta\vec{r}_{2j} &= \frac{-\kappa_2 \Delta r_{1j}^2}{-4m\omega^2 + \kappa_1 - i\gamma 2\omega} \\ &= \frac{-\kappa_2 (\vec{E}\cdot\hat{b}_j)^2 \hat{b}_j}{-4m\omega^2 + \kappa_1 - i\gamma 2\omega} \cdot \frac{q_j^2}{(-m\omega^2 + \kappa_1 - i\gamma\omega)^2}\end{aligned} \tag{2.12.a}$$

This allows us to define a second-order nonlinear hyperpolarizability as

$$\alpha_{2j} = \frac{-\kappa_2}{-4m\omega^2 + \kappa_1 - i\gamma 2\omega} \cdot \frac{q_j^2}{(-m\omega^2 + \kappa_1 - i\gamma\omega)^2} \tag{2.12.b}$$

It follows that

$$\Delta\vec{r}_{2j} = \alpha_{2j} (\vec{E}\cdot\hat{b}_j)^2 \hat{b}_j . \tag{2.12.c}$$

Similarly, for third- and fourth-order displacements we have

$$\Delta\vec{r}_{3j} = \alpha_{3j} (\vec{E}\cdot\hat{b}_j)^3 \hat{b}_j , \tag{2.13.a}$$

$$\Delta\vec{r}_{4j} = \alpha_{4j} (\vec{E}\cdot\hat{b}_j)^4 \hat{b}_j . \tag{2.13.b}$$

Even though we have considered only longitudinal displacements here, we will see when we treat THG in Ch. IV, the transverse displacements have the same form as above.

By substituting Eqs. (2.11.c), (2.12.c), (2.13.a), and (2.13.b) into (2.8), we can obtain the linear, second-, third-, and fourth-order nonlinear dipole densities induced by the external field. Up to fourth order these are

Linear:

$$\vec{P}^{(1)} = q\sum_i \alpha_{1i} \hat{b}_i \hat{b}_i \cdot \vec{E} \tag{2.14.a}$$

Second-order:

$$\vec{P}^{(2)} = q\sum_i \alpha_{2i} \hat{b}_i \hat{b}_i \hat{b}_i \cdot\cdot \vec{E}\vec{E} \tag{2.14.b}$$

Third-order:

$$\vec{P}^{(3)} = q\sum_i \alpha_{3i}\hat{b}_i\hat{b}_i\hat{b}_i\hat{b}_i \cdots \vec{E}\vec{E}\vec{E} \tag{2.14.c}$$

Fourth-order:

$$\vec{P}^{(4)} = q\sum_i \alpha_{4i}\hat{b}_i\hat{b}_i\hat{b}_i\hat{b}_i\hat{b}_i \cdots\cdots \vec{E}\vec{E}\vec{E}\vec{E} \tag{2.14.d}$$

Hence according to the classical-E&M far-field radiation equation we have the radiation fields

Linear:

$$\vec{E}_{ff}^{(1)} \propto [\underline{I} - \hat{k}\hat{k}]\cdot\{\sum_i \alpha_{1i}\hat{b}_i\hat{b}_i\}\cdot\vec{E}\,; \tag{2.15.a}$$

SHG:

$$\vec{E}^{2} \propto [\underline{I} - \hat{k}\hat{k}]\cdot\{\sum_i \alpha_{2i}\hat{b}_i\hat{b}_i\hat{b}_i\}\cdot\cdot\vec{E}\vec{E}\,; \tag{2.15.b}$$

THG:

$$\vec{E}^{3} \propto [\underline{I} - \hat{k}\hat{k}]\cdot\{\sum_i \alpha_{3i}\hat{b}_i\hat{b}_i\hat{b}_i\hat{b}_i\}\cdots\vec{E}\vec{E}\vec{E}\,; \tag{2.15.c}$$

FHG:

$$\vec{E}^{4} \propto [\underline{I} - \hat{k}\hat{k}]\cdot\{\sum_i \alpha_{4i}\hat{b}_i\hat{b}_i\hat{b}_i\hat{b}_i\hat{b}_i\}\cdots\vec{E}\vec{E}\vec{E}\vec{E}\,. \tag{2.15.d}$$

The expressions can be written as sums over the bond vectors of the unit cell because the radiation fields are additive. These summations are generally straightforward to evaluate, and in the simple case of tetrahedrally bonded semiconductors, closed-form expressions can be obtained. The projection operator $[\underline{I} - \hat{k}\hat{k}]$ can also be written $[\,\hat{p}\hat{p} + \hat{s}\hat{s}\,]$, where $\hat{p}$ and $\hat{s}$ are the unit vectors in the direction of the *p*- and *s*-polarized radiation, respectively.

## *2.3 Higher-order terms*

### 2.3.1 Phenomenological treatment

In the above, radiation is treated in the dipole approximation assuming anharmonic restoring forces. However, the dipole contribution vanishes in the bulk of materials with inversion symmetry. But we know from multipole expansions [5] that radiation can also result from higher-order contributions. These include electric quadrupole, magnetic dipole, and spatial dispersion. Using SHG as an example, the effective nonlinear polarization can be written

$$\begin{aligned}\vec{P}_{eff}^{(2)}(2\omega) &= \vec{P}^{(2)}(2\omega) - \nabla\cdot\vec{Q}^{(2)}(2\omega) \\ &\quad + \frac{c}{i2\omega}\nabla\times\vec{M}^{(2)}(2\omega) + \cdots\end{aligned} \tag{2.16}$$

where $\vec{P}^{(2)}$, $\vec{Q}^{(2)}$, $\vec{M}^{(2)}$ are the source terms giving rise to electric-dipole, electric-quadrupole, and magnetic-dipole contributions, respectively. Equation (2.16) is valid when the dimensions of the volume element are small compared to the characteristic length over which the field varies. These three terms can also be expressed in terms of the applied external field through susceptibility tensors [6]:

$$\vec{P}^{(2)}(2\omega) = \vec{\vec{\chi}}^{D} : \vec{E}(\omega)\vec{E}(\omega) + \vec{\vec{\chi}}^{P} : \vec{E}(\omega)\nabla\vec{E}(\omega); \tag{2.17.a}$$

$$\vec{Q}^{(2)}(2\omega) = \vec{\vec{\chi}}^{Q} : \vec{E}(\omega)\vec{E}(\omega); \tag{2.17.b}$$

$$\vec{M}^{(2)}(2\omega) = \vec{\vec{\chi}}^{M} : \vec{E}(\omega)\vec{E}(\omega). \tag{2.17.c}$$

For a medium with inversion symmetry $\vec{\vec{\chi}}^{D}$ vanishes, so the first term in Eq. (2.17.a) is zero. Furthermore, since $\vec{\vec{\chi}}^{M}$ is proportional to the third-rank unit antisymmetric tensor,

$\vec{M}^{(2)}(2\omega)$ also vanishes for a material with inversion symmetry in both space and time. As a result, when calculating the bulk contribution to SHG for materials with inversion symmetry, such as Si, from a polarization-expansion perspective only the spatial-dispersion and electric-quadrupole terms need be evaluated. In the next section we show how to do this systematically from first principles.

We first consider the electric-quadrupole contribution. According to classical E&M theory [5], the electric quadrupole is defined as

$$Q_{i,j}(2\omega) = \frac{1}{V}\sum_n q_n (3\Delta x_{n,i}\Delta x_{n,j} - \Delta x_n^2 \delta_{ij}), \tag{2.18}$$

From these expression the $2\omega$t electric-quadrupole contribution is clearly proportional to the square of the linear displacement, and hence to the square of the linear susceptibility, as obtained by Bloembergen *et. al* [7] and Mendoza *et. al.* [8] With Eq. (2.18) and knowledge of the linear displacement, the quadrupole contribution to the far-field radiation can be calculated. We will leave the details to the following chapter.

As stated above, the spatial variation (spatial dispersion) of the incident field in the medium can also induce bulk SHG even in materials with inversion symmetry. The physics is straightforward: if $\vec{E}$ has a spatial dependence then in principle the field at one end of a dipole is larger than the field at the other end, leading to an automatic asymmetry. In our previous analyses of SHG from Si, we attributed the entire response to the interface region and ignored the bulk. The assumption was justified on the grounds that the bonding asymmetry at the interface is significant, even if the interface is only one or two atomic layers thick. However, the spatial-dispersion term can easily be added to the model. For the $j^{\text{th}}$ bond we expand $\vec{E}$ at the charge site according to

$$\vec{E}_j = \vec{E}_{j0} + \Delta\vec{r}_j \bullet \nabla\vec{E}\,, \tag{2.19}$$

where $\Delta\vec{r}_j$ is from Eq. (2.9.2). Substituting Eqs. (2.19) and (2.9.2) into the force equation introduces $\nabla\vec{E}$, and therefore spatial dispersion.

### 2.3.2 First-principles treatment.

In principle the above provides a complete frame for performing SBHM calculations for NLO, but we show here that it is also possible to take a more fundamental view, allowing the far-field radiation to be evaluated from first principles. The advantages of a first-principles method are 1) a better understanding of the principles behind, and the physical meaning of, the various terms than what is provided by the purely phenomenological treatment, and 2) the approach is more systematic. We will evaluate dipole and first-forbidden bulk contributions to SHG in centrosymmetric materials as an example of this method.

We begin with the Green-function expression for the 4-potential of a point charge q propagating in free space:

$$(\phi(\vec{r},t), \vec{A}(\vec{r},t)) = \frac{1}{c}\int d^3r'dt'(c\rho(\vec{r}',t'), \vec{J}(\vec{r}',t'))\frac{\delta(t-t'-\frac{1}{c}|\vec{r}-\vec{r}'|)}{|\vec{r}-\vec{r}'|}\,, \tag{2.20.a}$$

where

$$\rho(\vec{r}',t') = q\delta(\vec{r}' - \vec{r}_o - \Delta\vec{r}(t'))\,; \tag{2.20.b}$$

$$\vec{J}(\vec{r}',t') = \rho(\vec{r}',t')\frac{d}{dt'}\Delta\vec{r}(t')\ ; \tag{2.20.c}$$

and where for each bond $j$ with unit bond vector $\hat{b}_j$, $\Delta\vec{r}_j(t')$ has the form of Eq. (2.9.b). From the force equation we can obtain the vector potential $\vec{A}(\vec{r},t)$ in the far–field region as

$$\vec{A}(\vec{r},t) = \frac{-i\omega q}{rc} e^{ikr - i\omega t}\ e^{-i\vec{k}\bullet\vec{r}_o} \cdot \times \sum_j e^{-i\vec{k}\bullet\Delta\vec{r}_j(t)}\ \hat{b}_j\,[\Delta r_{j1} + 2\Delta r_{j2}\, e^{ikr - i\omega t} e^{-i\vec{k}\bullet\vec{r}_o} e^{-i\vec{k}\bullet\Delta\vec{r}_j(t)}] \tag{2.21}$$

In Eq. (2.21) we substitute the complex wave vector $\tilde{k} = \tilde{k}(\omega)$ of the material for the free-space value, which is acceptable because we are considering optically isotropic materials at a discrete frequency $\omega$. The magnetic-dipole and bulk-quadrupole terms result from the expansion of the exponential, $\Delta\mathbf{r}_j$, next to the summation, although in this application the magnetic-dipole contribution vanishes.

Evaluating the far-field radiation $\vec{E}_{ff}$ explicitly we find

$$\begin{aligned}\vec{E}_{ff} = \frac{qk^2}{r}(\tilde{I} - \hat{k}\hat{k})\bullet\sum \{\hat{b}_j \frac{q(\hat{b}_j\bullet\vec{E}_o)}{\kappa_1 - m\omega^2} e^{ikr - i\omega t} e^{i(\vec{k}_o - \vec{k})\bullet\vec{r}_o} \\ + \hat{b}_j \frac{q^2(\hat{b}_j\bullet\vec{E}_o)^2}{(\kappa_1 - m\omega^2)^2(\kappa_1 - 4m\omega^2)}[-i(\hat{b}_j\bullet\vec{k})(\kappa_1 - 4m\omega^2) \\ + 2i(\hat{b}_j\bullet\vec{k}_o)(\kappa_1 - m\omega^2) - 2\kappa_2]e^{2ikr - 2i\omega t}\ e^{2i(\vec{k}_o - \vec{k})\bullet\vec{r}_o}\ \},\end{aligned} \tag{2.22}$$

where the projection operator $(\tilde{I} - \hat{k}\hat{k})$ can also be written $(\hat{s}\hat{s} + \hat{p}\hat{p})$. The first term in braces is the linear-optic response, and the remaining three describe SHG. The physical origin of the three SHG terms are clear from the development: the first term, which involves the outgoing wave vector, is the electric-quadrupole contribution; the second term, which involves the incoming wave vector, arises from spatial dispersion; and the

third term, which depends only on the anharmonic restoring force, reduces to the contribution from asymmetric bonding at the interface for SHG from centrosymmetric crystals. The intensity is proportional to the absolute square of the far field after all contributions have been taken into account.

The above first-principles calculation can be applied to all other nonlinear optical processes, including those such as sum- and difference-frequency mixing involving two or more incident waves. A good example is the generation of THz radiation from semiconductors that are illuminated by ultrafast laser pulses. THz generation involves both bond charges and free carriers, and we will apply the one-dimensional force law to both. We will discuss the generation of THz radiation in Ch.VI.

## *2.4 Conclusions*

In this chapter we provide a detailed description of nonlinear harmonic generation at the atomic scale using a one-dimensional force equation including anharmonic restoring forces. Two ways are presented: the phenomenological approach of the original SBHM, and the first-principles approach that we will use for effects of higher order than SHG.

## *References:*


[1] G. D. Powell, J.-F. T. Wang, and D. E. Aspnes, Phys. Rev. B **65**, 205320 (2002).

[2] J.-F. T. Wang, G. D. Powell, R. S. Johnson, G. Lucovsky, and D. E. Aspnes, J. Vac. Sci. Technol. B **20**, 1699 (2002).

[3] C. W. Oseen, Ann. Phys. (Leipzig) **48**, 1 (1915).

[4] P. P. Ewald, Ann. Phys. (Leipzig) **49**, 1 (1916).

[5] J. D. Jackson. Classical Electrodynamics. John Wiley & Sons, Inc., New York, Third edition, 1998.

[6] P. Guyot-Sionnest and Y. R. Shen, Phys. Rev. **B38**, 7985 (1988).

[7] N. Bloembergen, R. K. Chang, S. S. Jha, and C. H. Lee, Physical Review **174**, 813 (1968).

[8] B. S. Mendoza and W. L. Mochán, Phys. Rev. **B55**, 2489 (1997).

# Chapter III: Dipole-Forbidden Bulk SHG in Crystals with Inversion Symmetry

## *3.1 Introduction*

Second-harmonic generation (SHG) was the first nonlinear-optical phenomena studied [1], and has now been investigated intensively by both theory and experiment [2-5]. Amplified femtosecond laser pulses have recently been used to study SHG from semiconductor surfaces/interfaces [6-9]. As noted in the Ch. I, these investigations are of interest because SHG are electric-dipole-forbidden in the bulk of materials with inversion symmetry, which makes them particularly attractive for surface/interface studies provided that higher-order bulk contributions can be ignored. As a result, SHG is already widely used for studying semiconductor surfaces and interfaces [10-15].

However, since the capability of obtaining SHG data as a continuous function of wavelength is limited, SHG results are usually in the form of anisotropy, i.e., dependences of intensity as a function of sample azimuth angle $\phi$ for the four possible combinations of incident and observed polarizations, *pp*, *ps*, *sp*, and *ss* [16]. Here, *p* and *s* refer to *p*- and *s*-polarization, with the first and second letters referring to the polarization of the incident and observed beams, respectively. A large number of systems have been investigated by SHG and include semiconductor, metal, and bio-systems.

In particular the Si (001), (110), and (111) interfaces have been studied thoroughly. Lüpke [16] gave a complete description of SHG from Si in phenomenological terms. However, this description not only requires far more parameters than is needed in the

SBHM, but being completely phenomenological also cannot address the problem of the relative magnitude of the bulk and interface contributions to SHG.

In this chapter, we will give analytical expressions of dipole forbidden SHG for silicon interfaces using the SBHM. We will also simulate the SHG data taking into account the bulk contribution; which we evaluate, and then estimate the relative bulk and surface contributions for SHG. Numerical calculations are given for the further proof of relative bulk and surface contributions.

## *3.2 SHG including dipole-forbidden bulk contributions*

Because Si has inversion symmetry and hence SHG signals from the bulk are dipole-forbidden, Si SHG has received particular attention. Indeed, in previous work [20, 21] our group considered only the interface contribution, and obtained excellent agreement between theory and experiment. However, the question remains: if we consider higher-order contributions, can bulk SHG still be ignored? The issue arises because the interface contribution originates essentially from one monolayer, whereas the bulk contribution comes from many layers. Lüpke *et al*. [16] indicated that the bulk contributions could not be neglected relative to that of the interface, and in fact argued that the bulk contribution accounted for fully half of the observed SHG signal from oxidized Si. Since this issue is still unresolved, we here use the SBHM developed in Ch. 2 to estimate the first-forbidden bulk contributions to SHG by obtaining and evaluating analytic expressions, then directly comparing predicted anisotropies to experiment. We find that bulk contributions are indeed minor, certainly less than half the interface contributions. However, the coherent superposition of bulk and interface contributions is important and cannot be neglected.

### 3.2.1 Bond-sum evaluation: quadrupole contributions

Starting from the first-principles Eq. (2.22), if we assume that all bonds are identical, as is the case in the bulk of the cubic semiconductors, we can obtain the total quadrupole contribution by integrating over the penetration depth. We first obtain the analytical expression for the on-axis case. The configuration is shown in Fig. 3.1. The laboratory axes are in the left of the figure. Light is incident on the sample surface at an angle of incidence $\theta_i$. The generated wave leaves at an angle $\theta_o$, which we take to be equal to the angle of incidence. For vicinal samples we tilt the crystal axes by the vicinal angle $\gamma$ using the rotation matrix

$$M(T) = \begin{pmatrix} \cos\gamma & 0 & \sin\gamma \\ 0 & 1 & 0 \\ -\sin\gamma & 0 & \cos\gamma \end{pmatrix}. \tag{3.1}$$

We next rotate about the unit surface normal vector $\hat{n}$ using the rotation matrix

$$M(R) = \begin{pmatrix} \cos\phi & \sin\phi & 0 \\ -\sin\phi & \cos\phi & 0 \\ 0 & 0 & 1 \end{pmatrix}. \tag{3.2}$$

In the following we obtain analytic expressions of quadrupole contributions only for singular (on-axis) surfaces, but we use tilt angles when doing numerical calculations to simulate data.

We consider first Si (111). Here, the bond vectors in the laboratory frame are

$$\hat{b}_1 = \hat{z}\,, \tag{3.3.a}$$

$$\hat{b}_2 = \sin\beta\,\hat{x} + \cos\beta\,\hat{z}\,, \tag{3.3.b}$$

$$\hat{b}_3 = -\frac{1}{2}\hat{x}\sin\beta + \frac{\sqrt{3}}{2}\hat{y}\sin\beta + \hat{z}\cos\beta \tag{3.3.c}$$

$$\hat{b}_4 = -\frac{1}{2}\hat{x}\sin\beta - \frac{\sqrt{3}}{2}\hat{y}\sin\beta + \hat{z}\cos\beta\,, \tag{3.3.d}$$

where $\beta$ = 109° is the bond angle. After some algebra we find the analytic expressions for the bulk SHG fields for the four polarization combinations *pp*, *ps*, *sp*, and *ss*:

$$\begin{aligned} E_{pp} = -\frac{iqck^3 Z_0 V_0}{64\pi V}\frac{e^{ikr}}{r}\alpha^2 (&6\cos\beta\cdot\sin^3\beta\cdot\cos^2\theta\cdot\cos 3\phi \\ &+\cos\theta(32\sin^3\theta - 24\sin^2\beta\sin^3\theta \\ &+3\sin^4\beta(\sin\theta + 3\sin^3\theta)) - 6\sin^2\beta\cdot\sin 2\theta) \end{aligned} \tag{3.4.a}$$

$$\begin{aligned} E_{ps} = \frac{3iqck^3 Z_0 V_0}{128\pi V}\frac{e^{ikr}}{r}\alpha^2\cos\beta\cdot \\ (-5\cos\theta + \cos 3\theta)\sin^3\beta\cdot\sin 3\phi \end{aligned} \tag{3.4.b}$$

$$\begin{aligned} E_{sp} = \frac{3iqck^3 Z_0 V_0}{128\pi V}\frac{e^{ikr}}{r}\alpha^2\sin^2\beta\,[&2\sin 2\beta\cos 2\theta\cos 3\phi \\ &-(3+5\cos 2\beta)\cos\theta\sin\theta)] \end{aligned} \tag{3.4.c}$$

$$E_{ss} = \frac{3icqk^3 Z_0 V_0}{32\pi V}\frac{e^{ikr}}{r}\alpha^2\cos\beta\cos\theta\sin^3\beta\sin 3\phi \tag{3.4.d}$$

For Si (100), the situation is more complicated. If the bonds of the (001)Si-$SiO_2$ interface are oriented in the same way as those of the bulk, the bonding configuration is that shown schematically in Fig. 3.2. The bond vectors are specifically

$$\begin{aligned} \hat{b}_{1,2} &= \langle \pm\sin\beta/2 \quad 0 \quad \cos\beta/2 \rangle \\ \hat{b}_{3,4} &= \langle 0 \quad \pm\sin\beta/2 \quad -\cos\beta/2 \rangle \end{aligned}\,. \tag{3.5.a}$$

However, on a macroscopic scale the (001)Si surface consists of two types of domains differing by a 90° rotation of the bonds. This is a result of the fact that the two sublattices of the diamond structure are chemically identical, so in contrast to e.g. the III-V materials any interface generated by purely statistical means will contain nominally equal areas of both, with each domain separated from the next by an atomic-height step. Adding a second set of vectors rotated azimuthally by 90° from the original group yields a set of 8 bonds. If the strengths of the four upper and four lower bonds were equal, then the sum would vanish identically and no harmonic signal would result. However, if the longitudinal hyperpolarizabilities of the upper and lower bonds are unequal, then we obtain a finite result with the original hyperpolarizabilities replaced by their difference.

On a macroscopic scale we therefore consider the four basic bond vectors prior to rotation to be

$$\begin{aligned} \hat{b}_{1,2} &= \langle \pm \sin\beta/2 \quad 0 \quad \cos\beta/2 \rangle \\ \hat{b}_{3,4} &= \langle 0 \quad \pm \sin\beta/2 \quad \cos\beta/2 \rangle \end{aligned}, \tag{3.5.b}$$

where all *z*-components are now taken to be positive. For singular samples the quadrupole SHG contributions are

$$\begin{aligned} E_{pp} = \frac{icqk^3 Z_0 V_0}{64\pi V}\frac{e^{ikr}}{r}\alpha^2 \cos\theta \sin\theta [(6 + \sin^2\beta - \\ 22\sin^2\theta + 3\sin^2\beta\sin^2\theta - 6\cos\beta - 10\cos\beta\sin^2\theta) \\ + (\frac{3}{2} + \frac{1}{2}\cos 2\beta - 2\cos\beta)\cos^2\theta\cos 4\phi] \end{aligned} \tag{3.6.a}$$

$$E_{ps} = \frac{icqk^3 Z_0 V_0}{16\pi V}\frac{e^{ikr}}{r}\alpha^2 Cos^2\theta \cdot Sin\theta \cdot Sin^4\frac{\beta}{2} Sin4\phi \tag{3.6.b}$$

$$E_{sp} = \frac{icqk^3 Z_0 V_0}{64\pi V}\frac{e^{ikr}}{r}\alpha^2[-6-10\cos\beta + 2(\cos\beta - 1)\cos 4\phi]\sin 2\theta \sin^2\frac{\beta}{2} \tag{3.6.c}$$

$$E_{ss} = \frac{icqk^3 Z_0 V_0}{16\pi V}\frac{e^{ikr}}{r}\alpha^2 \sin\theta \sin^4\frac{\beta}{2}\sin 4\phi \tag{3.6.d}$$

### 3.2.2 Bond-sum evaluation: spatial dispersion contributions

Spatial dispersion is an effect due to the spatial variation of the incident field, which can also induce second-order displacements and thus generate SHG. The spatial variation of the incident field at the interface can be ignored since its SHG contribution is dominated by first-order effects. As a result, the main contribution from spatial dispersion comes from the bulk. In the following, we will begin with Eq. (2.19) instead of Eq. (2.22), since the results are the same in either case. By expanding the field to first order; we can write the force equation. (2.10) to second order as

$$\begin{aligned}\vec{F} &= m\frac{d^2\vec{r}_j}{dt^2} \\ &= q_j\vec{E}\cdot\hat{b}_j(1-i\vec{k}\cdot\vec{r}_j)e^{-i\omega t} - \kappa_1(\vec{r}_j-\vec{r}_0) - \kappa_2(\vec{r}_j-\vec{r}_0)^2 - \gamma\frac{d\vec{r}_j}{dt},\end{aligned} \tag{3.7}$$

where the $i\vec{k}$ in Eq. (3.7) is from $\nabla\vec{E}$, since $\vec{E}$ is proportional to $e^{i\vec{k}\cdot\vec{r}}$, where $\vec{k}$ is the wave vector of the incident wave. In Eq. (3.7) $\vec{r}$ is the bond displacement, which is equivalent to $\Delta\vec{r}_j$ in Eq. (2.19). The vector $\vec{r}_0$ can be taken to be $\hat{b}_j$, so the displacement of the $j^{\text{th}}$ bond can be written

$$\vec{r}_j = \vec{b}_j + (\Delta r_{j1}e^{-i\omega t} + \Delta r_{j2}e^{-2i\omega t})\hat{b}_j + \cdots \tag{3.8}$$

Solving these equations and ignoring the terms of $(\vec{k}\cdot\vec{b})^2$ we obtain the part of SHG due to spatial dispersion:

$$\Delta\vec{r}_{j2}^{\,Dis} = \frac{-(\vec{k}\cdot\vec{b}_j)(\vec{E}\cdot\hat{b}_j)^2\hat{b}_j}{-4m\omega^2+k_1-i\lambda 2\omega}\cdot\frac{q_j^2}{(-m\omega^2+k_1-i\gamma\omega)} + \frac{-2i\kappa_2(\vec{k}\cdot\vec{b}_j)(\vec{E}\cdot\hat{b}_j)^2\hat{b}_j}{-4m\omega^2+k_1-i\lambda 2\omega}\cdot\frac{q_j^2}{(-m\omega^2+k_1-i\gamma\omega)^2} \tag{3.9}$$

From Eq. (3.9) we can see that the above spatial-displacement expression includes the interface as well as the bulk contribution. The interface contribution is that involving $\kappa_2$, which for centrosymmetric materials is zero in the bulk. In the following calculations we ignore the $\kappa_2$ term.

Having $\Delta\vec{r}_j$ for spatial dispersion, we can calculate the resulting field contribution as done with Eqs. (3.4) and (3.6). For Si (111) these are

$$E_{ss} \propto \cos\theta\cos\beta\sin^3\beta\sin 3\phi \tag{3.10.a}$$

$$E_{sp} \propto \sin^2\beta\sin 3\theta(8\sin 2\beta\cos 3\phi - 10\sin 2\theta - 6\sin 2\theta\cos 2\beta) \tag{3.10.b}$$

$$E_{ps} \propto \cos\beta(\cos\theta+3\cos 3\theta)\sin^3\beta\sin 3\phi \tag{3.10.c}$$

$$E_{pp} \propto \cos\theta[3\cos\beta(\cos\theta+\cos 3\theta)\sin^3\beta\cos 3\phi - 3\sin^2 2\beta\sin\theta + 9\cos^2\theta\cos\theta\sin^4\beta + 8\sin^3\beta + 24\cos^4\beta\sin^3\theta] \tag{3.10.d}$$

We write these with the proportionality symbol because we are ignoring the prefactor. For Si (100), we have similarly

$$E_{ss} \propto \sin\theta \sin^4 \frac{\beta}{2} \sin^3 \beta \sin 4\phi \tag{3.11.a}$$

$$E_{sp} \propto \sin^2 \frac{\beta}{2} \sin 2\theta (5 + 3\cos\beta + \cos\beta \cos 4\phi - \cos 4\phi) \tag{3.11.b}$$

$$E_{ps} \propto \cos^2 \theta \sin\theta \sin^4 \frac{\beta}{2} \sin 4\phi \tag{3.11.c}$$

$$\begin{aligned} E_{pp} \propto \sin 2\theta [2\cos^2 \theta \sin^2 \frac{\beta}{2} (1 + 7\cos\beta + \cos\beta \cos 4\phi \\ - \cos 4\phi) - 8\cos^2 \frac{\beta}{2} \sin^2 \theta (1 + 3\cos\beta)\} \end{aligned} \tag{3.11.d}$$

The final expression for the far field is

$$E_{g-h}(2\omega) = E_{g-h}^{Dip}(2\omega) + E_{g-h}^{Quad}(2\omega) + E_{g-h}^{Dis}(2\omega) \tag{3.12}$$

where g and h represent p or s. The dipole contributions can be found in [17]. The intensity is the absolute square of the total field.

### 3.2.3 Signals as a function of depth: field-penetration effects, phase considerations, and relative bulk and surface contributions

Since fields of bulk origin can emerge from an appreciable depth within the material, the complete picture must take into account the fact that the phases of the driving and radiation fields at different lattice planes in the bulk are different. In addition, the contribution from the surface is expected to be different from that of the bulk. However, all signals are phase-correlated since they arise from a common driving field, so in calculating the observed intensity cross terms are expected to be important.

Because interface and bulk contributions involve different orders of nonlinear effects for SHG, we cannot simply compare thicknesses of the contributing bulk and surface regions as is the case of THG discussed in the next chapter, where the two types of hyperpolarizabilities appear to be comparable.

Since the interface is essentially only two monolayers thick, its contribution can be evaluated directly without considering phase delays. For the bulk, we sum over the individual monolayers with phase delays taken into account. Since the layer spacing is much less than the wavelength of light we approximate the sum over layers with an integral,

$$\sum_l e^{2i(\vec{k}_o - \vec{k})\bullet\vec{r}_o} \cong \frac{1}{\Lambda}\int dz\, e^{-2i*2k_z z} = \frac{i}{4\Lambda k_{oz}}, \tag{3.13}$$

where $\Lambda$ is the interlayer spacing. This expression is derived assuming that the wave vectors of the incident and radiating waves are normal to the surface and point in opposite directions. The first assumption is valid to a high degree of accuracy for semiconductors, where refractive indices are of the order of 3 to 4. Given this, the second assumption is clearly correct for the backscattering configuration. The calculation does not take absorption into account, but this can be added if necessary.

We also make the approximation

$$\alpha_1 = \frac{q}{\kappa_1 - m\omega^2} \approx \frac{q}{\kappa_1} \tag{3.14}$$

where $\alpha_1$ is related to the linear susceptibility. We also ignore the $m\omega^2$ contribution to $\kappa_1 - m\omega^2$ and $\kappa_1 - 4m\omega^2$, which is reasonable since for our application the frequency of

interest is relatively far from any resonance. With phase considered in this way Eq. (2.22) takes the form

$$\begin{aligned}\vec{E}_{ff} &= \frac{qk^2}{r}(\tilde{I} - \hat{k}\hat{k}) \bullet \sum \hat{b}_j \{\alpha_1 (\hat{b}_j \bullet \vec{E}_o) e^{ikr - i\omega t} e^{i(\vec{k}_o - \vec{k}) \bullet \vec{r}_o} \\ &+ \alpha_1^2 (\hat{b}_j \bullet \vec{E}_o)^2 [-i(\hat{b}_j \bullet \vec{k}) + \\ &2i(\hat{b}_j \bullet \vec{k}_o) - \frac{2\kappa_2}{\kappa_1}] e^{2ikr - 2i\omega t} e^{2i(\vec{k}_o - \vec{k}) \bullet \vec{r}_o} \}.\end{aligned} \tag{3.15}$$

Performing a lateral integration over the surface leads to total linear and SHG contributions of

$$\begin{aligned}E_{ff}^{tot} &= \frac{\pi q}{V}(\tilde{I} - \hat{k}\hat{k}) \bullet \sum_j \hat{b}_j \{\alpha_1 (\hat{b}_j \bullet \vec{E}_o) e^{ikz - i\omega t} + \\ &ik\alpha_1^2 (\hat{b}_j \bullet \vec{E}_0)^2 (\frac{3}{4}(\hat{k} \bullet \hat{b}_j) - 2\Lambda \frac{\kappa_2}{\kappa_1})) e^{i2kz - i2\omega t}\},\end{aligned} \tag{3.16}$$

where V = ΛA is the volume of the unit cell. For tetrahedral bonding the vector projections and the sum over j reduce to 4/3 in the linear case, whence at normal incidence the linear term reduces approximately to

$$\frac{E_{ff}}{E_o} \approx \frac{4\pi q \alpha_1}{3V} = \frac{1-n}{1+n}. \tag{3.17}$$

We can thus relate the SHG intensity originating from the bulk to the intensity $I_o$ of the driving laser as

$$I_{SHG} \approx \frac{\pi \gamma^2 V^2 I_o^2}{128 \lambda^2 c q^2} \left(\frac{1-n}{1+n}\right)^4, \tag{3.18}$$

where V is the volume of the unit cell, and

$$\vec{\gamma} = \sum_j \{[(I - \hat{k}\hat{k}) \bullet \hat{b}_j] (\hat{k} \bullet \hat{b}_j) (\hat{b}_j \bullet \hat{E}_j)^2 \qquad (3.19)$$

is the vector summarizing geometric factors and has a magnitude of order 0.2.

We can now estimate the relative bulk and surface contributions for centrosymmetric materials. Using values appropriate to our SHG configuration (1 W average incident power, $\lambda$ = 800 nm, a duty cycle of $10^{-4}$, and an illuminated area of characteristic dimension 40 μm), we estimate that $N_{SHG} \sim 10^4\gamma^2/\text{s} \sim 0.04 \times 10^4/\text{s}$, where $N_{SHG}$ is the number of bulk SHG photons generated per second. For comparison we typically observe total SHG generation rates of the order of $2.5 \times 10^4$/s, which indicates that the bulk contribution, treated as if the intensities were additive, is very small, certainly much less than the observed count rates.

A second way to estimate relative bulk and surface contributions is also possible. We will consider the (111)Si surface as an example. From Eq. (3.4.a) we estimate that $V_0 = \int SEdz = V_{01}E_p$ , where $V_{01}$ is the focus area times the penetration depth and $E_p$ is the magnitude of the p-polarized incident field.. The other parameters can be obtained from the literature. Taking the value [19] $\chi_1 = 1.06\times10^{-10}$ for Si, assuming an incident field of the order of $1\times10^8$ N/C, and using $\lambda$ = 800 nm, a unit cell volume = $4\times10^{-23}$ cm$^3$, a sample-collector separation of 0.5 m, a $2\omega$ absorption coefficient of $9.0\times10^4$ cm$^{-1}$, and a volume exposed to the incident radiation of $1.4\times10^{-10}$ cm$^3$, we find the emitted SHG energy to be about $0.24\times10^{-14}$ J/s. This can be compared to values of about $1\times10^{-14}$ J/s that we measure experimentally. Hence from this perspective the bulk contribution is about one-quarter or less of the observed intensity, which leads to the same result as

above. We will include the quadrupole and spatial-dispersion contributions to SHG when we simulate data later.

### 3.2.4 Determination of relative bulk/surface contributions from anisotropy data.

We now consider the determination of relative bulk/surface contributions from data. The results of Lüpke *et al*. [16] include all four polarization combinations *pp*, *ps*, *sp*, and *ss*, and are shown in Fig. 3.3. These data were obtained at a wavelength of 765 nm on a Si sample cut 5° off (111) toward the [11-2] direction. The angles of incidence and observation in air were both 45°. Lüpke *et al*. used a phenomenological method to analyze their data, where the dipole moment is connected to the far-field SHG or THG through third- or fourth-rank susceptibility tensors, respectively. This macroscopic way of connecting the total dipole density to the incident field is to formulate the macroscopic second order (for bulk) and third order (for surface) susceptibility tensors in the crystal frame, then rotate these tensors to the laboratory frame, and then obtain the dipole density. The generated SHG far field radiation is then calculated in the dipole approximation.

To obtain the relative bulk contribution we perform a least-square analysis, fitting all four data sets simultaneously with the SBHM model predictions. Since Lüpke *et al*. normalized the individual polarization combinations to the $6^{th}$ harmonic of the Fourier decompositions [16], the actual magnitudes are unknown. We take this into account by using individual scaling factors for the *ps*, *sp*, and *ss* data. However, we use a common scaling factor between the interface and bulk contributions for all four data sets, since this is independent of measurement conditions. The fixed parameters are the vicinal angle of

5°, the angles of incidence of 29.1° and 11° for the interface and bulk, respectively, and the bond angle of 109.4° for both interface and bulk. In particular we use the specified vicinal angle of 5° instead of the value of 1.12° previously used by Powell *et. al.* [17]. The angles of incidence are obtained from Snell's Law, taking into account the refractive indices of $SiO_2$ and Si. The phase reference is provided by one of the two back interface bonds, which we take to be zero.

The results are shown in Fig. 3.3. The residuals are 0.263, 0.116, and 0.087 for bulk-only, interface-only, and bulk and interface combined. In the last case the individual bulk and interface contributions for the *pp* combination are shown in Fig. 3.4. The residuals indicate that the overall fit improves substantially through the sequence. The surprising result is that the bulk contribution, for which the lineshapes are invariant and the only parameters that can be varied are the scaling factors, provides such a good representation of the data. With additional, lineshape-modifying parameters available for the interface-only case, improvement is not surprising. Here, the hyperpolarizabilities obtained are 1.28 + i0.28, 3.11 + i1.66, 2.23 – i0.01, and 2.23 + i0, where the last is used as a phase reference. With both bulk and interface included the fit improves further, with the bulk now contributing about 1/4 of the overall signal, as seen in Fig. 3.3, and the hyperpolarizabilities becoming 1.19 + i0.81, 1.45 + i1.39, 1.42 – i0.00, and 1.42 – i0. Thus the bulk contribution causes the interface parameters to adjust to improve the overall fit, mostly via a change of the hyperpolarizability of the second, "step" bond. Since all combinations provide an acceptable representation of the observed anisotropies, the (111) data are somewhat inconclusive.

A more definitive example is given in Fig. 3.5. These data were obtained on a (001)Si surface cut 9° off (001) toward [111] [18]. As shown previously, the angle of incidence appropriate to this interface contribution is 12°. The bulk contributions, shown in Fig. 3.6, are very different from the data, in particular contributing virtually nothing to the major intensity peak near 0°. Hence, and in contrast to the vicinal (111) sample, a bulk-only representation cannot succeed and was not attempted. The residuals for interface-only and combined interface and bulk contributions are 29.9 and 18.8, respectively. Thus the fit is improved with the bulk contribution included, mainly through its effect on *pp*. For the interface-only case the hyperpolarizabilities are 87.9 – i0.9, 188.5 – i47.9, 122.8 + i0, and 120.9 + i0, with the last being used as the phase reference. With the bulk included the values become 67.2 – i2.4, 149.5 – i34.8, 90.0 + i6.5, and 84.9 + i0, so all hyperpolarizabilities change by similar amounts. However, the good fit obtained in the interface-only case and the substantial differences between the bulk lineshapes and data suggest that the observed improvement with bulk included may only be a secondary effect, with the bulk acting to artificially distort the interface contribution to give the better overall fit. In any case, the improved fit is a direct consequence of the coherent superposition of the interface and bulk signals, so the coherent superposition cannot be ignored.

One of the difficulties in analyzing the Lüpke *et al*.[16] data follows from the absence of information about the 7$\phi$ Fourier coefficients. Our SBHM calculations given in Table 3.1 show that the 7$\phi$ coefficients appears only if the bulk contribution is present and the surface orientation is neither (001) nor (111). Thus both a bulk contribution and a vicinal sample are necessary to generate a 7$\phi$ term. For small vicinal angles, which

describe the cases considered here, we can use the magnitude of 7ϕ coefficients to estimate the bulk contribution. For the (001)Si *pp* data these coefficients are less than 10% of the 6ϕ coefficients, providing further evidence that the bulk contribution is small.

In summary, we have estimated the relative bulk and interface contributions to SHG for oxidized Si by obtaining an analytic expression for the first-forbidden bulk contributions, evaluating it directly using reasonable experimental parameters, then performing a least-squares analysis of SHG anisotropy data for vicinal (111) and (001)Si samples. We conclude that the major fraction of observed nonlinear-optical anisotropies arises from bond geometry and therefore, as with linear optics, very little information is available from single-wavelength data. Nevertheless, even in the absence of spectral data the SBHM allows us to clarify previous assumptions about the relative importance of bulk and interface contributions to SHG in centrosymmetric materials, identify the importance of the interaction between bulk and surface contributions, and recognize the significance of the 7ϕ component in determining bulk contributions for vicinal samples.

## *3.3 Conclusions*

In Ch. III we apply the theory developed in Ch. II to dipole-forbidden SHG arising in the bulk of centrosymmetric materials. Having analytic representations of the bulk contributions, we are able to clarify the relative importance of bulk and surface contributions for SHG. The bulk alone is found to contribute little to SHG, although in the THG case we will find that the coherent interaction between bulk and surface contributions at the field level is significant. Because the bulk contributions to SHG in Si

are relatively minor, the SBHM continues to represent the azimuthal dependences of SHG data for Si very well.

The obvious conclusion remains that the geometry of the crystal is the most important factor for determining SHG, at least for Si. Discrepancies may indicate that factors other than geometric symmetry are important. We conclude that not much information can be obtained from data obtained at single wavelengths. In the future, when wide-range wavelength-tunable lasers may become available, much more information is should be obtainable from for example resonant energies, critical point parameters, etc. Whether the SBHM represents a sufficiently powerful analytic tool to interpret these data remains as a challenge, but we expect it to meet this challenge.

## *References:*


[1] P. A. Franken, A. E. Hill, C. W. Peters, and G. Weinreich, Phys. Rev. Lett. **7**, 118 (1961).

[2] Y. R. Shen, *The Principles of nonlinear optics*, Wiley, New York, 1984.

[3] Y. R. Shen, Ann. Rev. Mater. Sci. **16**, 69 (1989).

[4] J. F. McGilp, J. Phys. (London) Condens. Matter. **1**, 85 (1989).

[5] T. F. Heinz, G. A. Reider, Trends Anal. Chem. **8**, 235 (1989).

[6] T. V. Murzina, R. V. Kapra, and O. A. Aktsipetrov, Appl. Phys. Lett., Vol. **83**, 4749 (2003).

[7] M. Fiebig, D. Fröhlich, Th. Lottermoser, and M. Maat, Phys. Rev. **B66**, 144102. (2002).

[8] V. Fomenko and E. Borguet, Phys. Rev. **B68**, 081301(R) (2003).

[9] J. S. Salafsky and K. B. Eisenthal, J. Phys. Chem. **B104**, 7752 (2000).

[10] M. Reid, I. V. Cravetchi, and R. Fedosejevs, Phys. Rev. **B72**, 035201 (2005).

[11] O. A. Aktsipetrov, A. A. Fedyanin, V. N. Golovkina, and T. V. Murzina, Optics Letters, **19**, 1450 (1994).

[12] H. Ito, F. Minami, K. Yoshida, and K. Inoue, Journal of Luminescence, 66-7, **493** (1995).

[13] C. Simonneau, J. P. Debray, J. C. Harmand, P. Vidakovic, D. J. Lovering, and J. A. Levenson, Optics Letter, **22**, 1775 (1997).

[14] S. Chandola and J. F. McGilp, Physica Status Solid, **A184**, 111 (2001).

[15] Y. D. Glinka, T.V. Shahbazyan, I. E. Perakis, N. H. Tolk, X. Liu, Y. Sasaki and J. K. Furdyna, Surface and Interface Analysis, **35**, 146 (2003).

[16] G. Lüpke, D. J. Bottomley, and H. M. van Driel, J. Opt. Soc. Am. **B11**, 33 (1994).

[17] G. D. Powell, J. –F. Wang, and D. E. Aspnes, Phys. Rev. **B65**, 205320 (2002).

[18] J. –F. T. Wang, G. D. Powell, R. S. Johnson, G. Lucovsky, and D.E. Aspnes, J. Vac. Sci. Technol. **B20**, 1699 (2002).

[19] D. E. Aspnes and A. A Studna , Phys. Rev. B27, 985 (1983).

## cos7ϕ coefficients of *pp* anisotropies of Si surfaces

| | Si(100) | Si(111) |
|---|---|---|
| Non-tilt without bulk | 0 | 0 |
| Non-tilt with bulk | 0 | 0 |
| Tilt without bulk | 0 | 0 |
| Tilt with bulk | Non-zero | Non-zero |

**Table 3.1 cos7ϕ coefficient of *pp* signal of silicon surface**

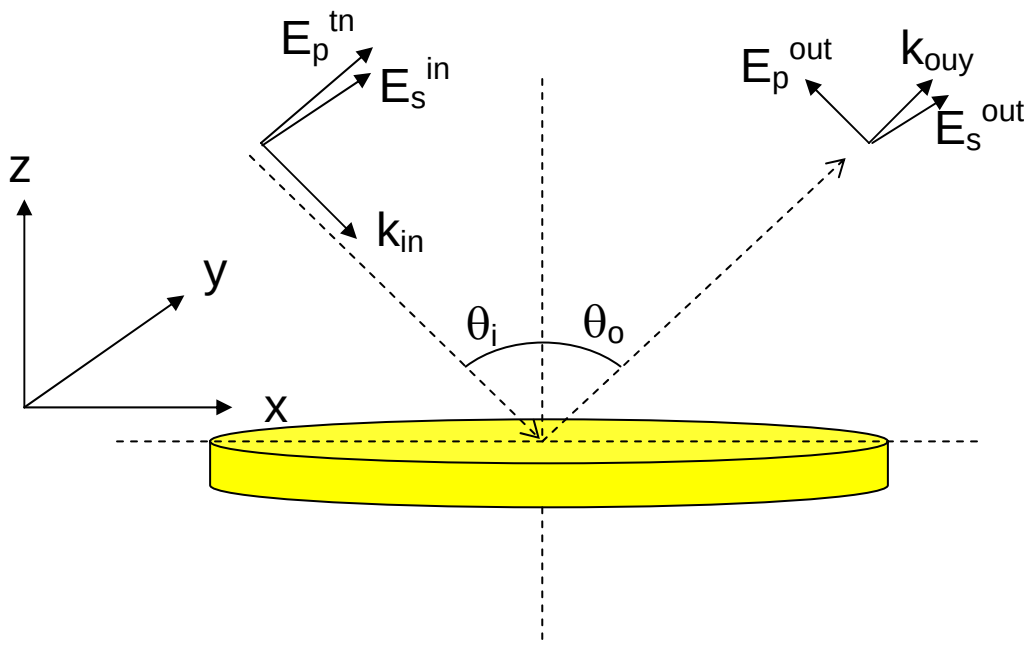



**Figure 3.1 Experiment diagram for reflected-harmonic-generation measurements.**

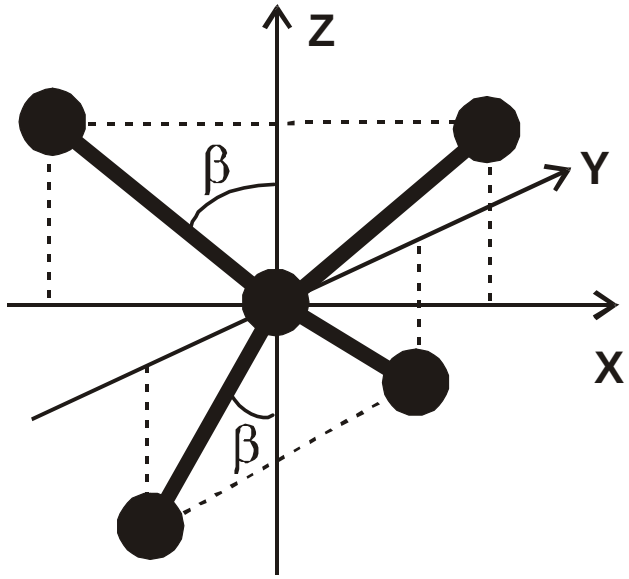



**Figure 3.2 Bond vector diagram**

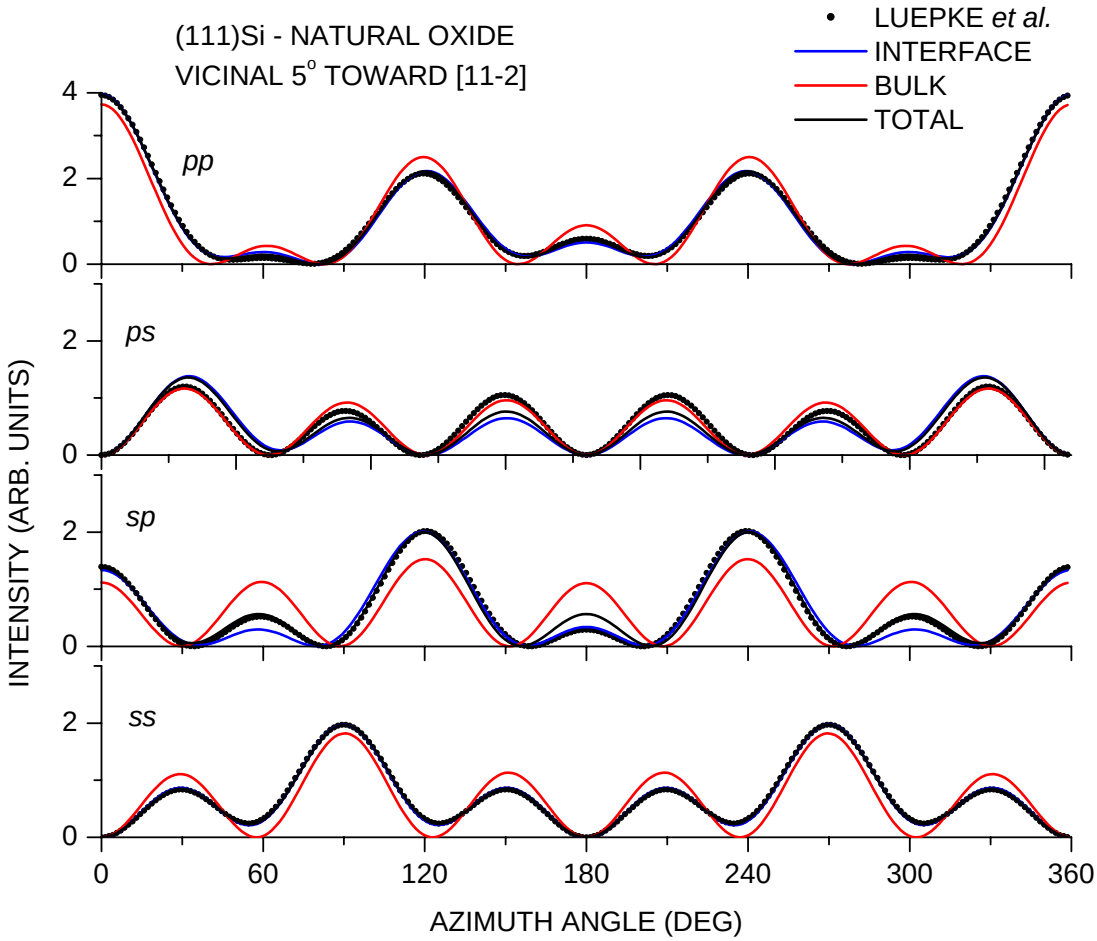



**Figure 3.3 Azimuth dependence of SHG for vicinal Si 5° off (111) toward [11-2].**

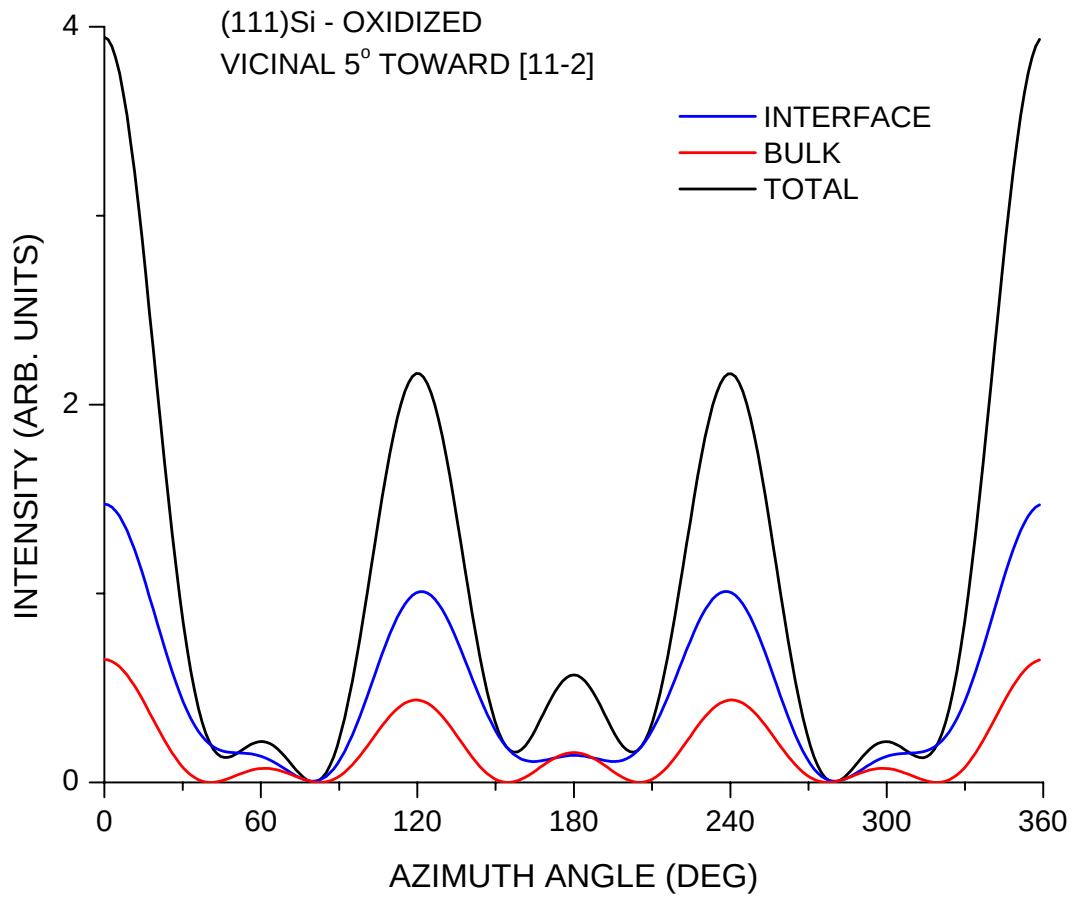



**Figure 3.4 Different contributions to the *pp* data of Fig. 3.2.**

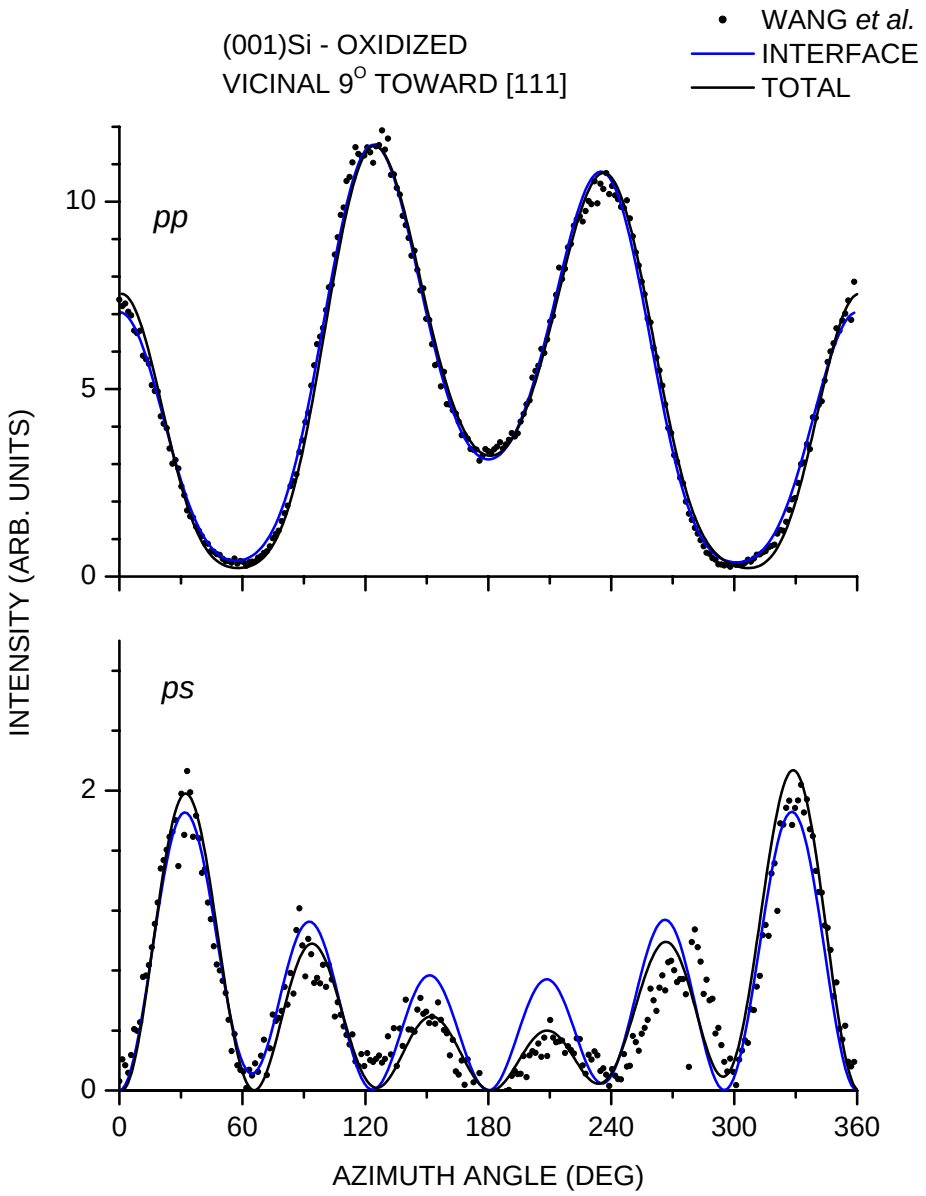



**Figure 3.5 Azimuthal dependence of SHG for vicinal Si 9° off (001) toward [111].**

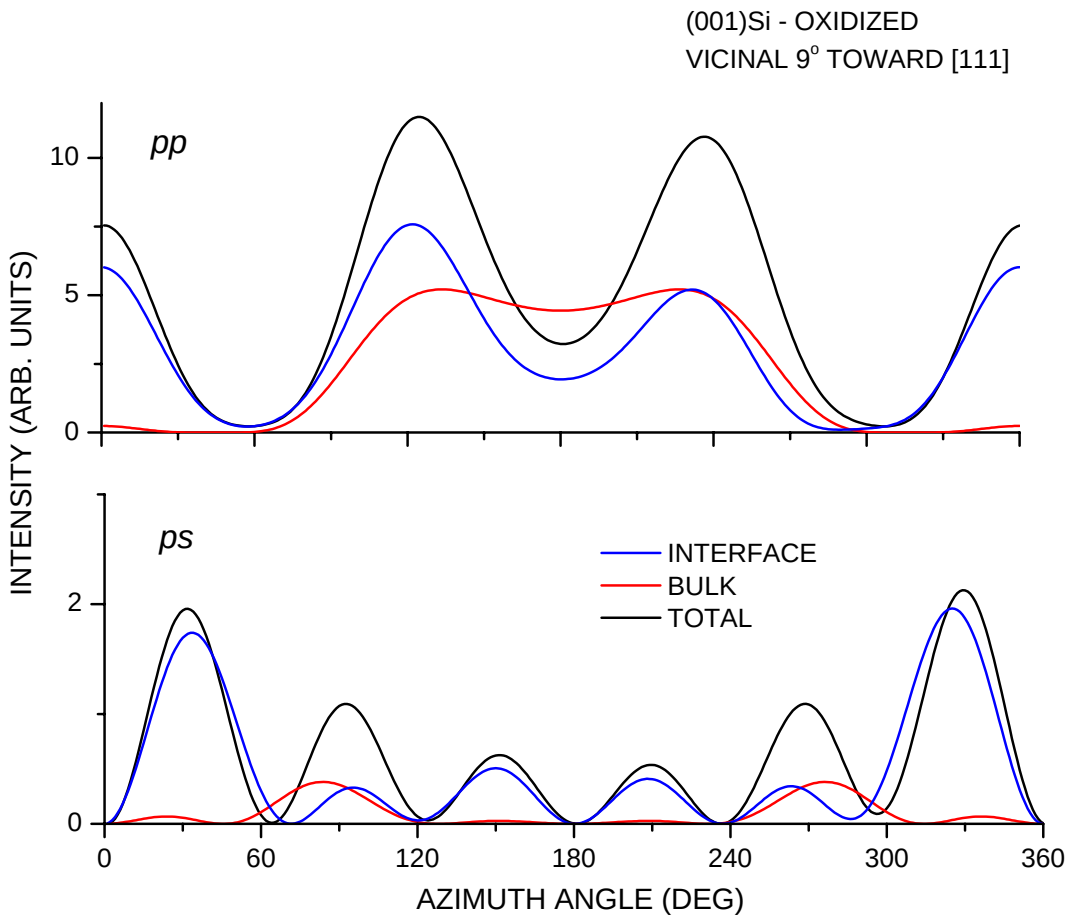



**Figure 3.6 Different contributions to the data of Fig. 3.4.**

# Chapter IV Bulk Third Harmonic Generation from Crystalline Si

## *4.1 Introduction*

In Ch. II we developed a simplified bond-hyperpolarizability model (SBHM) [1, 2], and applied it to dipole-forbidden SHG [3] in Ch. III. In both cases the SBHM provided an excellent representation of the data. The question naturally arises; does the model provide the same advantages for THG? This is a particularly interesting case for at least two reasons. First, (001)Si interfaces are locally twofold-rotationally symmetric, but because the two Si sublattices are oriented 90° apart and are chemically identical, macroscopic interface regions will have statistically equal areas of the two types of domains and hence exhibit macroscopic fourfold rotational symmetry. Therefore, THG is the lowest nonvanishing $n^{th}$-harmonic NLO signal that can be obtained on the Si(001) interfaces on which integrated-circuits technology is based.

Second, the bulk contribution to THG is dipole-allowed, even for crystals with inversion symmetry, and hence, in contrast to the SHG case, is expected to dominate THG signals. We estimate below that the interface contribution for Si is probably no more than 5% of the total signal, but this means that, as with linear optics and noted above, interface contributions can be extracted only with the help of additional data, for example the wavelength dependences of the associated hyperpolarizabilities. If the SBHM is to provide a useful means of obtaining these hyperpolarizabilities, the obvious first requirement is that it accurately describes THG from the bulk. Application to a dominantly bulk response also represents an important test of the model, because the

directions of the bulk bonds are unambiguous, as opposed to interfaces where roughness or chemical-bonding effects can result in bond directions different from those in the bulk.

Here, we show that the SBHM does provide an accurate description of THG data for Si. We also provide further clarification of the model by relating its parameters to the two nonvanishing components of the macroscopic fourth-rank nonlinear-susceptibility tensor describing bulk THG in cubic materials. By comparing our calculations to previous experimental results [4, 5], we find that the SBHM accurately describes THG anisotropies of singular (111), (110), and (001)Si samples, and provides a nearly complete representation of THG for vicinal samples. In addition, treating the internal propagation direction as an adjustable parameter yields the value expected from Snell's Law.

However, consistent with the fact that the fourth-rank THG tensor of silicon has two independent bulk components, an accurate description of THG for the *pp* and *ss* polarization combinations can be realized only by extending the SBHM to include the transverse hyperpolarizability as well as the longitudinal component used in previous work. This is not surprising because the symmetry argument that allowed us to ignore the transverse component for SHG and FHG does not apply to THG. Some differences between model calculations and the THG data remain, which need to be examined in greater detail. Since the SBHM basically summarizes geometric contributions, these differences may prove useful in gaining an improved understanding of THG. We also make specific predictions for the anisotropies of polarization combinations for which data have not yet been reported, for example the *sp* and *ss* combinations for (111)Si.

## *4.2 Derivation of expressions for THG*

We start from Eqs. (2.14.c) and (2.15.c). However, the symmetry argument that allows us to ignore the transverse contribution in SHG and FHG does not apply to any of the odd susceptibilities, including the linear-optical response as well as THG. Therefore, we also consider the transverse contribution, which has a form similar to that given in Eqs. (2.14.c) and (2.15.c). As a result we will change the notation for the bond vector in Eqs. (2.14.c) and (2.15.3) to the unit vector $\hat{u}_j$, where $\hat{u}_j$ is either $\hat{b}_j$ or $\hat{b}_{jt}$, where $\hat{b}_{jt}$ is the unit vector perpendicular to $\hat{b}_j$ lying in the $\hat{b}_j - \hat{E}$ plane. Specifically, $\hat{b}_{jt}$ is given by

$$\hat{b}_{jt} = [\hat{E} - \hat{b}_j(\hat{b}_j \bullet \hat{E})] / |1 - (\hat{b}_j \bullet \hat{E})^2|^{1/2}. \tag{4.1}$$

For the longitudinal case we write

$$\vec{p}_{3jl} = \alpha_{3lj}\, \hat{b_j}\, (\hat{b}_j \bullet \vec{E})^3 , \tag{4.2}$$

where $\alpha_{3lj}$ is the longitudinal third-order hyperpolarizability of the $j^{\text{th}}$ bond. As usual, the (macroscopic) longitudinal polarization density $\vec{P}_{3l}$ is calculated by averaging the microscopic dipoles over a volume V:

$$\vec{P}_{3l} = \frac{1}{V}\sum_j \vec{p}_{3lj} = \frac{1}{V}\sum_j (\alpha_{3lj}\hat{b}_j\hat{b}_j\hat{b}_j\hat{b}_j) \bullet\bullet\bullet \vec{E}\vec{E}\vec{E}, \tag{4.3a}$$

$$= \frac{\alpha_{3l}}{V}\sum_j (\hat{b}_j\hat{b}_j\hat{b}_j\hat{b}_j) \bullet\bullet\bullet \vec{E}\vec{E}\vec{E}, \tag{4.3b}$$

where in the bulk $\alpha_{3l}$ is the same for all $j$. The transverse contribution is treated identically with the substitution of $\hat{b}_{jt}$ for $\hat{b}_j$ and the transverse third-order hyperpolarizability $\alpha_{3t}$ for $\alpha_{3l}$.

## *4.3 General properties for tetrahedrally bonded semiconductors; connection to fourth-rank susceptibility tensor components*

Given these polarizations, the far-field radiation may be calculated from previous expressions taking into account the phase-retardation effects discussed in Ch. III. However, for the tetrahedrally bonded semiconductors some general simplifications are possible. We discuss these first, since they allow analytic results to be obtained for high-symmetry crystallographic orientations and also allow the two microscopic quantities used above, $\alpha_{3l}$ and $\alpha_{3t}$, to be related to $\chi_{1111}$ and $\chi_{1212}$, the two nonvanishing components of the fourth-rank susceptibility tensor for materials of cubic symmetry.

For the tetrahedrally bonded semiconductors the bond vectors relative to the crystallographic axes can be written

$$\hat{b}_1 = \frac{1}{\sqrt{3}}\hat{x} + \frac{1}{\sqrt{3}}\hat{y} + \frac{1}{\sqrt{3}}\hat{z}; \tag{4.4a}$$

$$\hat{b}_2 = -\frac{1}{\sqrt{3}}\hat{x} - \frac{1}{\sqrt{3}}\hat{y} + \frac{1}{\sqrt{3}}\hat{z}; \tag{4.4b}$$

$$\hat{b}_3 = -\frac{1}{\sqrt{3}}\hat{x} + \frac{1}{\sqrt{3}}\hat{y} - \frac{1}{\sqrt{3}}\hat{z}; \tag{4.4c}$$

$$\hat{b}_4 = \frac{1}{\sqrt{3}}\hat{x} - \frac{1}{\sqrt{3}}\hat{y} - \frac{1}{\sqrt{3}}\hat{z}; \tag{4.4d}$$

which implicitly assigns all bonds to one of the two atoms of the unit cell. In the following we sum over the four bond vectors listed above, treating the sum over unit cells and volume normalization V in the next section.

We first consider the connection between the longitudinal and transverse contributions to the overall response. Using Eq. (4.1) we can write the dyadic portion of the transverse equivalent of the sum in Eq. (4.3b) as

$$\begin{aligned}
&\sum_j (\hat{b}_{jt}\hat{b}_{jt}\hat{b}_{jt}\hat{b}_{jt} \bullet\bullet\bullet \hat{E}\hat{E}\hat{E}\hat{E}) \\
&= \sum_j \frac{[\hat{E} - \hat{b}_j(\hat{b}_j \bullet \hat{E})]^4}{[1-(\hat{b}_j \bullet \hat{E})^2]^2} \bullet\bullet\bullet \hat{E}\hat{E}\hat{E}\hat{E} \\
&= 4\hat{E} - (\sum_j \hat{b}_j\hat{b}_j) \bullet \hat{E} - \hat{E}(\sum_j \hat{b}_j\hat{b}_j) \bullet\bullet \hat{E}\hat{E} + (\sum_j \hat{b}_j\hat{b}_j\hat{b}_j\hat{b}_j) \bullet\bullet\bullet \hat{E}\hat{E}\hat{E}\hat{E} \\
&= \frac{4}{3}\hat{E} + (\sum_j \hat{b}_j\hat{b}_j\hat{b}_j\hat{b}_j) \bullet\bullet\bullet \hat{E}\hat{E}\hat{E}\hat{E}
\end{aligned} \tag{4.5a}$$

where we have used

$$\sum_j \hat{b}_j\hat{b}_j = \frac{4}{3}\underline{I}\,. \tag{4.5b}$$

Comparing Eq. (4.5a) with the dyadic part of Eq. (4.3b) we find that aside from the hyperpolarizabilities the longitudinal and transverse contributions differ only by the leading term in Eq. (4.5a). This term is isotropic and hence appears only as a constant multiplying an identity tensor, and is therefore also independent of crystallographic orientation. Thus the functional dependences of the longitudinal and transverse components on azimuth angle for any orientation of the crystal will be identical, differing only in the amount of offset, which for a given configuration is determined by the relative values $\alpha_{3l}$ and $\alpha_{3t}$. It also follows that neither the leading term nor the isotropic part of

the remaining term will contribute to the *sp* and *ps* responses, because for these configurations the associated field and polarization vectors are perpendicular to each other. Since lower-symmetry contributions such as microscopic interface roughness appear in the isotropic terms, the *ps* and *sp* combinations should be relatively insensitive to these effects

Before we go to next, we want to test one of our assumptions for SHG is that we need consider only motion in the bond direction. This conclusion is justified by assuming that the bonds are rotationally symmetric. To complete the picture it is necessary to determine whether this assumption can be justified mathematically. Here we will calculate the transverse bond contribution to SHG to assess this assumption. We will do the same calculation as above. Equation (4.1) provides an expression for a transverse bond vector. Using this expression the generated transverse electric field for SHG can be obtained, and we find

$$\begin{aligned}
&\vec{E}_t(2\omega) \propto \\
&\quad \sum_j (\hat{b}_{jt}\hat{b}_{jt}\hat{b}_{jt} \bullet\bullet \hat{E}\hat{E}) = \sum_j [1-(\hat{b}_j \bullet \hat{E})^2]^{1/2}[\hat{E} - \hat{b}_j(\hat{b}_j \bullet \hat{E})] \\
&\quad \approx 2\hat{E} + \hat{b}_j\hat{b}_j\hat{b}_j\hat{b}_j \bullet\bullet\bullet \hat{E}\hat{E}\hat{E}\hat{E}\hat{E} \\
&\quad \approx 2\hat{E}.
\end{aligned} \tag{4.6}$$

Therefore, if we ignore higher-order harmonic terms, the transverse contribution to SHG is just a dc value. And from the experimental data, we are sure that this dc value is minor.

Let's back to THG. We now consider the macroscopic polarizability. Since this can be written [6]

$$\vec{P} = 3\chi_{1212}(\vec{E} \bullet \vec{E})\vec{E} + (\chi_{1111} - 3\chi_{1212}) * (\hat{x}E_x E_x E_x + \hat{y}E_y E_y E_y + \hat{z}E_z E_z E_z) \quad (4.7)$$

it follows from the above equations that

$$\chi_{1111}^{tot} = \chi_{1111}^{l} + \chi_{1111}^{t} = \frac{4\alpha_l}{9V} + \frac{16\alpha_t}{9V}, \quad (4.8a)$$

$$\chi_{1212}^{tot} = \chi_{1122}^{tot} = \chi_{1221}^{tot} = \chi_{1212}^{l} + \chi_{1212}^{t} = \frac{4\alpha_l}{9V} + \frac{8\alpha_t}{9V} \quad (4.8b)$$

These expressions explicitly connect the two SBHM hyperpolarizabilities to the two nonvanishing components of the phenomenological fourth-rank third-order susceptibility tensor. As a result, we can also use these susceptibility tensors to reproduce all the following calculations below with no difficulty.

## *4.4 THG responses for specific geometries*

### 4.4.1 General considerations

In Sec. 3 all calculations were done in the crystallographic frame. However, in practice all vectors, including bond vectors, are generally specified relative to a laboratory frame that, from the crystal perspective, depends on surface orientation. In the laboratory frame we consider the *z* axis to be normal to the surface or interface and the incident and generated waves to lie in the *xz* plane. We assume that the external incidence angle of the driving beam is specified, but note that the angle $\theta_i$ to be used with the SBHM equations is that of the wave propagating in the medium, which is expected to be the oxide overlayer for interface responses and the bulk for bulk THG. $\theta_i$ is calculated from the external angle by Snell's Law. The internal observation angle $\theta_o$ is related to

the external observation angle in the same way. For the applications discussed below, where the external angles of incidence and observation are 45°, we have $\theta_i \approx 29°$ for $SiO_2$ and ≈ 11° for bulk Si. By performing a least-squares analysis we verify that the expected bulk value is obtained, as discussed below. For simplicity we assume $\theta_i = \theta_o$ in our numerical calculations.

The wavevectors representing the internal incident and observed fields relative to the laboratory frame are therefore $\hat{k} = -\hat{x}\sin\theta_i - \hat{z}\cos\theta_i$ and $\hat{k} = -\hat{x}\sin\theta_o + \hat{z}\cos\theta_o$, respectively. The internal incident and observed fields, again in the laboratory frame, are perpendicular to these vectors and can be separated into *s*- (TE-) and *p*- (TM-) polarized modes. The respective *s*-polarized components are $\vec{E}_{si} = E_{si}\hat{y}$ and $\vec{E}_{so} = E_{so}\hat{y}$, and the *p*-polarized components $\vec{E}_{pi} = E_{pi}\hat{p}_i = E_{pi}(-\hat{x}\cos\theta_i + \hat{z}\sin\theta_i)$ and $\vec{E}_{po} = E_{po}\hat{p}_o = E_{po}(\hat{x}\cos\theta_o + \hat{z}\sin\theta_o)$. The radiation projection operator leaves the s-polarized component unchanged, while the p-polarized component constructs the linear combination $(p_x\cos\theta_o + p_z\sin\theta_o)$.

We now consider crystal rotation. Assuming that the bond vectors $\hat{b}_j$ are defined in the laboratory frame at $\phi = 0°$, rotation is accomplished mathematically by replacing the Cartesian unit vectors in the $\phi = 0°$ descriptions as follows:

$$\hat{x} \rightarrow \hat{x}\cos\phi + \hat{y}\sin\phi \ . \tag{4.9a}$$

$$\hat{y} \rightarrow -\hat{x}\sin\phi + \hat{y}\cos\phi \tag{4.9b}$$

For vicinal samples we first define the bond vectors as if the sample were on-axis, then incorporate the tilt mathematically by applying an initial rotation by the polar angle $\gamma$ in the *xz* plane according to the replacements

$$\hat{x} \rightarrow \hat{x}\cos\gamma - \hat{z}\sin\gamma . \tag{4.10a}$$

$$\hat{z} \rightarrow \hat{x}\sin\gamma + \hat{z}\cos\gamma . \tag{4.10b}$$

The resulting vectors are then rotated azimuthally according to Eqs. (4.9).

By applying suitable rotations to the field and polarization vectors defined in the laboratory frame, expressions such as Eq. (4.9a) that are evaluated in the crystallographic frame can be used with any surface orientation. For the longitudinal case we have from Eq. (4.3b)

$$\vec{P}_l = \frac{\alpha_{3l}}{V}\sum_j M(\phi)M'\hat{b}_j\,[(M(\phi)M'\hat{b}_j)\bullet\vec{E}]^3 \tag{4.11}$$

where the $\hat{b}_j$ are same as those in Eqs. (4.4), M' is the matrix that rotates the crystal, i.e., rotates the field and polarization vectors from the crystallographic coordinate system to the laboratory frame to the position where the azimuth angle $\phi$ = 0, and M($\phi$) is the azimuth rotation matrix. After some calculations we obtain

$$\vec{P}_l = \frac{\alpha_{3l}1}{V}M(\phi)M'\sum_j \hat{b}_l\hat{b}_j\hat{b}_j\hat{b}_j \bullet\bullet\bullet\vec{E}'\vec{E}'\vec{E}' \tag{4.12}$$

where $\vec{E}' = M'^T\,M(\phi)^T\,\vec{E}$, and where $M'^T$ and $M(\phi)^T$ are the transposes of $M'$ and $M(\phi)$, respectively. These rotations allow us to calculate THG in the crystallographic coordinate system first, then project the resulting fields back to the laboratory frame.

Although the hyperpolarizabilities are in general complex, in the following we assume them to be real. Analysis of SHG anisotropy data showed that the presence of complex hyperpolarizabilities could be recognized from the inability of all local minima of the anisotropy data to reach zero. The only situation where this might occur in the data analyzed below is for the sp polarization combination for the vicinal (111)Si sample. The remaining data show no indication of phase differences. This is expected for measurements made far from resonances.

### 4.4.2 Si (111)

We begin by considering Si(111), for which the data record is most complete. In the laboratory frame the bond vectors for a singular crystal are described in Eqs. (3.5) with $\beta$ = 109.4° is the angle between any two of the bonds. The azimuth angles of the "down" bonds are chosen so that at $\phi = 0°$ bond 2 lies in the *xz* plane. Using these expressions we obtain the following analytic expressions for the longitudinal contribution to the fields in the far-field radiation zone for each of the four polarization combinations:

$$E_{ppl} = \frac{1}{8}\alpha_{3l}[-9\cos^4\theta\sin^4\beta + 8(1+3\cos^4\beta)\sin^4\beta + 12\cos\beta\cos^3\theta\sin^3\beta\sin\theta\cos 3\phi\,] \tag{4.13a}$$

$$E_{psl} = -\frac{9}{4}\alpha_{3l}\cos\beta\cos^2\theta\sin^3\beta\sin\theta\sin 3\phi \tag{4.13b}$$

$$E_{spl} = \frac{3}{4}\alpha_{3l}\cos\beta\sin^3\beta\sin\theta\sin 3\phi\ , \tag{4.13c}$$

$$E_{ssl} = \frac{9}{8}\alpha_{3l}\sin^4\beta\ , \tag{4.13d}$$

where $\alpha_{3l}$ is the longitudinal hyperpolarizability. The analytic expressions for the transverse contribution are obtained by replacing $\alpha_{3l}$ with $\alpha_{3t}$ and adding the terms $-\frac{4}{3}\alpha_{3t}\cos(\theta_i+\theta_o)$ and $\frac{4}{3}\alpha_{3t}$ to Eqs. (4.13a) and (4.13d), respectively. We note that $E_{\mathrm{ssl}}$ is independent of $\phi$, $E_{\mathrm{psl}}$ and $E_{\mathrm{spl}}$ are 180° out of phase with each other, and consistent with our above discussion only $E_{\mathrm{ppl}}$ and $E_{\mathrm{ssl}}$ have isotropic components. The sign difference between $E_{\mathrm{psl}}$ and $E_{\mathrm{spl}}$ has no effect on the intensity.

We compare the model to experiment beginning with a vicinal rather than the singular Si(111) configuration because data have been reported for all polarization combinations [14]. The calculations are done numerically rather than analytically. As discussed above the on-axis bond vectors are converted to the vicinal frame by rotating them about the $y$ axis as $\hat{b}_j' = R(\gamma)\hat{b}_{j0}$, where $R(\gamma)$ is the rotation matrix and γ = 5° toward $[11\bar{2}]$ is the vicinal angle for the Lüpke *et al* [14]. data analyzed here. The THG anisotropy is evaluated by following this with an azimuthal rotation $R(\phi)$, substituting the resulting bond vectors into Eqs. (4.3b) and (4.5a), and taking the absolute squares of the results as a function of ϕ.

The Lüpke *et al* [4]. data are shown as points in Fig. 4.1. The *ps* signal is the largest, so we determine $\alpha_{3l}$ from that, with $\theta$ and $\beta$ fixed at 11° and 109.4°, respectively. Since the *ps* combination has no isotropic contribution, the resultant lineshape should not be affected by artifacts such as interface roughness, which we showed next chapter for FHG generates an isotropic response [7]. The fit is almost perfect, indicating that the model gives an accurate representation of THG signals originating primarily from the

bulk. We emphasize that this agreement is obtained only by amplitude scaling: the lineshape itself is calculated with *no* adjustable parameters. Since the transverse and longitudinal lineshapes are identical for the *ps* combination, their individual contributions cannot be distinguished.

Next, we critically assess the capability of the model to reproduce the remaining data. These comparisons are shown in the lower three panels of Fig. 4.1. The model representation of the *sp* data, which also has no isotropic contribution, is not as good, indicating that the model could be oversimplified. However, to proceed further a first-principles theoretical calculation would be necessary, which is beyond present capabilities.

The *pp* and *ss* data provide the opportunity to assess the relative contributions of the longitudinal and transverse components, since these combinations contain dc offsets. One question is: can we account this dc offset using roughness effects? The answer is no. The reason is that because what we calculate is the bulk contribution of THG, all the surface effects including surface THG and roughness effects should be small compared to the bulk contribution. So this dc offset cannot be explained as roughness effects. Using dashed lines for the longitudinal contribution alone and solid lines for both, the second and fourth panels of Fig. 4.1 show that both contributions are needed and when both are included the *pp* and *ss* data can be fit very well with respect to both lineshapes and phases. We find the ratio of transverse and longitudinal hyperpolarizabilities to be $\frac{\alpha_{3t}}{\alpha_{3l}} = 1.2$.

The *ps* data also allow us to assess whether the expected value of 11° is the best choice of the angle of incidence. We investigate this by examining the $\theta$ dependence of

the residual $\sigma$ of the least-squares fit to the *ps* data of Fig. 4.1. The result is shown in Fig. 4.2. The minimum occurs at 9.5°, which is close enough to the expected value of 11° not only to confirm our choice of $\theta$ but also to further highlight the bulk origin of the effect and confirm the validity of the model.

On-axis Si(111) data for *pp* and *ps* polarizations were reported by Tsang *et. al* [5] and are shown as the points in Fig. 4.3. These data were obtained at 775 nm using a self-mode-locked Ti:sapphire laser. Surface preparation was not described, so the data presumably pertain to a naturally oxidized sample. The result of fitting the *pp* polarization with $\theta$ and $\beta$ fixed at 11° and 109.4°, respectively, is shown in the top panel of Fig. 4.3. The dashed curve shows the result with $\alpha_{3l}$ (scaling) being the single adjustable parameter. The solid curve is calculated with both $\alpha_{3l}$ and $\alpha_{3t}$ (scaling and offset) adjusted. The offset discrepancy for the longitudinal fit alone has no effect on determining the best-fit lineshape. Here, we find $\alpha_{3t} / \alpha_{3l} = 0.2$. The model prediction for *ps* is compared to data in the second panel of Fig. 4.3. Again, the model calculation provides a good representation of the data, with minor discrepancies that would require a much more comprehensive calculation to describe.

Tsang *et. al* [5] did not report data for the *sp* and *ss* configurations. This may have been a consequence of weaker signals, although Eqs. (4.18) indicate that this should be of the same order of magnitude. While some differences will occur as a result of the Fresnel reflection factors, the SBHM here makes a specific prediction that can easily be tested. The expected lineshapes for the *sp* and *ss* combinations for on-axis Si(111) are shown in the third and fourth panels of Fig. 4.3.

### 4.4.3 Si(001)

Tsang *et. al* [5] also reported *pp* and *ps* THG data for Si(001), which are reproduced as the points in Fig. 4.4. For this orientation the bond vectors incorporating the macroscopic four-fold rotational symmetry is written as (3.7.2). As with Si(111) both longitudinal and transverse contributions can be expressed analytically. The longitudinal contribution is:

$$E_{ppl} = \frac{1}{2}\alpha_l[8\cos^4\frac{\beta}{2}\sin^4\theta - 3\cos^4\theta\sin^4\frac{\beta}{2} - \cos^4\theta\sin^4\frac{\beta}{2}\cos 4\phi] \tag{4.14a}$$

$$E_{psl} = \frac{1}{2}\alpha_l \sin^4\frac{\beta}{2}\cos^3\theta\sin 4\phi\,, \tag{4.14b}$$

$$E_{spl} = \frac{1}{2}\alpha_l \sin^4\frac{\beta}{2}\cos\theta\sin 4\phi\,, \tag{4.14c}$$

$$E_{ssl} = \frac{1}{2}\alpha_l \sin^4\frac{\beta}{2}(3+\cos 4\phi) \tag{4.14d}$$

and the transverse contribution is obtained as with the (111) orientation, adding the same terms to Eqs. (4.14a) and (4.14d) as are added to Eqs. (4.13a) and (4.13d), respectively. The intensity anisotropies for *ps* and *sp* will exhibit purely eight-fold symmetry.

Results of the fitting procedure for the *pp* configuration are shown in the top panel of Fig. 4.4 for scaling ($\alpha_{3l}$) varied and the solid line for scaling and offset ($\alpha_{3l}$ and $\alpha_{3t}$) varied. The agreement is good, but only when both contributions are considered. The ratio of transverse and longitudinal hyperpolarizabilities is now found to be $\alpha_{3t}/\alpha_{3l} = 0.9$. The expected *ps* anisotropy is compared to data in the lower part of Fig.

4.4. The expected eightfold period is obtained, although the data appear to show a twofold variation that is not present in the model, nor is expected for reasons of macroscopic symmetry. The origin of this twofold contribution is not clear.

Lüpke *et al*. [4] reported *ps* data for vicinal Si(001), which are shown as points in Fig. 4.5, together with a fit that adjusts the scaling factor $\alpha_{3l}$ only. The model represents these data excellently well. Since the longitudinal and transverse components have the same functional form for the *ps* and *sp* combinations, their relative contributions cannot be determined from these data.

### 4.4.4 Si (110)

For Si(110) the bond vectors can be written

$$\hat{b}_{1,2} = \hat{x}\sin\frac{\beta}{2} - \hat{y}\cos\frac{\beta}{2}, \tag{4.15a}$$

$$\hat{b}_{1,2} = -\hat{x}\sin\frac{\beta}{2} - \hat{y}\cos\frac{\beta}{2} \tag{4.15b}$$

$$\hat{b}_{3,4} = \hat{y}\cos\frac{\beta}{2} + \hat{z}\sin\frac{\beta}{2}, \tag{4.15c}$$

$$\hat{b}_{3,4} = \hat{y}\cos\frac{\beta}{2} - \hat{z}\sin\frac{\beta}{2} \tag{4.15d}$$

The analytic expressions for the longitudinal component are:

$$\begin{aligned} E_{ppl} = -\frac{1}{8}\alpha_l[&-16\sin^4\frac{\beta}{2}\sin^4\theta + 3\cos^4\theta(2\sin^4\frac{\beta}{2} + \sin^2\beta \\ &+ 4\cos^4\frac{\beta}{2} + 8\cos^4\theta(\sin^4\frac{\beta}{2} - 2\cos^4\frac{\beta}{2})\cos 2\phi \\ &+ \cos^4\theta(2\sin^4\frac{\beta}{2} - 3\sin^2\beta + 4\cos^4\frac{\beta}{2})\cos 4\phi] \end{aligned} \tag{4.16a}$$

$$E_{psl} = -\frac{1}{32}\alpha_l \cos\theta\,[(24\sin^2\beta\sin^2\theta + 6\cos^2\theta + 24\cos^2\theta\cos\beta + 2\cos^2\theta\cos 2\beta)\sin 2\phi - \cos^2\theta(3 + 4\cos\beta + 9\cos 2\beta)\sin 4\phi\,] \quad (4.16b)$$

$$E_{spl} = \frac{1}{32}\alpha_l \cos\theta\;[(16 + 24\cos\beta + 2\cos 2\beta)\sin 2\phi + (3 + 4\cos\beta + 9\cos 2\beta)\sin 4\phi\,] \quad (4.16c)$$

$$E_{ssl} = \frac{1}{32}\alpha_l[(33 + 12\cos\beta + 3\cos 2\beta) + (12 + 48\cos\beta + 4\cos 2\beta)\cos 2\phi + (3 + 4\cos\beta + 9\cos 2\beta)\cos 4\phi] \quad (4.16d)$$

The expressions for the transverse component are obtained in the same way as for the (111) and (001) orientations.

THG data are not presently available for Si(110). However, we can compare our results to the general tensorial *sp* expression reported by Sipe [13]. Sipe found constant, sin2ϕ, cos2ϕ, sin4ϕ, and cos4ϕ Fourier coefficients for the radiation field in the far zone under *p*–polarized excitation, which he wrote as

$$E_{sp}^{3\omega} = -A_{sp}\frac{g_{3b}}{2N}(A - B)[a^{sp} + b_2^{sp}\sin 2\phi + c_2^{sp}\cos 2\phi + b_4^{sp}\sin 4\phi + c_4^{sp}\cos 4\phi] \quad (4.17)$$

The coefficient ratios $a^{sp} : b_2^{sp} : c_2^{sp} : b_4^{sp} : c_4^{sp}$ follow the same proportions as $E_s$: $E_p$: $E_s$: $E_p$: $E_s$. Since $E_p >> E_s$ in this experiment we can say that our results, which predict only constant, sin2ϕ, and sin4ϕ components, are reasonable.

## 4.5 Estimation of relative bulk and surface contributions

We calculate the effects of finite penetration and emergence depths and estimate the relative bulk and surface contributions with a simple model. We assume that the field generated at each bond is proportional to the driving field at the bond. Making a continuum approximation, assuming normal incidence, and assuming that the surface and bulk hyperpolarizabilities are identical, the fields emerging from the surface and bulk in THG are therefore proportional to

$$\vec{E}_{3\omega}^{far} \propto \int_0^d e^{i(k_1+k_2)z}dz + \int_d^\infty e^{i(k_1+k_2)z}dz \approx d + i/(k_1+k_2) \qquad (4.18)$$

where $d$ is the thickness of the surface region and $k_1$ and $k_2$ are the wavevectors of the driving and SHG fields, respectively. Assuming that the surface term is small and that the wavevector $k_1$ is real, both good approximations for typical driving frequencies for Si, the relative surface and bulk contribution to the observed intensity is

$$\frac{I_{2s}}{I_{2b}} = -2\,\mathrm{Re}[i(k_1+k_2)d] = \frac{4\pi d}{\lambda_2}\kappa_2 \qquad (4.19)$$

where $\lambda_2$ and $\kappa_2$ are the wavelength and extinction coefficient of the SHG signal. If the surface signal is weak compared to that of the bulk, as is the case in THG discussed in the next chapter, the surface contribution essentially becomes observable only because it is phase-coherent with the bulk. The assumption that the surface and bulk hyperpolarizabilities are identical is not expected to be valid in practice, but the modification necessary to incorporate this generalization into Eq. (4.19) is obvious.

As an example of how the relative contributions can be determined we consider our present application, crystalline Si at a driving wavelength of 765 nm (1.623 eV). Here, the third-harmonic wavelength is 255 nm (4.868 eV). The extinction coefficient $\kappa_3$ at 4.868 eV is 3.83, so if we assume that the surface signal arises from the two outermost atomic layers ($d \approx 0.25$ nm) the ratio is 0.047. Since the ordinary refractive index $n_3$ of Si at 4.868 eV is 1.63, this ratio could vary from 0 to 0.051 depending on the relative phases of surface and bulk hyperpolarizabilities. The calculation should be considered a guide only, since differences between bulk and surface hyperpolarizabilities are expected and could be substantial.

It is interesting that perhaps the simplest estimation yields almost exactly the same results. We only compare the thicknesses of the surface and bulk regions. For Si the interface can be considered to be about two monolayers thick, i.e., about half a lattice constant of 0.27nm. We take for the bulk thickness the lesser of the penetration depths of the incident and generated third-harmonic waves. Since Si is almost transparent at 765nm, the effective thickness of the bulk is equal to the penetration depth of the third-harmonic wave. At 255nm, the absorption coefficient is $1.9\times10^6$/cm, so the penetration depth is about 5.3nm. As a result, the ratio is estimated to be 5%. This supports the idea that the hyperpolarizabilities of bulk and interface regions may be similar in magnitude.

## *4.6 Conclusions*

We have extended the SBHM to the case of bulk THG for tetrahedrally bonded crystals of cubic symmetry and have applied the results to crystalline Si. For (111), (001), and (110) orientations the expressions for the longitudinal and transverse contributions

are simple enough to allow the THG fields to be expressed analytically for all four polarization combinations *pp*, *ps*, *sp*, and *ss*. For orientations and polarization combinations for which data are available the model agrees well with the data. For *sp* and *ps* data only scaling factors are required. For *pp* and *ss* data a transverse contribution, assumed to be rotationally symmetric with respect to a given bond, must be included. The *ss* and *pp* combinations contain these lower-symmetry azimuth-independent contributions, whereas the *ps* and *sp* combinations do not.

We also establish the connection between the microscopic longitudinal and transverse hyperpolarizabilities and the two independent coefficients of the fourth-rank third-order susceptibility tensor. As with previous applications to interface SHG, the ability of such a simple model to describe a wide range of data indicates that the major fraction of bulk THG signals arises essentially from geometry. However, the ability to systematically isolate geometric contributions opens the way for an analysis of the discrepancies between the predictions of the SBHM and the data, which should allow greater insight into nonlinear optical processes.

## *References*


[1] G. D. Powell, J.-F. T. Wang, and D. E. Aspnes, Phys. Rev. **B65**, art. No. 205320 (2002).

[2] J.-F. T. Wang, G. D. Powell, R. S. Johnson, G. Lucovsky, and D. E. Aspnes, J.Vac. Sci. Tech. **B20**, 1699 (2002).

[3] H. J. Peng, E. J. Adles, J. –F. T. Wang, and D. E. Aspnes. Phys. Rev. **B72**, 205203 (2005).

[4] G. Lüpke, D. J. Bottomley, and H. M. van Driel, J. Opt.Soc. Am. **B11**, 33 (1994).

[5] T. Y. F. Tsang, Phys. Rev. **A52**, 5 (1995).

[6] J. E. Sipe, D. J. Moss, and H. M. van Driel, Phys. Rev **B35**, 1129 (1987).

[7] J.-K. Hansen, H. J. Peng, and D. E. Aspnes, J.Vac. Sci. Technol. **B21**, 1798 (2003).

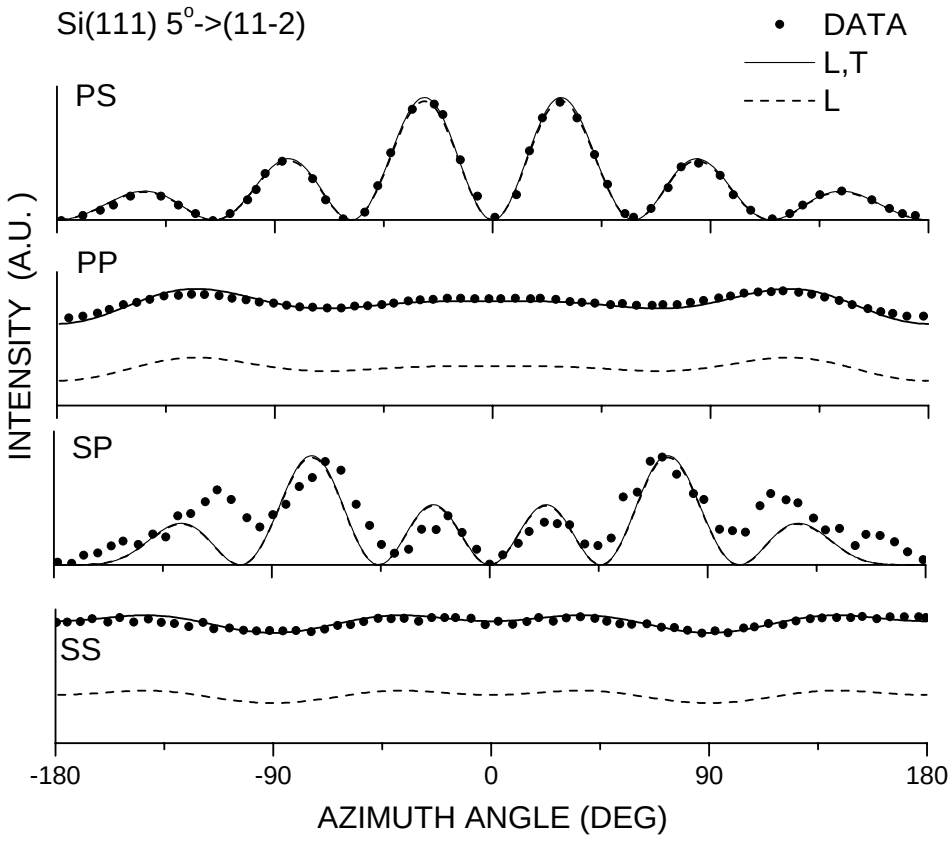



**Figure 4.1 Azimuthal dependences of THG signals for vicinal Si (111) offcut 5° toward $[11\bar{2}]$. Points: data from ref. 14. Lines: SHBM with longitudinal and transverse components both included (solid) and longitudinal component alone (dashed).**

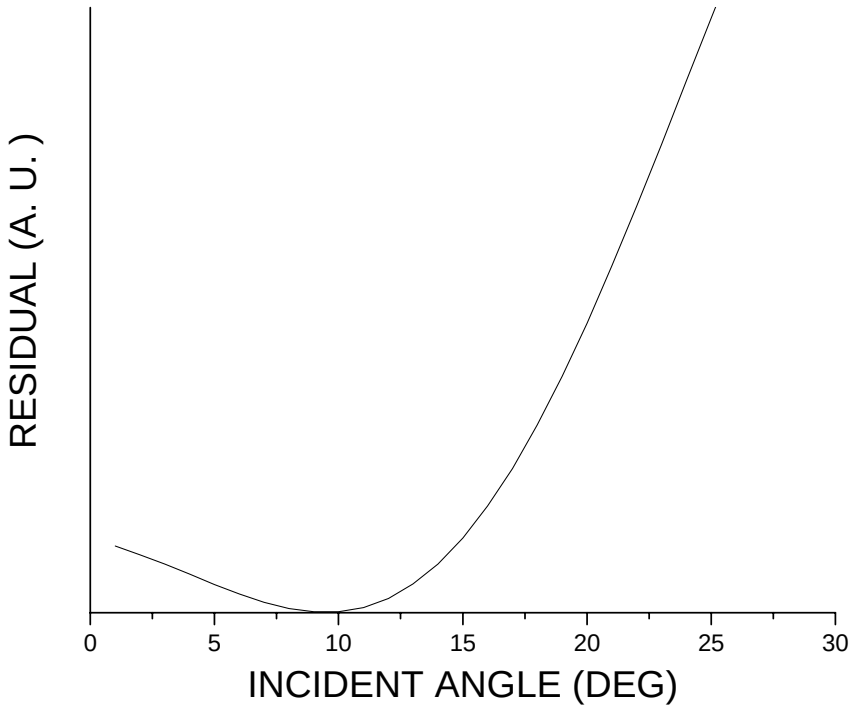



**Figure 4.2 Best-fit residual as a function of angle of incidence $\theta$.**

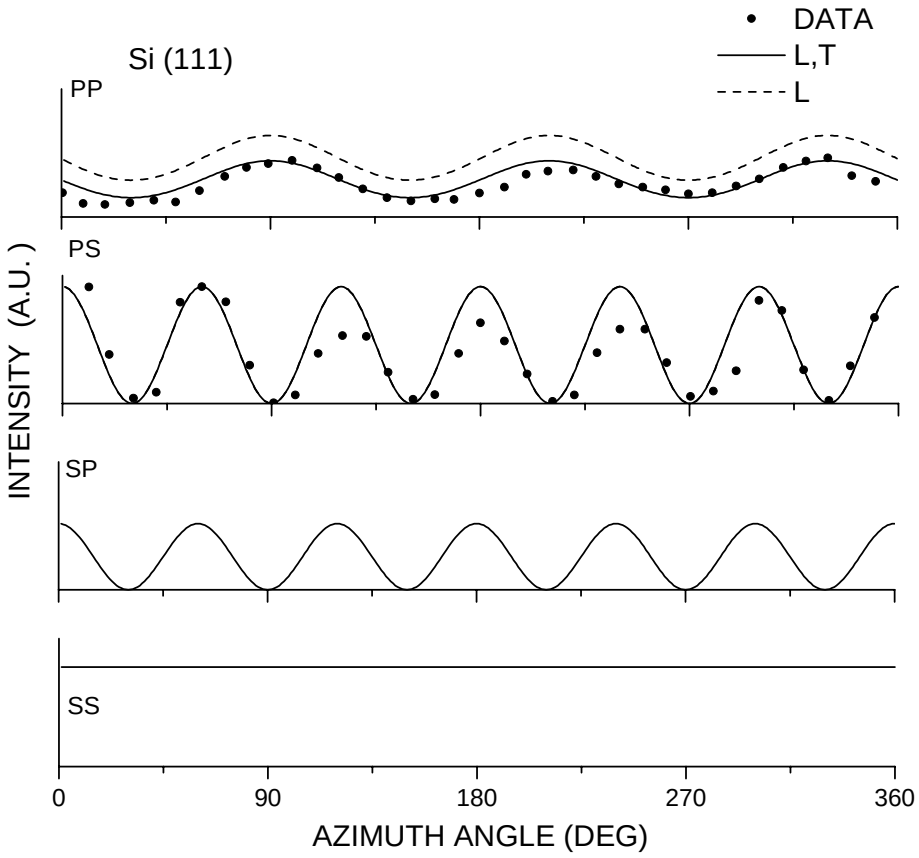



**Figure 4.3 As Fig. 4.1, but for on-axis Si(111). The data are from ref. 20.**

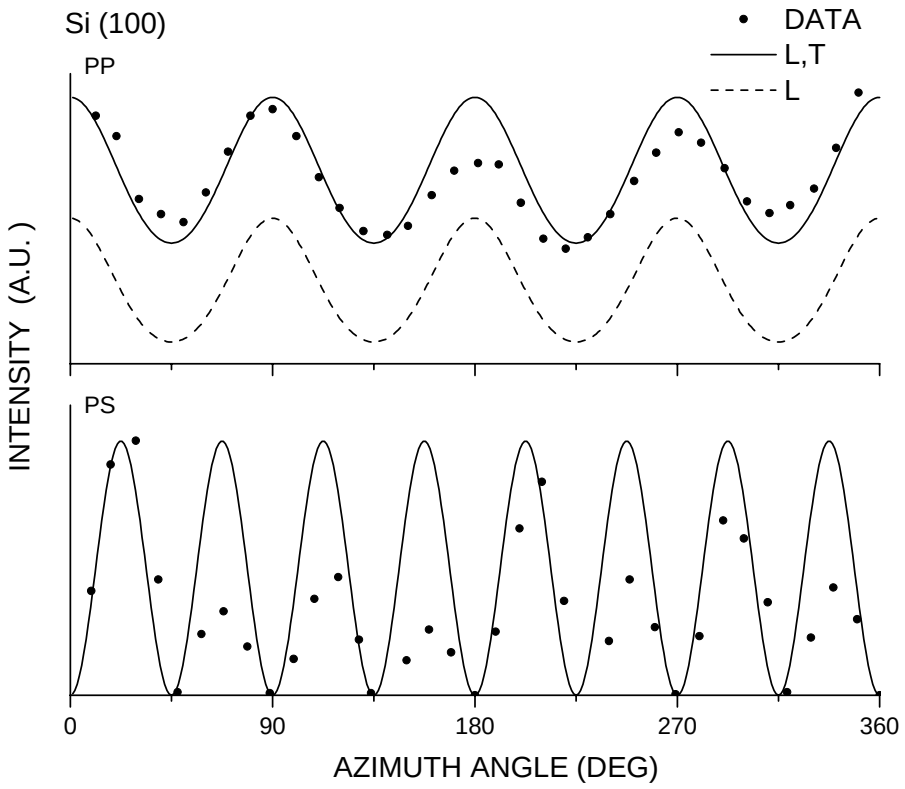



**Figure 4.4 As Fig. 4.1, but for Si (001). The data are from ref. 20.**

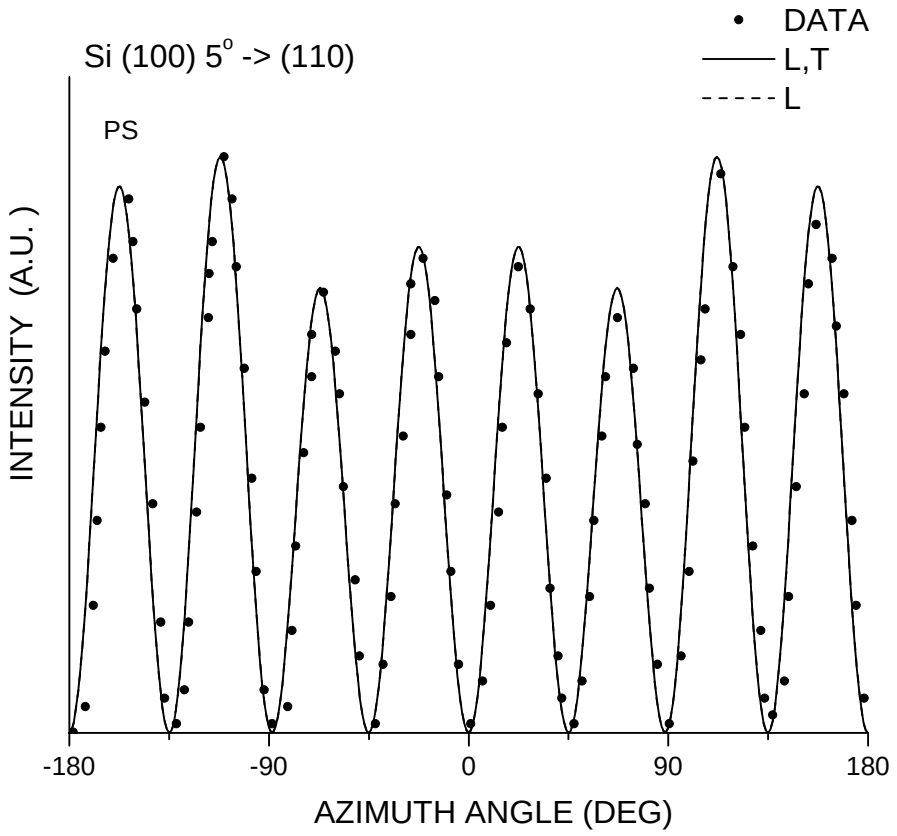



**Figure 4.5 As Fig. 4.1, but for Si (001). The data are from ref. 14.**

# Chapter V. Surface Fourth-Harmonic Generation

## *5.1. Introduction*

Although fourth-harmonic generation (FHG) is much weaker than second harmonic generation (SHG), it is a potential surface diagnostic technology [1-3]. Formalisms currently used to analyze FHG data are basically extensions of theories for SHG. More general approaches may be very complicated since fourth-order susceptibilities are related to fifth-rank tensors. However, in the SBHM the extension from SHG to FHG is very simple, as we showed in Ch. II. This is certainly one of the advantages of the SBHM. Since we have already shown that the higher-order bulk contributions are small in SHG, we will not consider bulk FHG here. We will begin with Eqs. (2.14.d) and (2.15.d),. and we will show that with no adjustable parameters the SBHM is in excellent agreement with *ps* and *ss* data for (001) Si-$SiO_2$ interfaces, and correctly predicts the phases of the *pp* and *sp* data. The *pp* and *sp* data exhibit offsets that can be described by adding a second class of randomly oriented bonds that contribute isotropically to the FHG signal. Consistent with the earlier work of Dadap et al. [5], we attribute this contribution to interface roughness, and show that the fourth-order longitudinal hyperpolarizabilities associated with roughness bonds are at least an order of magnitude larger than those associated with the intrinsic bonds, and have the opposite sign.

## *5.2. Formulation*

From Eq. (2.14.d) we can represent the fourth-harmonic component $\vec{p}_{4j}$ of the induced dipole of the $j^{th}$ bond as

$$\vec{p}_{4j} = q_j \Delta x_4 \hat{b}_j = \alpha_{4j} \left(\hat{b}_j \cdot \vec{E}\right)^4 \hat{b}_j , \tag{5.1.a}$$

$$\vec{E}_{4\omega}^{far} \propto \frac{e^{ikr}}{r} [\underline{1} - \hat{k}\hat{k}] \bullet (\sum \alpha_{4j} \hat{b}_j \hat{b}_j \hat{b}_j \hat{b}_j \hat{b}_j ) \bullet\bullet\bullet\bullet \hat{E}\hat{E}\hat{E}\hat{E}\hat{E} . \tag{5.1.b}$$

where $\alpha_{4j}$ is the microscopic fourth-order longitudinal hyperpolarizability of the $j^{th}$ bond and $\hat{k}$ is the unit vector in the direction of the observer. The observed intensity $I_{4\omega}$ far from the sample is proportional to the absolute square $|\vec{E}_{4\omega}^{far}|^2$ of the field $\vec{E}_{4\omega}^{far}$ that is the coherent sum of the fields radiated by the different bonds.

Since most published second- and fourth-harmonic generation data are in the form of dependences of the observed intensities on the sample azimuth angle $\phi$, we examine the general form that such anisotropies may take. Writing the azimuthal dependence of the field component along the bond axis as

$$\hat{b}_j \cdot \vec{E} = a_0 + a_1 \cos\phi , \tag{1.2}$$

we see from Eq. (5.1.b) that $\vec{E}_{4\omega}^{far}$ will in general contain cosines of integer multiples of $\phi$ up to and including $5\phi$. However, as described below, if $a_0 = 0$ then the resultant variation in intensity will simply be $\cos^8\phi$, a result consistent with the symmetry analysis by Lee and Downer [6].

## *5.3. (001)Si-SiO$_2$ interface*

The bond vectors for Si(001) are given in Eqs. (3.5b). If we assume that the angles of incidence and observation are both equal to $\theta$ and considering incoming and outgoing *s*- and *p*-polarized light separately, we can write the incoming fields as $\vec{E}_s = E_s \hat{y}$ and

$\vec{E}_p = E_p(-\cos\theta\,\hat{x} + \sin\theta\,\hat{z})$, the outgoing wave vector as $\hat{k} = (-\sin\theta\,\hat{x} + \cos\theta\,\hat{z})$, and the outgoing s- and p-polarized beams as the components $\hat{y}$ and $\hat{p}$ = $(\cos\theta\,\hat{x} + \sin\theta\,\hat{z})$, respectively, of the total outgoing field. As a result, we find

$$\begin{aligned}
\vec{E}^{far}_{4\omega,pp} &= \Delta\alpha\,[\cos\theta\sin\frac{\beta}{2}\cos\phi + \sin\theta\cos\frac{\beta}{2}]\times \\
&\qquad [-\cos\theta\sin\frac{\beta}{2}\cos\phi + \sin\theta\cos\frac{\beta}{2}]^4\ \hat{p} \\
&\Rightarrow \frac{1}{2}\Delta\alpha\,\sin\theta\cos\frac{\beta}{2}\,(-9\cos^4\theta\sin^4\frac{\beta}{2} + \\
&\quad 8\sin^2\theta\cos^2\theta\sin^2\frac{\beta}{2}\cos^2\frac{\beta}{2} \\
&\quad + 8\sin^4\theta\cos^4\frac{\beta}{2} - 3\cos^4\theta\sin^4\frac{\beta}{2}\cos 4\phi)\ \hat{p}
\end{aligned} \quad , \qquad (5.3.a)$$

$$\begin{aligned}
\vec{E}^{far}_{4\omega,ps} &= \Delta\alpha[\sin\frac{\beta}{2}\cos\phi][-\cos\theta\sin\frac{\beta}{2}\cos\phi + \sin\theta\cos\frac{\beta}{2}]^4\,\hat{y} \\
&\Rightarrow \frac{1}{2}\Delta\alpha\,\sin\theta\cos\frac{\beta}{2}\,(4\cos^3\theta\sin^4\frac{\beta}{2}\sin 4\phi)\hat{y}
\end{aligned} \quad , \qquad (5.3.b)$$

$$\begin{aligned}
\vec{E}^{far}_{4\omega,xp} &= \Delta\alpha[\cos\theta\sin\frac{\beta}{2}\cos\phi + \sin\theta\cos\frac{\beta}{2}][\sin^4\frac{\beta}{2}\cos^4\phi]\hat{p} \\
&\Rightarrow \frac{1}{2}\Delta\alpha\,\sin\theta\cos\frac{\beta}{2}\,(\sin^4\frac{\beta}{2}\,(3+\cos 4\phi))\,\hat{p}
\end{aligned} \quad , \qquad (5.3.c)$$

$$\begin{aligned}
\vec{E}^{far}_{4\omega,ss} &= \Delta\alpha[\sin\frac{\beta}{2}\sin\phi][\sin^4\frac{\beta}{2}\sin^4\phi]\hat{y} \\
&\Rightarrow 0
\end{aligned} \quad . \qquad (5.3.d)$$

where $\Delta\alpha$ is the difference of the fourth order hyperpolarizability between up and down bonds. In these equations the first entry of a pair is the full expression and the second that which results when the first entry is summed over the four equivalent bonds.

Each single-bond term contains all harmonics of $\phi$ between 0 and $5\phi$, yet the results

summed over four equivalent bonds separated by 90° contain only the 0 and $4\phi$ components. This is a standard result; since summing over equivalent bonds has the same effect as Fourier transformation in that the surviving terms have the same symmetry as the collection of bonds over which the sum is performed. Thus for example for a single bond the full harmonic spectrum of $\vec{E}^{far}_{4\omega,pp}$ contains terms proportional to 1, $\cos\phi$, $\cos 2\phi$, $\cos 3\phi$, $\cos 4\phi$, and $\cos 5\phi$, which upon squaring to calculate the intensity results in principle in a full complement of contributions up to and including $\cos 10\phi$. However, if the total field is the coherent superposition of contributions from four identical bonds separated by 90°, only the terms proportional to 1 and $\cos 4\phi$ survive, leading to intensity contributions proportional to 1, $\cos 4\phi$, and $\cos 8\phi$. It follows that if the two bonds at 0° and 180° are different from those at 90° and 270°, then a $\cos 2\phi$ term would also survive in the field superposition, leading to additional contributions of $\cos 2\phi$ and $\cos 6\phi$ in $I_{pp}$. This provides an immediate experimental opportunity to check the assumption that the four bonds of Fig. 3.2 are equivalent and that their contributions add coherently.

The same considerations for $\vec{E}^{far}_{4\omega,ps}$, $\vec{E}^{far}_{4\omega,sp}$, and $\vec{E}^{far}_{4\omega,ss}$ show that the complete set of field terms for a single bond in these three cases are proportional to $\sin\phi$, $\sin 2\phi$, $\sin 3\phi$, $\sin 4\phi$, and $\sin 5\phi$; 1, $\cos\phi$, $\cos 2\phi$, $\cos 3\phi$, $\cos 4\phi$, and $\cos 5\phi$; and $\sin\phi$, $\sin 3\phi$, and $\sin 5\phi$, respectively. Thus any inequivalency in the set of four bonds would generate a rich harmonic structure in the intensities associated with these configurations. The absence of such structure in the data, and in particular in the vanishing of $\vec{E}^{far}_{4\omega,ss}$ to experimental uncertainty in the data of [2], is good evidence that such asymmetries do not exist and in

particular that the surface areas of the two inequivalent domains of the (001)Si interface are equal, at least to the precision of the data.

The above conclusions are also easily generalized to situations where the symmetry is effectively lower, i.e., for a rough surface where we might expect a random distribution of bonds. Summing over such bond sets in general suppresses all but the isotropic term. For example, the simplest representation of a completely random orientation of equivalent bonds would be to add four more bonds at initial angles of 45°, 135°, 225°, and 315° to those of Fig. 3.2. It is easily seen that the contribution of four additional bonds of this type has the same constant value but a $\cos 4\phi$ contribution of opposite sign, thereby leading only to a constant contribution in the associated intensity.

## *5.4. Comparison with experiment*

Lee and Downer [2] reported results of FHG anisotropy measurements from (001)Si-$SiO_2$ interfaces measured at angles of incidence and observation of 45°, to which we can compare the above results. As discussed previously [4], our calculations are done with $\theta = 29.1°$ to incorporate the effect of refraction at the air-$SiO_2$ interface. Although the refractive indices at the driving and fourth-harmonic fields are different, this difference is minor for $SiO_2$ and we neglect it here. The data of ref. 2 are shown in Fig. 5.1, along with calculations in the SBHM as discussed below. It is important to note that both data and calculations contain scaling factors that are presently arbitrary, depending not only on the average incident power but also the detailed time dependence of the field. Therefore, for display purposes we normalize the pp, ps, and sp data to the dominant azimuthal Fourier components of the intensities $I_{pp}$, $I_{ps}$, and $I_{sp}$, which are $\cos 4\phi$, $\cos 8\phi$,

and cos4$\phi$, respectively. The intensity $I_{ss}$ is zero to within experimental uncertainty. For completeness the scaling factors for $I_{pp}$, $I_{ps}$, and $I_{sp}$ with respect to the raw data are the reciprocals of 1690, 40.2, and 104, respectively. For $I_{ss}$ we use the reciprocal of 100, which is consistent with that for $I_{sp}$.

The anisotropies calculated in the SBHM with the dominant Fourier coefficients in the first three cases normalized in the same way are also shown in Fig. 5.1 As can be seen the SHBM describes the $I_{ps}$ and $I_{ss}$ data almost perfectly. For $I_{pp}$ and $I_{sp}$ the lineshapes and phases are predicted correctly, but the calculated dependences exhibit an offset (constant background) that is different from the data. Since the calculations are done with no adjustable parameters except for scaling factors, the observed agreement for all four polarization combinations is clearly a consequence of the geometric and symmetry properties of the lattice of covalent bonds. However, to explain the offset discrepancy for $I_{pp}$ and $I_{sp}$ we must consider additional effects.

The key to understanding the offset discrepancy is the data of Lee and Downer [2] as a function of etching time, as reproduced in Fig. 5.2. These data exhibit the anisotropy changes that result when the (001)Si surface is etched in a 7:1 $NH_4F$:HF solution for different durations. This etch roughens this surface, and therefore the interface between the (001)Si substrate and the $SiO_2$ overlayer that grows after the sample is removed from the etch [7]. These data clearly show that the relative magnitudes of the isotropic and azimuthally dependent contributions depend on how much the surface has been roughened.

We can incorporate the effect of surface roughness in the SBHM by assuming

that a fraction f of the interface bonds are statistically distributed in azimuth with a different hyperpolarizability $\Delta\alpha_r$ and mean angle $\beta_r$ with respect to the z axis. From our previous discussion regarding symmetry, we would expect these bonds to contribute to the constant term but not to any others. In support, Eqs. (5.3) show that $\vec{E}^{far}_{4\omega,ps}$ and $\vec{E}^{far}_{4\omega,ss}$ have no dc terms for any values of $\theta$ and $\beta_4$. Hence with this assumption the model predicts that offset discrepancies will affect only $I_{pp}$ and $I_{sp}$, in agreement with experiment.

The need for two parameters to describe roughness follows from Fig. 5.1 and additional considerations of Eqs. (5.3). We first note that the predicted offset for $I_{sp}$ is larger than that observed, whereas that for $I_{pp}$ is smaller. From Eq. (5.3c) the only way the offset of $I_{sp}$ can be reduced through the use of an additional constant term is if $\Delta\alpha_4$ and $\Delta\alpha_r$ have opposite signs. However, if $\beta_r = \beta_4 = 54.7356°$ then by Eq. (5.3a) the $I_{pp}$ offset will also be reduced, leading to a greater discrepancy for the pp configuration. But if $\beta_r$ is less than the cutoff value $\beta_{r0} = 34.2°$ for $\theta = 29.1°$, defined as that value of $\beta_r$ for which the constant contribution vanishes, then the constant term will have the opposite sign and the $I_{pp}$ discrepancy will also be reduced. Thus we conclude that microscopic roughness can indeed provide the explanation for the offset discrepancies in $I_{pp}$ and $I_{sp}$, but only if $\Delta\alpha_4$ and $\Delta\alpha_r$ have opposite signs and $\beta_r$ is less than 34.2°. The nearly systematic reduction in the offset with increased etching seen in Fig. 3 can therefore be attributed to a nearly systematic increase in the fraction of random bonds. Since the fraction $f$ of random bonds is likely to be substantially less than the fraction $(1 - f)$ of

oriented bonds, the data of Fig. 5.2 imply that $\Delta\alpha_r$ is considerably larger than $\Delta\alpha_4$ in addition to having an opposite sign.

We make the above results quantitative by performing a simultaneous least-squares fit of the SBHM to the $I_{pp}$, $I_{ps}$, and $I_{sp}$ data of Fig. 5.1 using the following equations:

$$E_{pp}^{far} = \frac{1}{2}\Delta\alpha \sin\theta\cos\frac{\beta}{2}[-9\cos^4\theta\sin^4\frac{\beta}{2} + 8\sin^2\theta\cos^2\theta\sin^2\frac{\beta}{2}\cos^2\frac{\beta}{2} + 8\sin^4\theta\cos^4\frac{\beta}{2} - 3\cos^4\theta\sin^4\frac{\beta}{2}\cos 4\phi\,] + c_{pp} \tag{5.4.a}$$

$$E_{ps}^{far} = \eta_{ps}\,[\frac{1}{2}\Delta\alpha\,\sin\theta\cos\frac{\beta}{2}\,(4\cos^3\theta\sin^4\frac{\beta}{2}\,\sin 4\varphi)]; \tag{5.4.b}$$

$$E_{sp}^{far} = \eta_{sp}\,[\frac{1}{2}\Delta\alpha\,\sin\theta\cos\frac{\beta}{2}\,(\sin^4\frac{\beta}{2}\,(3+\cos 4\varphi))] + c_{sp}\,], \tag{5.4.c}$$

where $\eta_{ps}$ and $\eta_{sp}$ are scaling factors, and $c_{pp}$ and $c_{ss}$ are the azimuth-independent parts of the corresponding Eqs. (5.4) that describe the effect of roughness. These have the explicit forms:

$$c_{pp} = \frac{1}{2}\Delta\alpha_r\,\sin\theta\cos\beta_r\,[-9\cos^4\theta\sin^4\beta_r + 8\sin^2\theta\cos^2\theta\sin^2\beta_r\cos^2\beta_r + 8\sin^4\theta\cos^4\beta_r \tag{5.5.a}$$

$$c_{sp} = \frac{3}{2}\Delta\alpha_r\,\sin\theta\cos\beta_r\,\sin^4\beta_r\,. \tag{5.5.b}$$

The justification for $\eta_{ps}$ and $\eta_{sp}$ is that the data are scaled arbitrarily, recalling that $\Delta\alpha$ is performing the same function for $I_{pp}$. The results of the fitting procedure are shown in Fig. 5.3. The values of the parameters are $\Delta\alpha$ = 2.895; $c_{pp}$ = –0.7903; $\eta_{ps}$ = 2.949; $\eta_{sp}$

= 3.885; and $c_{sp}$ = –0.3583. It is clear that the model gives an excellent representation of the data.

We can now find $\beta_r$ and $\Delta\alpha_r/\Delta\alpha$ by equating the determined values of $c_{pp}$ and $c_{sp}$ to the corresponding Eqs. (5.4). We find $\beta_r = 27.2°$ and $\Delta\alpha_r = -12.63$ referenced to $\Delta\alpha = 2.90$, which yields $\Delta\alpha_r/\Delta\alpha_4 = -4.36$. Since the surface density of bonds associated with roughness is expected to be much less than the intrinsic bond density of 2 per surface atom, it is clear that the fourth-order longitudinal hyperpolarizability of the former is much larger than that of the latter. For example if 10% of the interface bonds are associated with roughness, the fourth-order longitudinal hyperpolarizability ratio is not only of the opposite sign but some 50 times larger.

With $\beta_r$ established and unlikely to change significantly with etching, we can now determine the $\Delta\alpha_r/\Delta\alpha$ ratio for the data of Fig. 5.3 We write $E_{sp} = a + b\cos 4\phi$, in which case

$$\begin{aligned} I_{sp} &= a^2 + b^2/2 + 2ab\cos 4\phi + (b^2/2)\cos 8\phi \\ &= c_0 + c_4\cos 4\phi + c_8\cos 8\phi \end{aligned}, \qquad (5.6.a)$$

so

$$a = (c_0 - c_8)^{1/2}\,; \qquad b = c_4/(2a) = (2c_8)^{1/2}\,.; \qquad (5.6.b)$$

where $c_0$, $c_4$, and $c_8$ are the Fourier (= best-fit) coefficients for the spectra. After some algebra we find

$$\frac{\Delta\alpha_r}{\Delta\alpha_4} = \left(\frac{a}{3b} - 1\right)\frac{\cos\beta/2\sin^4\beta/2}{\cos\beta_r\sin^4\beta_r}, \qquad (5.7)$$

which is the desired connection between the Fourier coefficients and the hyperpolarizability ratio.

The best-fit lineshapes are also shown in Fig. 5.2. In all cases the calculated lineshapes fit the observed anisotropies remarkably well. Evaluating the results with Eqs. (3.6) and (3.7) we find values of the ratio of –4.37, –4.23, –5.17, –6.14, and –5.59 for exposures of 0, 10, 20, 30, and 60 min, respectively. Thus the fraction of bonds associated with roughness increases with increasing etching time, although not monotonically.

## *5.5 Conclusions*

We have shown that the SBHM can be applied to describe observed anisotropies of fourth-harmonic intensities of (001)Si-$SiO_2$ interfaces provided that we include a separate, isotropic contribution from bonds affected by interface roughness. With data and model calculations both normalized to the largest Fourier coefficient, the SBHM predicts the lineshapes of the *ps* and *ss* results and the phases of the *pp* and *sp* results with no adjustable parameters. The *pp* and *sp* data exhibit offsets that cannot be described with the intrinsic interface bonds alone, but can be explained by assuming a second set of interface bonds that are associated with interface roughness. By least-squares fitting the predictions of analytic expressions derived in the text to the pp and sp data we find that the bond angle associated with roughness is about half that associated with intrinsic bonding. In addition, the fourth-order longitudinal hyperpolarizabilities have opposite signs, and that associated with roughness is probably about an order of magnitude larger.

The fact that this simple representation describes essentially all FHG data to within experimental uncertainty indicates that the amount of interface information obtainable from FHG may be limited to the extent that the expense of setting up the necessary equipment may not be justified. However, it should be noted that the macroscopic fourfold rotation symmetry of (001)Si interfaces is too high to be accessible by SHG. More critical tests of the capabilities of FHG and that of the SBHM to describe it will be provided when accurate values for the relative strengths of the *pp*, *ps*, and *sp* signals are obtained, and when FHG measurements are performed as a function of wavelength.

## *References*


1. Y.-S. Lee, M. H. Anderson, and M. C. Downer, Opt. Lett. **22,** 973 (1997).

2. Y.-S. Lee and M. C. Downer, Opt. Lett. **23**, 918 (1998).

3. Y.-S. Lee and M. C. Downer, Thin Solid Films **364**, 80 (2000).

4. G. D. Powell, J.-F. T. Wang, and D. E. Aspnes, Phys. Rev. **B 65**, art. No. 205320 (2002).

5. J. I. Dadap, B. Doris, Q. Deng, M. C. Downer, J. K. Lowell, and A. C. Diebold, Appl. Phys. Lett., **64**, 16 (1994).

6. Y. R. Shen, *The Principles of Nonlinear Optics*, Wiley, New York, 1984.

7. K. Sawara, T. Yasaka, S. Miyazaki, and M. Hirose, J. Appl. Phys. Jpn. **31**, L931 (1992).

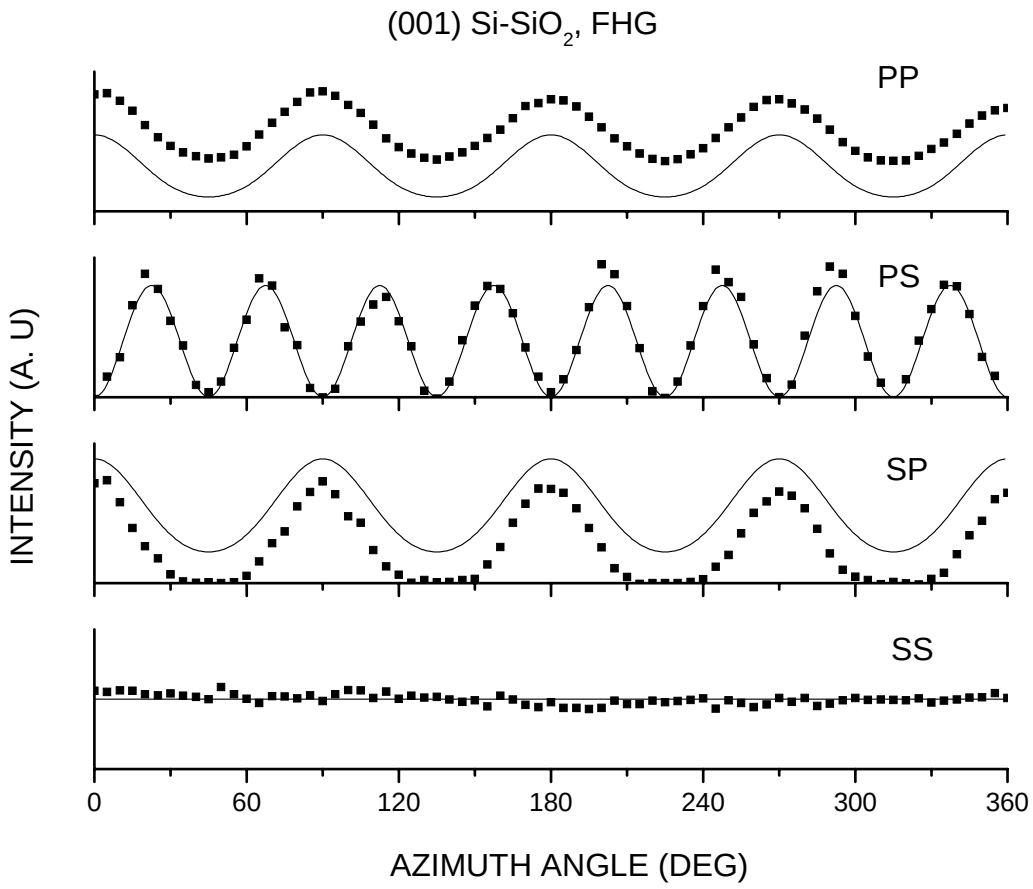



**Figure 5.1 Normalized FHG anisotropies for the (001)Si-$SiO_2$ interface for the polarization combinations *pp*, *ps*, *sp*, and *ss*, as reported in ref. 2. The solid curves are the SBHM results.**

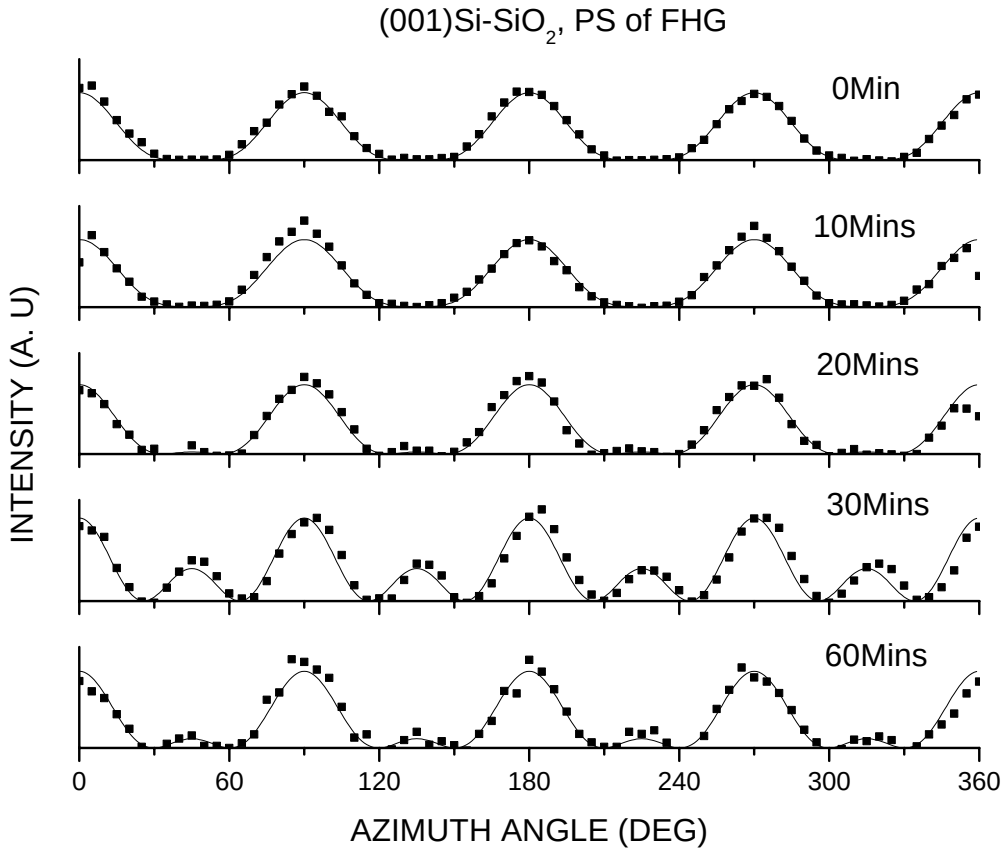



**Figure 5.2 Normalized FHG anisotropies of (001)Si immediately following exposure of the sample to a buffered oxide etch for durations of 0 (top), 10, 20, 30, and 60 min (bottom). The solid curves are the result of SBHM calculations taking into account interface roughening.**

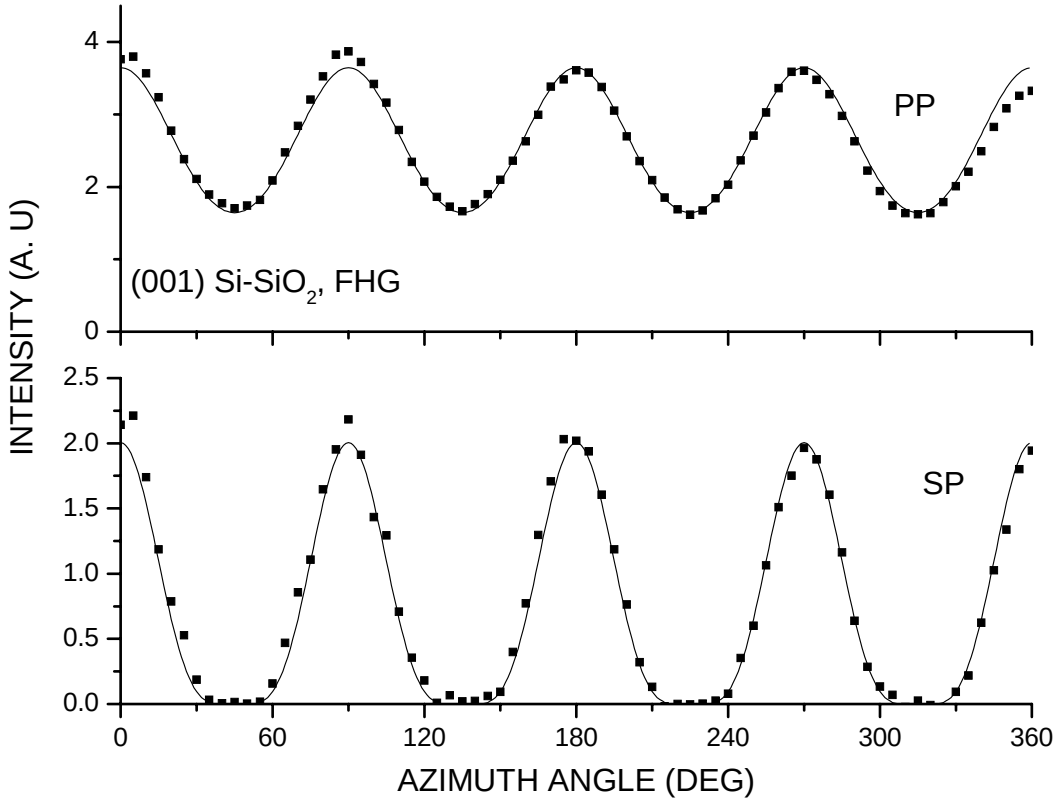



**Figure 5.3 Normalized FHG anisotropies for the (001) Si-$SiO_2$ interface for the polarization combinations *pp* and *sp*. The solid curves are the result of SBHM including interface roughness.**

# Chapter VI Dipole-Radiation Model for Terahertz Radiation from Semiconductors

## *6.1 Introduction*

The generation of terahertz (THz) radiation by irradiating semiconductors with ultrafast pulses in the 800 nm wavelength range has been extensively investigated owing to the lack of convenient alternative sources of these potentially useful frequencies [1-6]. Descriptions of THz generation include the current-surge model of Shan and Heinz [5, 6] for free carriers and the frequency-mixing approach of Morris and Shen [8] and Khurgan [9] for bound charges. The former accounts well for the frequency dependence and magnetic field enhancement of the radiation when free carriers are present, but contains no means of generating azimuthal dependences [4, 7]. The latter provide phenomenological descriptions of the azimuthal dependence, but not the free-carrier background. Saeta *et al.* [1] attempted to separate these contributions from data, but performed the calculation at the intensity, not the field, level. Since the two contributions are driven coherently by a common field, an intensity calculation does not properly combine them. The purpose of Ch. V. is to investigate the consequences of a coherent superposition at the field level, using a simple dipole-radiation model that provides insight into the origin of the bulk response. Analytic expressions for the combination are obtained.

## *6.2 Formulation*

Our approach is an extension of the SBHM, which accurately describes the azimuthal dependences of SHG, THG, and FHG from both bulk and interface regions in

terms of parameters that have direct physical meanings on the microscopic scale [10-12]. In this model NLO effects are described as the superposition of dipole radiation from charges accelerated by the external driving field, and hence is effectively the extension of the linear-optic calculations of Ewald [13] and Oseen [14] to NLO. The basic assumptions are described previously. With these assumptions motion can be described with a one-dimensional force model, which we will apply to both free carriers and bond charges. We will also consider the time dependence of the driving field itself, since THz radiation arises from interference between different Fourier components of the (short) pulse used to excite the charges (optical rectification).

We will first calculate the Thz field from bond charges because it is simply an adaptation of the calculations of previous chapters. The one-dimensional force equation for difference-frequency mixing is

$$\begin{aligned} F = m\frac{d^2x}{dt^2} &= q_j(\vec{E}_1 \bullet \hat{b}_j e^{-i\omega_1 t} + \vec{E}_2 \bullet \hat{b}_j e^{-i\omega_2 t} + c.c) \\ &- \kappa_1(x - x_0) - \kappa_2(x - x_0)^2 \end{aligned} \tag{6.1.a}$$

if we write the displacement as

$$\begin{aligned} x = x_0 &+ \Delta x_{11}e^{-i\omega_1 t} + \Delta x_{12}e^{-i\omega_2 t} + \Delta x_{21}e^{-i2\omega_1 t} + \Delta x_{22}e^{-i2\omega_2 t} \\ &+ \Delta x_{23}e^{-i(\omega_1+\omega_2)t} + \Delta x_{24}e^{-i(\omega_1-\omega_2)t} + \text{c.c} \end{aligned} . \tag{6.1.b}$$

Using the bond vector of Eq. (3.7.a) we obtain

$$E_{BC}^{P} \propto \sin 2\phi , \tag{6.2.a}$$

$$E_{BC}^{S} \propto \cos 2\phi , \tag{6.2.b}$$

where the subscript BC denotes bond charge and the superscripts p and s indicate the polarization of the outgoing waves. The incident wave is assumed to be p-polarized.

For free carriers, the first problem is to determine the nonlinearity mechanism. For bond charges nonlinearity results primarily from anharmonic restoring forces, but these do not exist for free carriers. However, we recall from Ch. II that spatial dispersion gives rise to a SHG contribution. In the free-carrier case we start from the one-dimensional force law

$$\vec{F} = m\frac{d^2\Delta\vec{r}}{dt^2} = q\vec{E}e^{-i\omega t} \tag{6.3.a}$$

where

$$\Delta\vec{r} = \Delta\vec{r}_1 e^{-i\omega t} + \Delta\vec{r}_2 e^{-i2\omega t} \tag{6.3.b}$$

and

$$\vec{E}e^{-i\omega t} = (\vec{E} + \Delta\vec{r}\cdot\nabla\vec{E})e^{-i\omega t}. \tag{6.3.c}$$

With these 3 equations we can solve for the displacement of the free carriers, which we find to be

$$\Delta\vec{r}_1 = -\frac{q\vec{E}}{m\omega^2}, \tag{6.4.a}$$

$$\Delta\vec{r}_2 = \frac{q^2\vec{E}\nabla\vec{E}}{4m^2\omega^4}. \tag{6.4.b}$$

The total dipole density is

$$\vec{P} = qn\Delta\vec{r} \tag{6.5}$$

where n is the charge density.

At this point we note another difference between free and bound charges. For bound charges the charge density is basically invariant while for free carriers the charge density depends on the incident field. To see this we expand the charge density as

$$n = n_0 + n_1 e^{-i\omega t} + n_2 e^{-i2\omega t} + \ldots . \tag{6.6}$$

Then for the lowest-order nonlinearity, SHG, the dipole density is

$$\vec{P}(2\omega) = q n_0 \Delta\vec{r}_2 + q n_1 \Delta\vec{r}_1 \tag{6.7}$$

Using the charge-conservation equation

$$\nabla \cdot \vec{J} + \frac{\partial \rho}{\partial t} = 0 \tag{6.8}$$

we find

$$\begin{aligned} \rho &= qn \\ &= q(n_0 + n_1 e^{-i\omega t} + n_2 e^{-i2\omega t}) \end{aligned} \tag{6.9.a}$$

$$\frac{\partial \rho}{\partial t} = -q(i\omega n_1 e^{-i\omega t} + 2i\omega n_2 e^{-i2\omega t}) \tag{6.9.b}$$

and

$$\begin{aligned} \vec{J} &= \frac{\partial \vec{P}}{\partial t} \\ &= \frac{\partial (qn\Delta\vec{r})}{\partial t} \\ &= -i\omega[q n_0 \Delta\vec{r}_1 e^{-i\omega t} + 2q(n_0 \Delta\vec{r}_2 + n_1 \Delta\vec{r}_1) e^{-i2\omega t}] \end{aligned} \tag{6.9.c}$$

Therefore,

$$\vec{J} = -i\omega[-q n_0 \frac{q\vec{E}}{m\omega^2} e^{-i\omega t} + 2q(n_0 \frac{q^2 \vec{E}\nabla\vec{E}}{4m^2\omega^4} - n_1 \frac{q\vec{E}}{m\omega^2}) e^{-i2\omega t}] \tag{6.9.d}$$

As a result, for the 1ω term we have

$$\nabla \cdot \vec{J} = i \frac{q^2 n_0 \nabla \cdot \vec{E}}{m\omega} e^{-i\omega t} . \tag{6.9.e}$$

The equivalent part of the charge density is

$$\frac{\partial \rho}{\partial t} = -qi\omega n_1 e^{-i\omega t} \tag{6.9.f}$$

From Eqs. (6.9.e) and (6.9.f) it follows that

$$n_1 = -\frac{qn_0 e^{-i\omega t}}{m\omega^2}\nabla \cdot \vec{E}\,, \tag{6.10}$$

and finally

$$\begin{aligned}\vec{P}(2\omega) &= q(n_0 \Delta\vec{r}_2 + n_1 \Delta\vec{r}_1)e^{-i2\omega t} \\ &= \frac{n_0 q^3}{4m^2\omega^4}(\vec{E}\cdot\nabla\vec{E} + 4\vec{E}\nabla\cdot\vec{E})e^{-i2\omega t}\end{aligned} \tag{6.11}$$

which is the expression needed to describe SHG from free carriers. Substituting the result in the far-field radiation equation we get

$$\vec{E}_{FC}^{\,P} = -\frac{2A}{c^2 r}\{[\frac{\sin\theta}{\varepsilon\cos\theta + \gamma\sin\theta}(\frac{\partial^2 \vec{P}_{FC}}{\partial t^2}\bullet\hat{z} - \gamma\frac{\partial^2 \vec{P}_{FC}}{\partial t^2}\bullet\hat{x})]\bullet (-\hat{x}\cos\theta + \hat{z}\sin\theta)\} \tag{6.12.a}$$

$$\vec{E}_{FC}^{\,S} = -\frac{2A}{c^2 r}(\frac{\hat{y}}{\cos\theta + \gamma\sin\theta}\frac{\partial^2 \vec{P}_{FC}}{\partial t^2}\bullet\hat{y}) \tag{6.12.b}$$

where the superscripts refer to p (TM) and s (TE) polarizations, respectively, A is the area over which the photocurrent is present, r is the distance to the observer, $\gamma = \frac{\sqrt{\varepsilon - \sin^2\theta}}{\sin\theta}$, and the photocurrent is approximated as $\vec{j} = \frac{\partial \vec{P}_{FC}}{\partial t}$. This is the same expression as that given in references 5 and 6. From the above it follows that for free carriers any azimuthal dependence will be small compared to that of the bound charges.

As usual, the electric field in the far-field region can be calculated from the generated dipoles using the projection operator

$$\vec{E}_{THz} = \frac{Z_0 ck^2}{4\pi}\frac{e^{ikr}}{r}(I - \hat{k}\hat{k}) \bullet \vec{P}_{THz} \tag{6.13}$$

where $\hat{k}$ points in the direction of the observer. Here

$$\vec{P}_{THz} = \vec{P}_{BC} + \vec{P}_{FC}, \tag{6.14}$$

where $\vec{P}_{BC}$ and $\vec{P}_{FC}$ are the induced dipoles associated with the bound and free charges, respectively. To within a scaling factor the observed intensity is given by the absolute square of Eq. (6.13). If only the bulk contribution is present the generated THz signal will display a four-fold dependence on $\phi$. However, since the total field is the sum of the fields of the bound and free charges, the observed intensity may display either or both two-fold or four-fold components depending on the relative strengths of these two contributions.

Before we compare theory and experiment, we perform a numerical calculation for free-carrier SHG for Cu using Eq. (6.11). If we integrate (6.11), we find for the total dipole density

$$\vec{P}(2\omega) = \int \frac{An_0 q^3}{4m^2\omega^4}(\vec{E}\cdot\nabla\vec{E} + 4\vec{E}\nabla\cdot\vec{E})e^{-i2\omega t}dV, \tag{6.15}$$

where the incident field is given by

$$\vec{E} = (E_0\cos\theta,\ 0,\ E_0\sin\theta)e^{i\vec{k}_0\cdot\vec{r} - i\omega t} \tag{6.16.a}$$

and

$$\vec{k}_0 = (k_0\sin\theta,\ 0,\ k_0\cos\theta) \tag{6.16.b}$$

In the metal the propagation vector is

$$\vec{k}_{metal} = (k_0 \sin\theta,\ 0,\ i\sqrt{\frac{\mu\sigma\omega}{2}}), \tag{6.16.c}$$

where $\sqrt{\frac{\mu\sigma\omega}{2}} >> k_0$. Hence in the metal

$$\vec{E}_{metal} = (E_0 \cos\theta_{metal},\ 0,\ E_0 \sin\theta_{metal}) e^{ik_0 x \sin\theta - \sqrt{\frac{\mu\sigma\omega}{2}} z} \tag{6.17}$$

where $\tan\theta_{metal} = \frac{-ik_0 \sin\theta}{\sqrt{\frac{\mu\sigma\omega}{2}}}$. Therefore, $\theta_{\text{metal}}$ is approximately 0. As a result

$$\begin{aligned}
&\vec{E}_{metal} \nabla \cdot \vec{E}_{metal} = E_0^2 (\cos\theta_{metal},\ 0,\ \sin\theta_{metal}) \cdot \\
&\quad \cos\theta_{metal} (ik_0 \sin\theta - \sqrt{\frac{\mu\sigma\omega}{2}} \tan\theta_{metal}) e^{2ik_0 x \sin\theta - 2\sqrt{\frac{\mu\sigma\omega}{2}} z} \\
&\quad = 2ik_0 \sin\theta E_0^2 (\cos\theta_{metal},\ 0,\ \sin\theta_{metal}) \cos\theta_{metal}\ e^{2ik_0 x \sin\theta - 2\sqrt{\frac{\mu\sigma\omega}{2}} z}
\end{aligned} \tag{6.18}$$

$$\begin{aligned}
&\vec{E} \cdot \nabla \vec{E} = E_0^2 (\cos\theta_{metal},\ 0,\ \sin\theta_{metal}) \cdot \\
&\quad (ik_0 \sin\theta \cos\theta_{metal} - \sqrt{\frac{\mu\sigma\omega}{2}} \sin\theta_{metal}) e^{i2k_0 x \sin\theta - 2\sqrt{\frac{\mu\sigma\omega}{2}} z} \\
&\quad = 2ik_0 \sin\theta E_0^2 (\cos\theta_{metal},\ 0,\ \sin\theta_{metal}) \cos\theta_{metal}\ e^{i2k_0 x \sin\theta - 2\sqrt{\frac{\mu\sigma\omega}{2}} z}
\end{aligned} \tag{6.19}$$

So

$$\begin{aligned}
&\vec{P}(2\omega) = \int \frac{5n_0 q^3}{2m^2\omega^4} ik_0 E_0^2 (\cos^2\theta_{metal}, 0, \frac{\sin 2\theta_{metal}}{2}) \\
&\sin\theta e^{i2k_0 x \sin\theta - 2\sqrt{\frac{\mu\sigma\omega}{2}} z - i2\omega t}\, dxdydz \\
&\quad = -i \frac{5Dn_0 q^3}{4m^2\omega^4} \sqrt{\frac{2}{\mu\sigma\omega}} E_0^2 \sin(k_0 D \sin\theta) \\
&(\cos^2\theta_{metal}, 0, \frac{\sin 2\theta_{metal}}{2}) \sin\theta e^{-i2\omega t}
\end{aligned} \tag{6.20}$$

The total far field is

$$\vec{E}^{\,ff} = Z_0 \frac{ck^2}{4\pi}\frac{e^{ikr}}{r}(\underline{I} - \hat{k}\hat{k})\vec{P} \tag{6.21}$$

So

$$\begin{aligned}\vec{E}^{\,ff}(2\omega) &= Z_0 \frac{c4k^2}{4\pi}\frac{e^{i2kr}}{r}(\underline{I} - \hat{k}\hat{k})\vec{P}(2\omega) \\ &= -iZ_0 \frac{c\mu\sigma\omega}{2\pi}\frac{1}{r}(\underline{I} - \hat{k}\hat{k})\frac{5Dn_0q^3}{4m^2\omega^4} \\ &\sqrt{\frac{2}{\mu\sigma\omega}}E_0^2 \sin(k_0 D\sin\theta)\cdot(\cos^2\theta_{metal},\, 0,\, \frac{\sin 2\theta_{metal}}{2})\sin\theta e^{i2kr - i2\omega t}\end{aligned} \tag{6.22}$$

Performing a numerical estimate for Au

$$\begin{aligned} &\sigma = 0.452\times10^8\,\Omega/m && \mu = 1.256\times10^{-6}\,\text{Tm/A} \\ &\text{c} = 3.0\times10^8\,m/s && Z_0 = 377 \\ &\omega = 3.75\times10^{14}\,Hz && m = 9.1\times10^{-31}\,kg \\ &q = 1.6\times10^{-19}\,C && n_0 = 8.4\times10^{28}/m^3 \\ &D = 4\times10^{-5} && E_0 = 1\times10^8 \\ &r = 0.5m && k_0 = 1.25\times10^6 \end{aligned} \tag{6.23}$$

leads to $\sqrt{\frac{\mu\sigma\omega}{2}} = \sqrt{\frac{1.256\times10^{-6}\times0.452\times10^8\times3.75\times10^{14}}{2}} = 1.032\times10^8$. Using Eq. (6.22)

and setting $\theta_{\text{metal}} = 0$ we obtain

$$\begin{aligned}\vec{E}^{\,ff}(2\omega) &= -i\cdot377\frac{3\times10^8\times1.032\times10^8}{0.5\times3.14}\times \\ &\frac{5\times4\times10^{-5}\times8.4\times10^{28}\times(1.6\times10^{-19})^3}{4\times(9.1\times10^{-31})^2\times(3.75\times10^{14})^4}\times10^{16} \\ &(\underline{I} - \hat{k}\hat{k})\sin(k_0D\sin\theta)\cdot \\ &(\cos^2\theta_{metal},\, 0,\, \frac{\sin 2\theta_{metal}}{2})\sin\theta e^{i2kr - i2\omega t} \\ &= -i\cdot7.8\times10^4\,(\underline{I} - \hat{k}\hat{k})\sin(k_0D\sin\theta)\cdot \\ &(\cos^2\theta_{metal},\, 0,\, \frac{\sin 2\theta_{metal}}{2})\sin\theta e^{i2kr - i2\omega t}\end{aligned} \tag{6.24}$$

Hence for an electric field E ~ $10^8$ V/cm, the SHG field generated by free carriers is of the order of $10^5$ V/cm. Thus if the power of the driving laser is 1W, the generated intensity would be about $10^{-7}$ W. We do not have any data against which to compare this magnitude, but we believe that the order of magnitude of this intensity is correct.

## *6.3 Comparison to data for THz generation from InP*

We now consider the results of Saeta *et al.* [1] for InP, which are shown in Fig. 6.1. These data were obtained on (001)InP sample at an angle of incidence of 66° for the *pp* and 45° for the *ps* cases, respectively. The authors did not mention observation angles, but these should be essentially equal to the incident angles. Since the difference between the refractive indices of InP at the incident and THz frequencies is small, we will assume that they are the same. In our simulation we use $(a\sin 2\phi + b)^2$ and $d\cos 2\phi$ to fit the observed intensities of the *pp* and *ps* signals, respectively, noting from Eq. (6.12a) that the free carriers do not contribute to the radiated s-polarized component for p-polarized incident light. For the other parameters, we use $\theta$ = 15° for the *pp* case and $\theta$ = 11.5° for the *ps* case, which are obtained using the known refractive index of InP at 800 nm and applying Snell's Law. From Fig. 6.1 we see that the model fits the *ps* signal perfectly. For the *pp* signal, the fitting is very good. The agreement in both cases shows that combination at the field level is correct. We obtain an a/b ratio of 0.27. Note that this ratio is not a fixed number, since it depends on the experimental conditions such as incident power, spot size, etc.. For high power densities the bond-charge nonlinearity will dominate and this ratio will be large. For low power densities the free-carrier contribution dominates and the ratio will be small.

We next consider the wavelength dependence of the THz radiation. The combination of free- and bond-charge contributions generates a cross product when the intensity is calculated, since these two processes are coherent, being driven by the same optical beam. The calculated frequency dependence of the bond-charge contribution is shown in Fig. 6.2. These results were obtained by first evaluating the difference mixing for any two frequency components of the pulse wave packet, then using the residual theorem to integrate over the width of the pulse. We used a plasma frequency of $0.7\times10^{12}$ Hz, a carrier frequency of $2\times10^{15}$ Hz, a damping coefficient of $1\times10^{11}$ $s^{-1}$, and a half-width at half-maximum of $3\times10^{14}s^{-1}$. The spectral dependence is similar to that given in the literature [6]. Furthermore, from the ratio obtained above, we find that the contribution of the free carriers is dominant. Clearly, incorporating coherence into the model does not significantly affect the spectroscopic results.

Finally, we consider the effect of a magnetic field on the THz intensity. Since the bond charges are tightly bound, we can assume that the magnetic field has little effect on them. Hence only the free charges will be affected by the magnetic field. According to the Lorentz force law

$$\vec{F} = \rho_c V_0 \vec{E} - \vec{k}\Delta\rho_c + \rho_c V_0 \vec{v} \times \vec{B} = \rho_m V_0 \vec{a} \tag{6.25}$$

where $V_0$ is the volume, $\rho_c$ the charge density, $\rho_m$ the mass density, $\vec{k}\Delta\rho_c$ describes the effects on the charge density variation, and $\vec{v}$ and $\vec{a}$ are the velocity and acceleration, respectively. Assuming that the electric and magnetic fields are along the z and x directions, respectively, we can solve the above force equation. The results are

$$a_y = -\frac{\omega E_{eff}}{B}\sin\omega t\,, \tag{6.26.a}$$

$$a_z = -\frac{\omega E_{eff}}{B}\cos\omega t\,, \tag{6.26.b}$$

where $\omega = \frac{\rho_c}{\rho_m}B$, $E_{eff} = E - \frac{k\Delta\rho}{\rho_c V_0}$, and we assume that $\vec{k}$ is in the same direction as $\vec{E}$.

Our results are similar to those of Takahashi *et al.* [4, 5]. Since the dipole moment is proportional to the acceleration, from above equations we see that the dipole moment will increase with increasing magnetic field and finally saturate, decreasing as the magnetic field further increases

## *6.4 Conclusions*

The model that combines the contributions from free and bound charges at the field level provides a simple, physically justifiable description of the production of THz radiation from semiconductors, and accurately describes the azimuthal and spectral dependences of the THz data. We also investigate the origin of nonlinearity of free carriers, which is the spatial dispersion of incident field. Obviously, other mechanisms may also be possible. However, our work can be considered a starting point in this area of research.

## *References*


[1]P. N. Saeta and B. I. Greene, Appl. Phys. Lett. **63**, 3482 (1993).

[2]X.-C. Zhang, B. B. Hu, J. T. Darrow, and D. H. Auston, Appl. Phys. Lett. **56**, 1011 (1990).

[3]X.-C. Zhang, J. T. Darrow, B. B. Hu, D. H. Auston, M. T. Schmidt, P. Tham, and E. S. Yang, Appl. Phys. Lett. **56**, 2228 (1990).

[4]H. Takahashi, M. Sakai, A. Quema, S. Ono, N. Sarukura, G. Nishijima, and K. Watanabe, J. Appl. Phys. **95**, 4545 (2004).

[5]J. Shan, C. Weiss, R. Wallenstein, R. Beigang, and T. F. Heinz, Opt. Lett. **26**, 849 (2001).

[6]J. Shan and T. F. Heinz, Topics in Applied Physics **92**, 1-56 (2004).

[7]C. Weiss, R. Wallenstein, and R. Beigang, Appl. Phys. Lett. **77**, 4160 (2000).

[8]J. R. Morris, and Y. R. Shen, Physical Review **A15**, 1143 (1977).

[9]J. B. Khurgin, J. Opt. Soc. Am. **B11**, 2492 (1994).

[10] G. D. Powell, J. –F. Wang, and D. E. Aspnes, Phys. Rev. **B65**, 205320 (2002).

[11]J.-F. T. Wang, G. D. Powell, R. S. Johnson, G. Lucovsky, and D.E. Aspnes, J. Vac. Sci. Technol. **B20**, 1699 (2002).

[12]H. J. Peng and D. E. Aspnes, Phys. Rev. **B70**,165312 (2004).

[13]C. W. Oseen, Ann. Phys. (Leipzig) **48**, 1 (1915).

[14]P. P. Ewald, Ann. Phys. (Leipzig) **49**, 1 (1916).

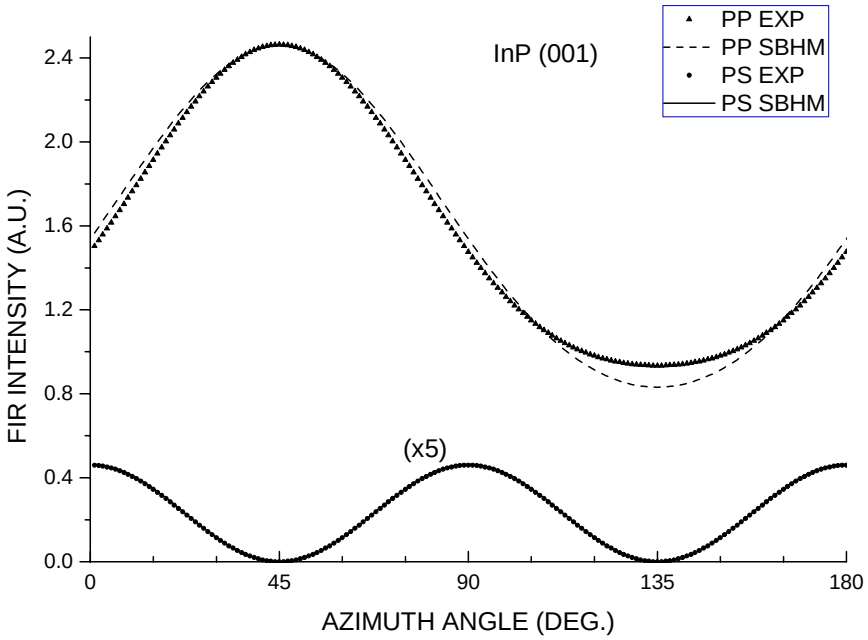



**Figure 6.1 *pp*- and *ps*- polarized FIR intensity for (001)InP. Data are from Ref. 1.**

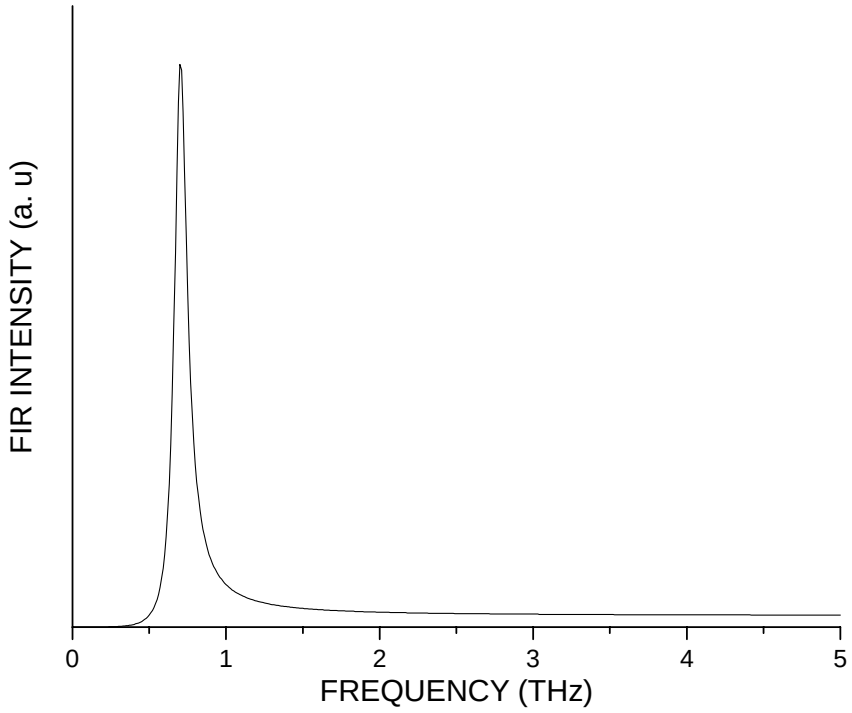



**Figure 6.2 Frequency dependence of the bond-charge contribution to the THz intensity.**

# Chapter VII Spectroscopic Second Harmonic Generation

## *7.1 The spectroscopic properties of the SBHM*

Nearly all of our comparisons between model predictions and data involve fitting intensity anisotropies, except for a single prediction of a frequency dependence for THz radiation in Ch. VI. Therefore, the question arises as to whether our model can deal with energy dependences of NLO responses, and can incorporate the results of theoretical calculations of hyperpolarizabilities in the bond model when such calculations become available. We discuss this point here.

From our model it is clear that we can write the generated fields for all four polarization combinations *pp*, *ps*, *sp*, and *ss* as

$$\vec{E}_{gh} = A(\omega)B(\phi) \tag{7.1}$$

where g and h refer p or s. Of course, A(ω) and B(ϕ) are related to other parameters. For example A(ω) is certainly related to the effective mass of the bond charge, bond strength, losses, etc. On the other hand B(ϕ) is related to geometric properties such as bond angles, vicinal angle of the sample, and angle of incidence. When the variable is ϕ, we find that the SBHM can accurately describe the anisotropy. When the variable is ω, we involve an additional degree of freedom, so we are certain that the SBHM will still describe the data. In fact, the spectral dependence of the hyperpolarizabilities can be expected to give new information about interface properties.

Although our approach is classical, it is a starting point that represents a convenient intersection between theory and experiment. As is the case for many similar problems,

the simple classical model can be extended to semiclassical or quantum mechanical models depending on requirements. For example, we could combine a quantum mechanical calculation of $A(\omega)$ with $B(\phi)$ in our expression for the fields. Hence we certainly expect to be able to predict spectroscopic properties of NLO data such as resonance energies, critical-point parameters, etc.

## *7.2 Spectroscopic SHG*

To support our argument of additional information available from spectral dependences, we present some spectroscopic SHG data of oxide-oxidized and oxide-nitrided layers on Si(111) surfaces tilted 5º toward the (-1 -1 2) direction. The experimental configuration is shown in Fig. 7.1. Two photomultipliers are used so that the data can be normalized to eliminate the effect of variations in source power between pulses and with wavelength. Owing to the awkwardness of tuning Ti-sapphire lasers and their short tuning range, our data cover 755 to 920nm.

Figure 7.2 shows anisotropy data as a function of wavelength for three samples. The first is a vicinal Si (111) wafer that was oxidized then exposed to a nitrogen plasma (oxide-nitrided sample). The other two are oxidized samples that were exposed to an oxygen plasma (oxide-oxidized), one of which is measured as-is and the other after rapid thermal annealing (RTA) at 900º. Using the SBHM and our standard simulation procedure, we obtained the hyperpolarizabilties for each bond. Because the bulk contributions are small, we do not include them in this analysis.

We first compare the hyperpolarizabilities of the two oxide-oxidized samples. Figure 7.3 a, b, and c show the results for the up, step, and back bonds, respectively. The

obvious point is that all hyperpolarizbilities decrease with increasing wavelength. We believe that this is due to the fact that decreasing photon energy moves the process further away from the resonant energy of the first major ($E_1$) transition in Si. Second, the magnitudes of the hyperpolarizabilities for the sample treated by RTA is larger than those for the sample without the RTA treatment, which is reasonable because annealing smooths and otherwise improves the quality of the interface, thereby increasing bond strengths. Third, all real parts of the hyperpolarizabilities have similar shapes for all three samples, whereas the imaginary parts exhibit very difference behavior for the samples with and without RTA. This indicates that imaginary part of the hyperpolarizability is more sensitive to annealing.

Next we will compare data for the oxide-oxidized sample to that of the oxide-nitrided sample. These data are compared in Fig. 7.14. To our surprise, they all behave very similarly except for a minor difference in magnitude. For the back bonds and step bonds, the magnitude of the hyperpolarizabilities of oxide-oxidized sample is larger. For up bond, they are almost the same except at the beginning, where the magnitude of hyperpolarizabilities of the oxide-nitrided sample is bigger.

In summary, the results show that our model gives a consistent description for the frequency-dependent harmonic generation data that we investigate here. By analyzing spectroscopic SHG data using the SBHM, we find that second-order hyperpolarizabilities, which are related to the asymmetry of the bonds, are sensitive to conditions of film growth and the properties of materials. This is consistent with the results previously obtained by Powell et al.

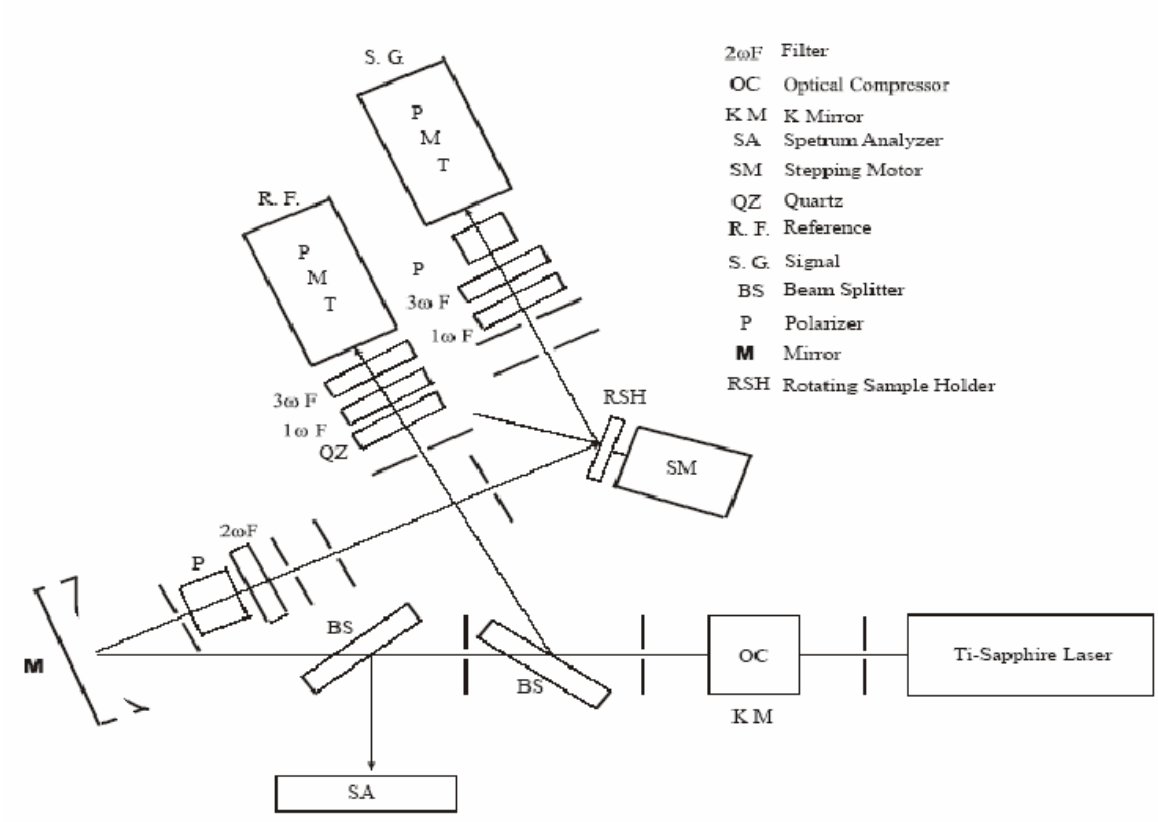



**Figure 7.1 SHG experiment setup**

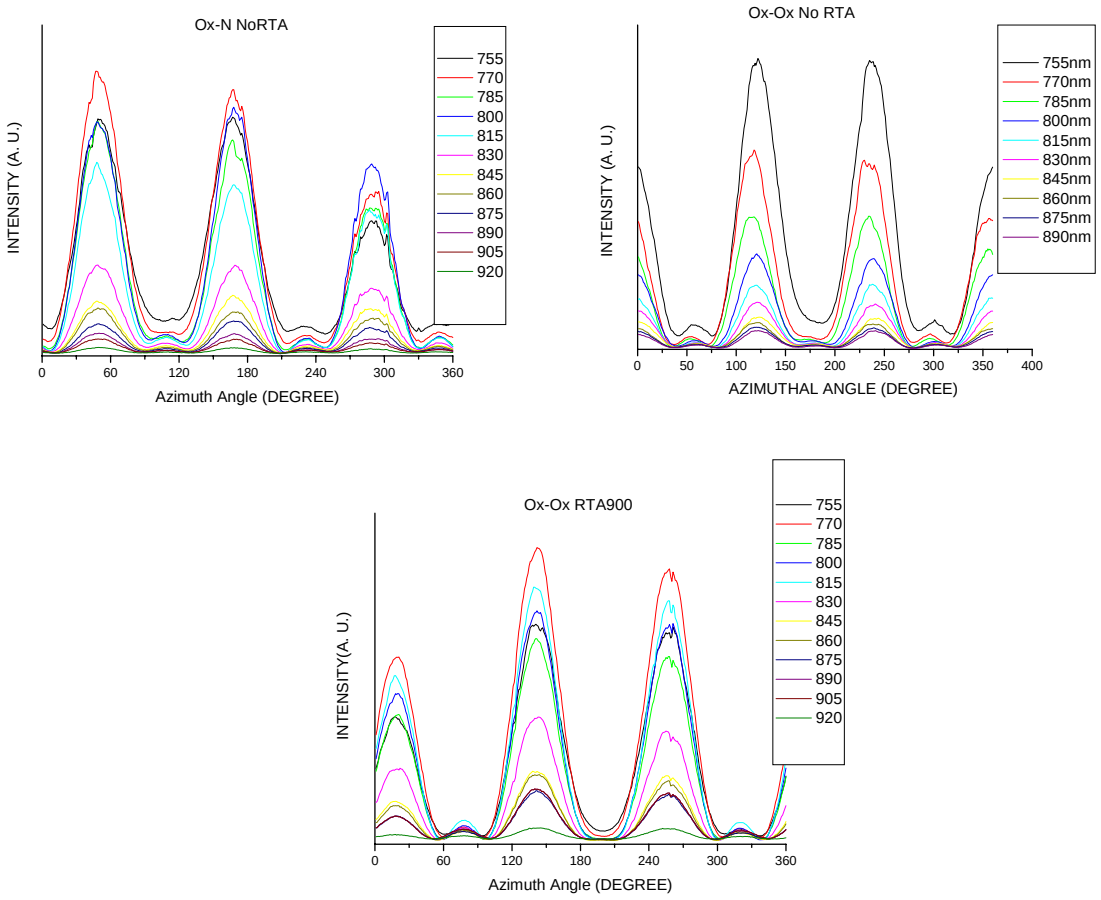
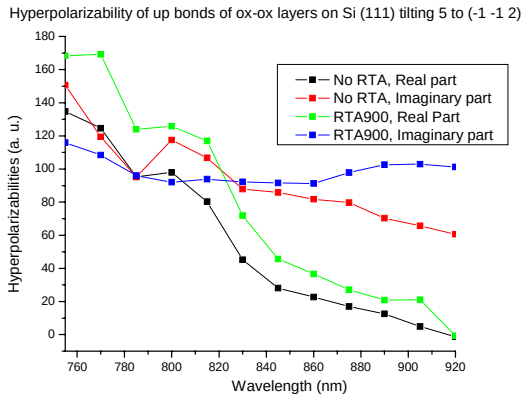
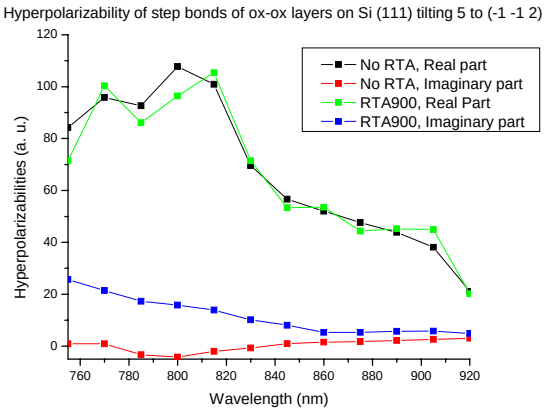


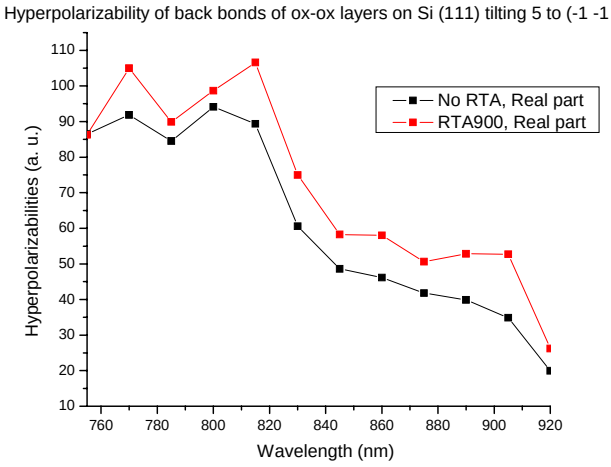

**Figure 7.2 Azimuthal dependence data at difference wavelength for oxide-nitrided and oxide-oxidized layers with and without rapid thermal annealing on Si (111) surfaces tilted 5º towards (-1 -1 2).**




a

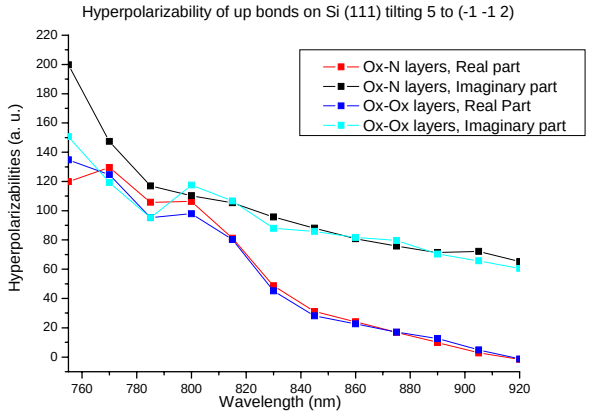



b

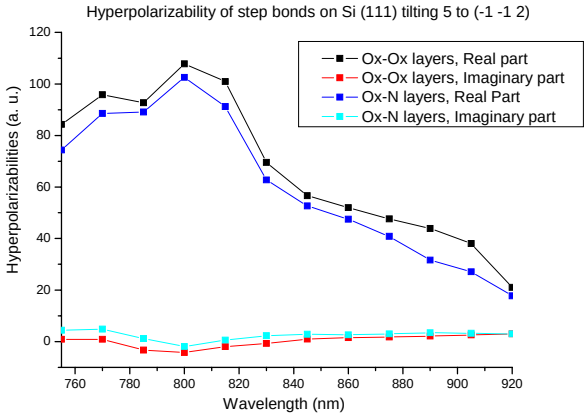



c

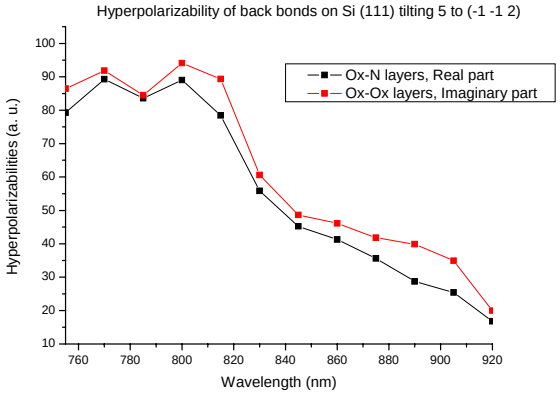
**Figure 7.3 Comparison hyperpolarizabilities for samples with and without RTA: a, up bond; b, step bond; and c, back bonds.**




a




b




c

**Figure 7.4 Comparison hyperpolarizabilities oxide-oxide sample to oxide-nitride sample: a, up bond; b, step bond; and c, back bonds**

# Chapter VIII Conclusions and Proposals

## *8.1 Conclusions*

In this project, we give a complete description of SBHM for harmonic generation. Two ways of derivation are given. The first one is an adaptation and extension of the original SBHM developed for SHG by previous group members, Powell and Wang. The extension uses the classical definitions of dipole, quadrupole, and magnetic dipole combined with the one-dimensional force law to derive analytic expressions for SHG, THG, and FHG. The advantages of this method are that it is simple and straightforward.

The second way is to start from potentials. We begin with the four-vector potential in free space for a point charge. We then expand the potential around the equilibrium position of the point charge. The position variation is due to incident electric field and can be calculated by one-dimensional force law. The advantages of this method are that it is systematic, giving more of a physical meaning to the origins of the different contributions, and it is easily extended to higher order contributions. Of course, the two methods lead to same analytical results. With these extensions and developments the SBHM has become a very strong and simple tool to theoretically calculate any harmonic-generation order, whether originating from the surface or the bulk. In this project we apply the SBHM to dipole-forbidden bulk SHG generation, THG, and FHG, all of which are investigated in detail. For dipole-forbidden SHG, we determine the relative importance of bulk and surface contribution, resolving a controversy in the literature. We find that bulk contributions (quadrupole and spatial dispersion) are minor. For THG, we show first time that our SBHM can not only describe surface harmonic generation but

also can describe bulk harmonic generation as long as motion transverse to the direction of the bond charges is considered. In THG we also find that the surface contribution is much less than that of the bulk, as expected, but that the coherent superposition of bulk and surface contributions is important and cannot be ignored. For FHG, we show that our model can predict the surface roughness effects on FHG.

In the last chapter we extend our model to another nonlinear-optical phenomenon, THz generation from semiconductor surfaces generated by ultrafast laser pulses. We apply the one-dimensional force law to both bond charges and free carriers to combine the two mechanisms for THz generation at the field level and give a simple physical interpretation of the generation of THz. The work also shows that for bond charges the nonlinear response is due to anharmonic restoring forces of the bonds, whereas for free carriers the origin is from the spatial dispersion of incident field.

## *8.2 Proposed work*

Although our SBHM describes the azimuthal data of harmonic and THz generation very successfully, we do not obtain much information about samples from the data. We use least-squares fitting to obtain the hyperpolarizabilities and the bonding angles. However, all above parameters are frequency-dependent. Single-frequency values cannot give us much information about the material. Consequently, it is clear that the future for the various harmonic generations will be spectroscopic, which will give us frequency-dependent hyperpolarizabilities and dielectric functions and thus material properties (from the bonding angle in the material, we can obtain the dielectric constant). These spectroscopic properties can help us regarding the growth of new materials. Hence with

the development of lasers tunable over a wide range, this will be a major direction for nonlinear optics.

One possible application of nonlinear optics to CMOS devices is the use of harmonic generation to monitor variations in doping densities. Dopant density and distribution are two important issues in today's CMOS-based integrated-circuits technology. Consequently, how to monitor doping parameters becomes a critical question. Although secondary ion mass spectrometry (SIMS) can provide a way to obtain accurate depth profiles, its disadvantages are very obvious. First, SIMS is complicated, and the equipment is very expensive. Second, SIMS analysis destroys the sample in the process of obtaining the depth profile. From our formulation in Ch. V, we know that the SHG intensity of free carriers will be proportional to the density of free carriers. Thus it should be possible to use NLO technology to in-situ monitor the density profile of chips, which has the added advantages that optical technology is nondestructive and can be used in any transparent ambient. However, to our knowledge no data in this area yet exist. It may take some time for this this to be realized.

Finally, as we end this project, we hope that our research will be of benefit to others working in this area.

## Publication and Presentation List:

I. Journal papers:

1. H. J. Peng, E. J. Adles, J. –F. T. Wang, and D.E.Aspnes, Relative bulk and interface contributions to second harmonic generation in silicon, PHYSICAL REVIEW B, Vol. **72**, 205203 (2005).

2. H. J. Peng and D. E. Aspnes, Dipole-Radiation Model for Terahertz Radiation from Semiconductors, APPLIED PHYSICS LETTERS, **86** 212109 (2005).

3. H. J. Peng And D. E. Aspnes, Calculation of Bulk Third Harmonic Generation from Crystalline Si with the Simplified Bond Hyperpolarizability Model, PHYSICAL REVIEW B, Vol. **70**, 165312 (2004).

4. D. E. Aspnes, J.–K. Hansen, H. J. Peng, G. D. Powell, and J. –F, T. Wang, Simplified Bond-Hyperpolarizability model of second- and fourth-harmonic generation: application to Si-$SiO_2$ interfaces" PHYSICA STATUS SOLIDI. **(b) 240**, No. 3, 509, (2003).

5. J.–K. Hansen, H. J. Peng, and D. E. Aspnes, Application of the simplified bond-hyperpolarizability model to fourth-harmonic generation" JOURNAL OF VACUUM SCIENCE AND TECHNOLOGY **B21** (4), 1798, (2003).

6. H. J. Peng, Z. X. Shen, E. H. Lim, C. W. Lai, R. Liu, A. T. S. Wee, A. Sameer, J. Y. Dai, B. C. Zhang, and J. Z. Zheng, " Effects of First rapid thermal annealing temperature on Co silicide formation" SOLID-STATE ELECTRONICS **47**, 1249 (2003).

II. Conference presentations:

1. H. J. Peng, E. J. Adles, and D. E. Aspnes, Application of the Simplified Bond-Hyperpolarizability Model to Bulk Second- and Third-Harmonic Generation in

Semiconductor, The 51st American Vacuum Society (AVS) International Symposium and Exhibition (Anaheim, CA), Nov. 2004 (presented by H. Peng).

2. E. J. Adles, H. J. Peng, and D. E. Aspnes, Bulk vs. Interface Contributions to Second Harmonic Generation of Si in the Simplified Bond Hyperpolarizability Model, 32nd Conference on the Physics and Chemistry of Semiconductor Interfaces (Bozeman, Montana), Jan. 2005 (presented by E. J. Adles).